Investigation of Dry Anodes Utilizing Electroplated Nickel and Nickel-Alloy Foam Catalysts for the Alkaline Oxygen Evolution in Anion Exchange Membrane Electrolyzers

Inaugural dissertation
of the Faculty of Science,
University of Bern

presented by

Etienne Berner

Supervisor of the doctoral thesis:

Prof. Dr. Matthias Arenz

Department of Chemistry, Biochemistry and Pharmaceutical Sciences

WISSEN
SCHAFFT
WERT.

Investigation of Dry Anodes Utilizing Electroplated Nickel and Nickel-Alloy Foam Catalysts for the Alkaline Oxygen Evolution in Anion Exchange Membrane Electrolyzers

Inaugural dissertation
of the Faculty of Science,
University of Bern

presented by

Etienne Berner

Supervisor of the doctoral thesis:

Prof. Dr. Matthias Arenz

Department of Chemistry, Biochemistry and Pharmaceutical Sciences

Accepted by the Faculty of Science.

Bern, December 4, 2024   The Dean
                                         Prof. Dr. Jean-Louis Reymond

WISSEN
SCHAFFT
WERT.

"Hydrogen is a light, odorless gas, which,

given enough time, turns into people."

Edward Robert Harrison

To my beloved wife, my daughter, my parents, and my sisters

Abstract

The dependence of modern society on fossil-based products is inherently connected to prosperity, well-being, wealth, and comfort. Conversely, the imperative to transition into a society powered solely by renewable resources and processes necessitates a fundamental change, not only in terms of technical advancements, but also in economic considerations and critical self-reflection.

This study investigates the extensive domain of electricity-to-hydrogen conversion, which is considered to play a crucial role in the future fossil-free ammonia production. The conversion of ammonia into fertilizer is essential for ensuring global food security. The research approach to optimize the inherent reaction of oxygen evolution during electrochemical water splitting for hydrogen production is investigated by the mean of a gas diffusion electrode (GDE) setup in an alkaline environment. Recent advancements in water electrolysis have led to the development of anion exchange membrane water electrolyzers (AEMWE), which potentially combine the advantages of established alkaline electrolyzers with those of proton exchange membrane electrolyzers.

The presented GDE setup is introduced as a "dry anode" configuration, subsequent to the recent introduction of the dry cathode in AEMWEs. This configuration can simulate reaction conditions of effective devices. Nickel and Ni alloy foams were synthesized using the hydrogen bubble template method, which generates highly porous metal films with enhanced surface area, thereby promoting an increased number of catalytically active sites and consequently higher reaction rates.

Oxygen evolution rates, normalized to the geometric electrode area, reached substantial current densities at quasi steady-states exceeding 4 A cm^{-2} at an iR-corrected set potential of 2.1 V$_{RHE}$ for a pure Ni foam benchmark catalyst. Galvanostatic investigation of NiFe alloys demonstrated a current density of 3 A cm^{-2} for the optimal composition at 1.82 V$_{RHE}$, based on the statistical evaluation of an extensive dataset.

In conclusion, the presented research demonstrates the potential of a dry anode configuration as an effective platform for studying high-performance oxygen evolution in an alkaline environment, supporting the development of advanced water electrolysis technologies.

Acknowledgements

I am deeply grateful and feel privileged to have worked under such supervision. Foremost, I would like to express my greatest appreciation to Prof. Matthias Arenz's patience, encouragement, and willingness to share his vast knowledge. His mentorship extended beyond just academic guidance - he taught me how to think critically, approach complex problems, and grow as an independent researcher. His trust in my abilities gave me the confidence to explore new directions and I am thankful for the freedom he provided while still offering direction when needed.

Without the help and creativity of Dr. Gustav Wiberg, this work would not have been possible. He was a steady source of inspiration and fun but also contributed as a critical analyst and questioned the important aspects. I am very grateful for the help with the setup optimization and for all the collaborations and joy in the laboratory.

Further, I want to express my gratitude to all former and current group members. Thank you, Dr. Vladislav Mints for advices in electrochemical experiments, Dr. Nicolas Schlegel, my office neighbor and local guide, Dr. Johanna Schröder and Dr. Shima Alinejad for the introduction to GDE measurements, Dr. Aline Bornet for organizing group activities, Dr. Jia Du and Dr. Damin Zhang for experimental advice, Dr. Ilya Pobelov for keeping the AFMs running, Dr. Pablo Collantes for informative video calls, Renan Lopes Munhos for inspiring conversation, Sven Nösberger for practical exchanges, Divyansh Gautam for discussion of electrodepositions, Dr. Menglong Liu, Ahmad Tirmidzi, Tim Kunzmann and Jonas Forner.

I also thank Prof. Peter Broekmann, Dr. Abhijit Dutta and Dr. Pavel Moreno-Garcia for valuable experience exchange and maintaining the optical microscope.

My appreciation goes to the in-house services, specifically the mechanical workshop team of T. Hübscher, A. Bigler, and S. Hostettler. I am grateful to the analytical research and services team members: Dr. S. Grabowsky, B. Frey, and D. Biner.

I extend my gratitude to Prof. Marian Chatenet for reviewing this thesis.

Lastly, but most importantly, I express my deepest appreciation to my beloved wife for always encouraging and supporting me throughout this journey, giving birth to our beautiful daughter, and of course to my mother, father, and sisters.

Table of contents

List of abbreviations

AEM	Anion exchange membrane
AEMFC	Anion exchange membrane fuel cell
AEMWE	Anion exchange membrane water electrolyzer
Au	Gold
BBC	Brown Boveri & Cie (company)
CE	Counter electrode
CH_4	Methane (gas)
Co	Cobalt
CO	Carbon monoxide (gas)
CO_2	Carbon dioxide (gas)
Cr	Chromium
Cu	Copper
CV	Cyclic Voltammetry / Voltammogram
ECSA	Electrochemical active surface area
Fe	Iron
GDE	Gas diffusion electrode
GDL	Gas diffusion layer
GFSA	Giovanola Frères SA (company)
HBT	Hydrogen bubble template
HEA	High entropy alloy
$HFR_{Sol.}$	High frequency solution resistance
HFR_{Cell}	High frequency cell resistance
H_2	Hydrogen (gas)
H_2O	Water
IHT	Industrie Haute Technologie (company)
KOH	Potassium hydroxide
MEA	Membrane electrode assembly
MEMS	Micro electro mechanical systems
Mn	Manganese
Ni	Nickel

N_2	(Di)Nitrogen (gas)
O_2	(Di)Oxygen (gas)
OER	Oxygen evolution reaction
ORR	Oxygen reduction reaction
PEM	Proton exchange membrane
PEMFC	Proton exchange membrane fuel cell
PEMWE	Proton exchange membrane water electrolyzer
Pt	Platinum
PTFE	Teflon (polytetrafluoroethylene)
PTL	Porous transport layer
RDE	Rotating disk electrode
RE	Reference electrode
RHE	Reversible hydrogen electrode
RWE	Rheinisch-Westfälisches Elektrizitätswerk AG (company)
SEM	Scanning electron microscopy
SEM-EDS	SEM with energy dispersive X-ray spectroscopy
SHE	Standard hydrogen electrode
SS	Stainless steel
US	Ultrasonic
W	Tungsten
WE	Working electrode
XRD	X-ray diffraction
Zn	Zinc

1. Introduction

This chapter examines the historical aspects of gas production, including hydrogen as a city gas and water electrolysis, with a focus on Bern and Switzerland, and provides a historical account of electrolyzer development. The objective of this thesis is outlined by introducing current developments in electrolysis technology. I deliberately refrain from a theoretical recapitulation of the foundational principles of electrochemistry here, as specialized works are better suited for this purpose, such as "Electrochemical Methods: Fundamentals and Applications" [1] by Allen J. Bard and Larry R. Faulkner or "Modern Electrochemistry" [2] by John O'M Bockris and Amulya K. N. Reddy.

The history of gas production in Bern

Bern pioneered the illumination of streets in Switzerland by establishing privately funded gas production in 1840, which was operational in 1843. Soon after, other initiatives in Switzerland followed the example and installed their own gas production facilities (Geneva and Lausanne in the late 1840s, Basel and Zürich in the 1850s) [3]. Today, "Gaswerk Bern" is renowned for its cultural activities and serves as a venue for diverse events, exhibitions, and performances. The former industrial structures have been repurposed, establishing a center for arts and alternative cultures. The gas production facility was closed in 1967.

This paragraph is based on two primary references [4,5] and reflects the interactions between technological progress, economy, society, and politics.

Situation before 1843

In Paris, an organization that illuminates city streets using oil lamps has been established since 1667. The primary objective was to improve safety and police security during evenings. Bern established a city oil lighting system in 1748 [6], when the police department of the city conducted a pilot study on public lighting to evaluate a cost-benefit analysis. A political debate followed, and only in 1768, the city council announced the continuous installation of 200 oil lamps and established a detailed timetable (from mid-September to Easter the light shall be on from nightfall until

1

around midnight) and cost-sharing within the offices of the city and the republic. Meanwhile, the employees of the privately held contractor in charge of refilling and maintaining the lights were under suspicion. "They would become thirsty from climbing ladders, so they would turn into the numerous cellar taverns and partake in drinks there." At the beginning of May 1843, 137 single- and 144 double-arcade oil lanterns and approximately 100 reflector lamps ("Reverbèren") were finally erased from the urban landscape.

Initiation of the gasworks Bern

In the early 19th century, a novel technology using gas instead of oil for illumination emerged in Europe. The objective was to gasify coal through pyrolysis and to combust the resultant gaseous product, primarily comprising carbon monoxide (CO, ~30 Vol.%) with trace amounts of hydrogen (H_2, ~2 Vol.%) and carbon dioxide (CO_2, ~2 Vol.%), alongside a predominant nitrogen content (N_2, ~66 Vol.%), in specialized gas lamps to generate illumination (**Fig. 1 (a)**). This gas composition is sometimes referred as generator gas and has a typical calorific value of 3.9 to 4.1 MJ m^{-3} [7,8]. In 1823, the communal council of the city of Bern initially deliberated on gas lighting. The technical and cost-related concerns were addressed in 1840 by engineer J. B. Roux, who had implemented such a system in the French city of Mulhouse. His report emphasized the feasibility of establishing a gas-powered urban lighting system but raised concerns regarding coal availability. Consequently, it was proposed that experiments should be conducted to assess the viability of domestic coal and peat as alternatives to expensive imports. However, the municipal government did not endorse this proposal, and thus, no funding was allocated for testing.

Instead, a private company named "Compagnie du Soleil" (Company of the sun) was founded to finance testing and gasworks construction. Concurrently, the luminous output of the installed oil-based illumination in comparison to the anticipated novel gas-powered lighting was a subject of negotiation between "Compagnie du Soleil" and governmental representatives, a process supported by the University of Bern. At that time, the standardization of light measurement was predicated on the Carcel-lamp, an invention from 1800. This device, an oil lamp equipped with a timer, emitted a "constant and continuous" illumination. The official photometric measurement, initiated by the city's police department, executed under supervision of company

representatives and led by Prof. Karl Brunner, Professor of Chemistry and Pharmacy, revealed an annual output of 137'987 h of Carcel-light, which fell short of the 200'000 h anticipated by company representatives. Professor K. Brunner used a photometer after Ritchie for the measurements, and noted that the results should not be considered accurate due to the imprecise nature of the Carcel-lamp as a measurement standard. However, J. B. Roux argued that the novel gas system provides expected 222'456 annual hours of Carcel-light, indicating that despite its apparently higher absolute cost, it was comparatively competitive when evaluated against the existing situation. The police commission was persuaded and favored gas illumination; however, the city parliament strongly criticized the studies and J. B. Roux's expense bill amounting to 200 Swiss Francs. Based on the experimental results of Prof. K. Brunner, "Compagnie du Soleil" presented a proposal to the city, which was subject to extensive deliberation. The annual expenditure for oil illumination amounted to 10'735.70 Francs, while the proposed gas lighting would incur an additional cost of 3000 Francs. Consequently, a public solicitation for alternative proposals from other private entities was initiated; however, no additional offers were received. The city government subsequently resolved to allocate the supplementary cost from the revenue generated by dog taxation through a municipal decision on December 30, 1840, in response to increasing political pressure for the implementation of gas lighting.
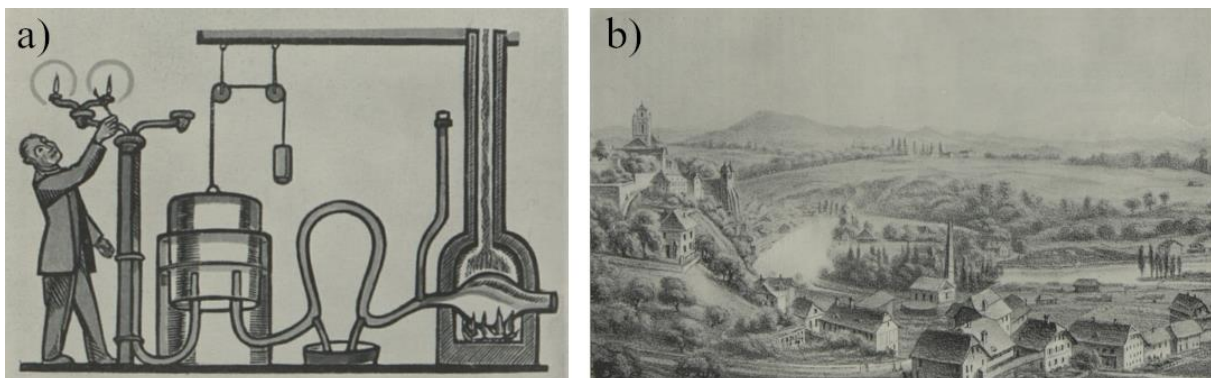
Figure 1: (a) Illustration from England around 1800 showing a simplified coal gasification process [4]. (b) Illustration of the first gasworks in the Marzili in Bern. The chimney had to be constructed taller than originally planned as a result of objections raised during the building permit approval process [4].

Within a few months, the politically mandated capital of 150,000 Francs for the stock corporation was secured by more than 187 shareholders. Several legal matters required

attention and the city government regulated in detail specifications, including the precise hours of Carcel-light provided, the quantity and position of lamps, security considerations such as production interruptions, public safety, and maintenance protocols, which were contractually addressed. The gasworks was projected to be situated in proximity to the Marzili (**Fig. 1 (b)**), an optimal location due to several factors. It was situated near the Aare for coal transportation, sufficiently close to the city, yet adequately distant from critical infrastructure, and in a low-lying area, as only natural ventilation was available. In June 1841, the building permit was granted after multiple objections. Shortly after the commencement of construction work, the company encountered challenges, as the opening of streets for pipe insertions did not progress as rapidly as anticipated, resulting in traffic congestion and public dissatisfaction. Furthermore, four of the initially constructed retorts cracked, and some pipes fabricated from clay were damaged prior to utilization, as revealed by initial tests. This caused an unpleasant odor to permeate the city, leading to widespread speculation and significant pressure on the company. However, on April 25, 1843, the test to illuminate the burners in Kramgasse and Marktgasse was successful, and the quality of the light was deemed superior to oil lamps by local journalists reporting in contemporary newspapers.

First years of operation

Initially, local coal from Beatenberg was shipped via Thunersee and the Aare to the gasworks. The annually contracted 1'500 t of coal could be delivered until 1856, then the resources were exploited. Another mine situated in Boltigen operated until 1860, when it was compelled to cease operations due to the establishment of a new railway connection to Bern, which facilitated the importation of superior coal from foreign countries.

After a mere three years of operation, "Compagnie du Soleil" initiated legal proceedings against the city of Bern for uncompensated income due to superior performance in Carcel-light hours than contractually stipulated. The local tribunal adjudicated two years later that the delivered 581'619 h of Carcel-light per annum exceeded twice the contracted amount of illumination. Consequently, the city was obligated to remunerate an additional 6'000 Francs annually from May 11, 1844, as compensation. Gas illumination became increasingly significant to private individuals and establishments,

who could procure and remit payment through monthly subscriptions. At the commencement of 1860, negotiations for a new contract between the municipality and the company were initiated, precipitating discussions among politicians and private investors. By November 30, 1860, the municipality had acquired control from the private corporation.

Gasworks operated by the city of Bern

The operation of the gasworks and the city illumination were, by municipal resolution of December 14, 1860 now functions of the government. Commencing in 1860 with 270 private consumers utilizing 1800 burners, by 1864 there were in excess of 4000 private gas flames. New pricing structures were implemented, resulting in reduced gas costs. Furthermore, the street illumination was enhanced, and clay pipes were replaced by metal pipes. In 1869, the net profit reached 100,000 Francs, and the gas price was reduced from 45 to 40 Rappen (cents) per cubic meter. The gasworks in the Marzili reached capacity limitations, and within one year, in September 1876, a new gasworks was constructed in Lindenau. By 1875, more than 13,300 private gas flames were connected to the grid. In 1877, over 3'500 t of coal were processed, which yielded 1'385 t of coke as a by-product for sale. By-products such as coke and ammonia water became increasingly economically significant as revenue sources for the gasworks due to demand from the construction industry. The urban illumination improved further, with 867 gas lamps recorded in 1889.

In 1891, electrical illumination was introduced, powered by the hydropower plant Mattwerk. Consequently, gas became less significant for lighting purposes. However, it remained useful for heating and cooking, and its importance continued to increase. In 1895, the net profit of the gasworks amounted to 259'016.72 Francs, which resulted in a further reduction in gas prices for consumers. The charge per cubic meter was now 20 Rappen for cooking and heating, while illumination was priced at 25 Rappen m^{-3}.

Water gas, further expansion and war

The annual production increased to exceed 4 Mm³ and reached the capacity limit. To prevent further reconstruction, a water gas production facility was implemented in 1902. Water gas was discovered by Felice Fontana in 1780 when he observed water vapor reacting with incandescent coal [7]. The reaction can be described as follows:

$C + H_2O \rightarrow H_2 + CO$. The H_2:CO ratio is dependent on the pressure and temperature within the reactor (**Fig. 2 (a)**), and contains ~50 Vol.% H_2 and 50 Vol.% of CO, traces of methane (CH_4, 1 Vol.%), and almost no nitrogen. This served as a supplementary source and increased the calorific value of the mix. Water gas has a calorific value of ~10 MJ m^{-3}, which is twice as high as that of generator gas. In 1903, 404'000 m^3 water gas was produced and blended with the city gas. However, due to increased demand, an expansion, several retrofitting, and novel equipment for coal preparation were implemented in 1907. By 1908, gas production reached 8.6 Mm^3, necessitating 28 kt of coal.

Figure 2: (a) H_2:CO ratio in relation to reactor temperature for water gas [7]. (b) Annual gas production from 1860 to 1940 in Mm^3 of the gasworks Bern. The sharp decrease around 1919 was caused by coal shortages during WWI [4]. (c) Washing machine with gas heating [5].

The utilized bituminous coal and the new installations delivered improved calorific valued gas, as more H_2 was present in the gas mixture (typically ~40 Vol.%) along with a higher CH_4 content (~20 – 40 Vol.%). CO remained at ~10 - 20 Vol.% and N_2 is reduced to lower than 10 Vol.%. The calorific value reached for such a typical city gas composition was ~16.5 - 21 MJ m^{-3}. The process yielded 20 kt of coke and 55 t of pure ammonia as byproducts. During the First World War, the coal supply was limited. In 1916, an all-time high of 15.3 Mm^3 of gas was produced and sold for 18 Rappen m^{-3}. The production decreased almost by half in the following years (**Fig. 2 (b)**). The coal was priced at 157 Francs t^{-1} in 1919, whereas before the war it was 32 Francs t^{-1}. Similarly, the gas price increased and its usage was rationed. Several street lights were completely shut down, and the coal mine in Boltigen was reopened. The gas price increased by more than a factor of 3, to 60 Rappen m^{-3}. It took several years to

overcome the crisis; in 1927, approximately 14 Mm^3 was produced, and the water gas facility had to be operational full-time. Meanwhile, the gas was used primarily for cooking and heating, with illumination accounting for only 0.4 % of usage. In 1927, the remaining gas illumination in the city was replaced with electric light. Until 1936, the annual gas production continued to increase steadily, reaching 20 Mm^3. Furthermore, the gas pipe network has grown continuously, and various new production facilities have been installed. During the Second World War, a similar scenario with a shortage in coal was present: the mine in Boltigen was reopened again, and even wood and peat were degassed.

Time of change

Following the outbreak of the Korean War in 1950, coke reserves were mandated by governmental regulations, legitimating gasification of coal. However, the increasing electrification of household appliances (**Fig. 2 (c)**) raised questions regarding the future viability of gasworks. In 1962, Switzerland established its initial gas network with the objective of ensuring the availability of natural gas (consisting mainly of CH_4) throughout the country. In 1967, the initial supply of natural gas reached the newly constructed spherical gas storage facilities in Bern, resulting in the permanent cessation of gasworks operations. In its final year of operation, 30 kt of coal was processed into 18.5 Mm^3 gas with a calorific value of 17.2 MJ m^{-3} [5]. Natural gas typically exhibits a calorific value of 35.5 to 39.7 MJ m^{-3}, with the highest value obtained when pure CH_4 is delivered [9].

Summary of 124 years continuous gas production in Bern

The use of gas illumination motivated the implementation of gasworks in 1843. Initially, the gas consisted primarily of CO with a trace of H_2 blend (~2 Vol.%) and N_2 as a main component, leading to a low calorific valued gas. One explosion in 1876, near the Federal Council Building, injured one employee of the gasworks; however, no deaths caused by other explosions or gas leakages were recorded over the entire period of 124 years. Though unfortunately, several suicides have been associated with gas poisoning. Water gas was introduced in 1902, which increased the H_2 content and calorific value of the gas. By 1908, improved installations and bituminous coal usage led to a more efficient city gas with substantially higher H_2 (~45 Vol.%) and CH_4 (~25 Vol.%)

content. The usage of the gas transformed from illumination to heating, with electrification as the driving force. During both World Wars, coal shortages led to lower production and increased price levels, along with restrictions on gas usage. In 1967, gasworks closed permanently when the city's gas grid was connected to a national grid fed with natural gas.

History of electrolysis and electrolyzer fabrication in Switzerland

Switzerland has played an influential role in commercially available electrolyzers over the past century [10]. Water electrolysis requires a relatively high amount of electrical energy, i.e. for an alkaline electrolyzer today 53.4 kWh kg^{-1} H$_2$ at an efficiency of 73 % [11] (if 1 kg H$_2$ equals to 39 kWh kg^{-1} at an isothermal potential V$_{SHE}$=1.47 [12], otherwise V$_{SHE}$=1.23 and 1 kg H$_2$ equals to 33.3 kWh kg^{-1}). Earlier electrolyzers were slightly less efficient and requested consequently higher amount of electricity.

Initial electrochemical industries were installed in places with excess hydropower, such as near Niagara Falls (1881, U.S.), Rheinfelden (1898, Germany), and Neuhausen am Rheinfall (1897, Switzerland). These industries are operated by chlor-alkali electrolysis or the electrochemical production of metals. Hydrogen was a byproduct of no interest for these enterprises at the time.

In 1899, Dr. Oscar Schmidt in Zürich obtained a patent (German patent DRP 111131 [13]) for a reactor design that would subsequently prove significant [14]. His invention comprised a filter press electrolyzer with a bipolar configuration capable of incorporating up to 96 individual cells (**Fig. 3 (a)**). The electrolyzers designed by Schmidt utilized asbestos cloth diaphragms and electrolytes containing 10 % potassium carbonate. These devices operated at 65 V with 26 cells and 110 V with 44 cells, capable of handling cell currents up to 150 A. The 44 cell version could generate up to 66 Nm³ (5.9 kg) of H$_2$ daily. Maschinenfabrik Oerlikon produced a slightly altered version of this electrolyzer under the brand Oerlikon-Schmidt. By 1901, these bipolar water electrolyzers had been adopted by 11 different companies and, in total, more than 800 of these units were operational worldwide [15] in the first decades of the 20th century [16].

In the late 1800s, the primary applications of hydrogen were confined to balloon inflation, platinum melting, and lead accumulator soldering. The 1920s and 1930s witnessed a significant increase in hydrogen demand for ammonia production, which

served as a precursor for fertilizers (nitrates) and explosives (ammonium nitrates) through the Haber-Bosch process: $N_2 + 3\ H_2 \rightarrow 2\ NH_3$. This heightened requirement for hydrogen in conjunction with the economic viability of hydroelectric power in mountainous regions has propelled advancements in water electrolysis technology.

Ewald A. Zdansky, employed by the Swiss company Lonza, developed the first pressurized industrial alkaline water electrolyzer, which was commissioned in 1948 in cooperation with Giovanola Frères SA (GFSA), located in Monthey. In 1951, the German firm Lurgi introduced a 30 bar pressurized electrolyzer to the market [17]. Subsequently, Lurgi acquired all of Lonza's patents (**Fig. 3 (b)**), which encompassed 32 patents filed by Zdansky between 1950 and 1956 [18]. Pressurized alkaline electrolyzers successively have become a dominant type of electrolyzer installation. Typical data for these electrolysis cells were as follows: current density of 2 kA m^{-2} (200 mA cm^{-2}), cell voltage of 1.9 V, operating temperature of 80° C, electrolyte concentration of 25 % caustic potash (KOH), and energy consumption of ~53 kWh kg^{-1} H_2.

In 1967, Maschienenfabrik Oerlikon merged with Brown Boveri & Cie, retaining the name BBC Electrolyzer System Oerlikon. A notable achievement of this entity was the construction of one of the world's largest electrolysis facilities for the KIMA fertilizer plant in Aswan, Egypt. Between 1973 and 1980, the company manufactured 144 Oerlikon modules EBK 385-70 in three phases of expansion. These modules had a nominal hydrogen production capacity of 32'400 Nm³ (2.9 t) h^{-1}, which was equivalent to 162 MW of electrical input [16].
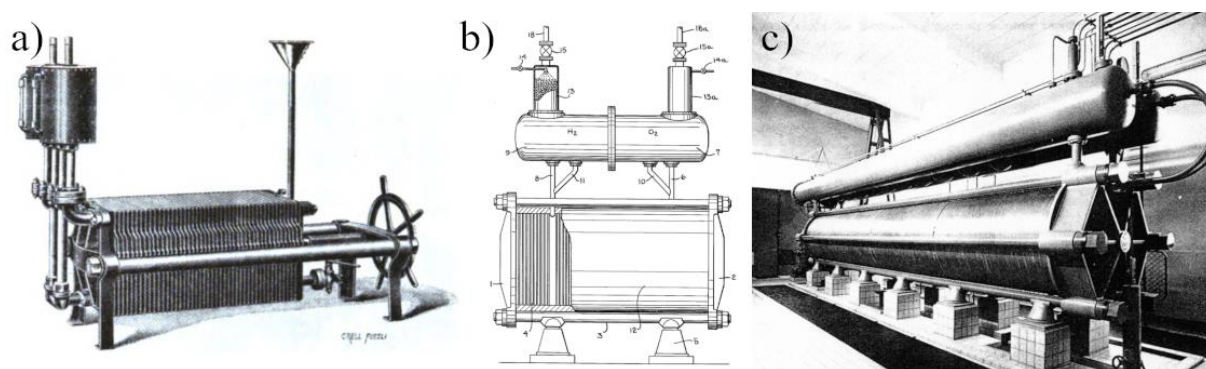
Figure 3: (a) Oerlikon-Schmidt electrolyzer design from 1902 [16]. (b) Patent by E. Zdansky of a pressurized electrolyzer from 1951 [16]. (c) Pressurized electrolyzer at 30 bar, originally developed by Lonza, with a production capacity of ~66 kg H_2 h^{-1}, requiring an electrical input of 3.4 MW [17].

Prior to 1995, Lurgi delivered more than 100 pressurized electrolyzers to global clients [19]. The most substantial installations were constructed for Sable Chem. Ind. Ltd. in Zimbabwe, and Crif in Peru. Lurgi discontinued its electrolysis operations in 1996, transferring all intellectual property rights and customer service to its former manufacturing associate GFSA. In 2004, Industrie Haute Technologie (IHT) based in Monthey, acquired responsibility for the electrolysis activities previously handled by Lonza Group and GFSA. In a more recent development, the German company Sunfire GmbH acquired IHT in 2020. On September 11, 2024, Sunfire announced a major contract for a 100 MW pressurized alkaline electrolyzer installation at the Rheinisch-Westfälisches Elektrizitätswerk AG (RWE) hydrogen site in Lingen, Germany [20].

Current development in water electrolysis

The imperative to transition from an economy reliant on fossil fuels to one powered by renewable sources generated interest in alternative approaches to reduce dependence on fossil-based resources [21]. H_2 plays a crucial role in this transition, accounting for approximately 2 % of global greenhouse gas emissions [22], which is attributable to the fact that approximately 95 % of the annual ~100 Mt H_2 is currently produced from fossil sources. Since its inception, the concept of a "Hydrogen economy" [23] has been challenged by the core that H_2 molecules do not naturally occur in abundance. The production of H_2 requires an energy input. As explained before, H_2 obtained from water electrolysis is energy intensive, therefore a considerable effort of research is spent on improving the catalytic material, the gas separator, the current collectors, and the device efficiency to overcome the "terawatt challenge" [24] of hydrogen in its global role [25]. Currently installed water electrolyzers predominantly comprise alkaline systems, which were previously described, with an increasing proportion of proton exchange membrane (PEM) electrolyzers. The economic aspects of cost-effective H_2 production remain essential for the successful implementation of large-scale installations [26,27].

Proton exchange membrane electrolyzers

The invention of the PEM electrolyzer, initially referred to as solid polymer electrolyte (SPE), by General Electric in the 1960s constituted a significant advancement in water electrolysis technology [28]. This system operates under acidic conditions, in contrast

to its alkaline counterpart. PEM electrolyzers demonstrate the capability to function at substantially higher current densities, attaining levels exceeding 2 A cm^{-2}, which can contribute to reduced operational expenses and potentially lower overall electrolysis costs. The relatively thin membrane (~100 – 250 µm), commonly referred to as the Nafion membrane by its proprietary name, functions as both a gas separator and a proton conductor, constituting the core of the system and enabling the achievement of higher current densities (**Fig. 4**). In comparison to alkaline electrolyzers, the solid polymer membrane in PEM electrolyzers facilitates a thinner electrolyte layer, thereby enhancing efficiency by reducing internal resistance [29]. Nafion, a sulfonated tetrafluoroethylene polymer (PTFE), was developed in the late 1960s by Walther Grot for DuPont as a modification of Teflon [30].

A considered limiting factor of PEM technology is its catalyst availability, which relies on iridium and ruthenium [31,32]. Both of these rare platinum (Pt) group metals are obtained as side products from Pt mining and have very limited availability [33]. Therefore, the scaling possibility is debated [34], but considerable progress in smaller
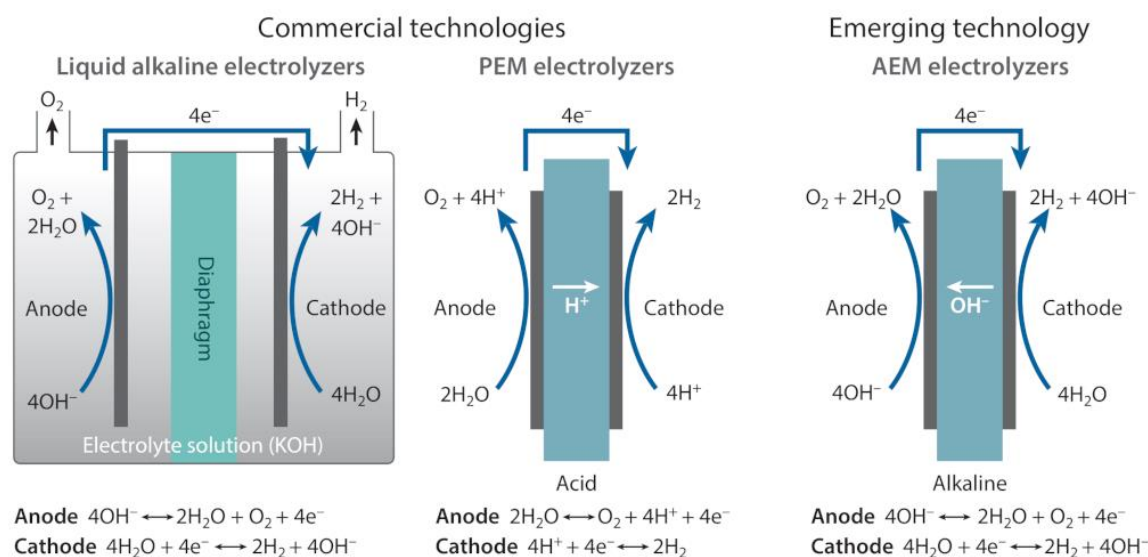
Figure 4: Commercial water electrolysis methods at low-temperatures (typically below 100° C), including KOH liquid, PEM systems and the emerging anion exchange membrane (AEM) technology. The figure highlights key differences in the half-cell reactions. Liquid systems typically use gapped electrodes (electrodes arranged in a "zero-gap" configuration on the diaphragm are also employed) and porous diaphragms as gas separator, unlike the solid polymer membranes in PEM and AEM. Water consumption and production differ between AEM and PEM.

<div align="right">© 2019 by Annual Reviews [34]</div>

Ir loadings from initially 1 – 3 mg cm^{-2} to below 100 µg cm^{-2} at comparable current densities of 1.8 A cm^{-2} [35] and possible Ir and Ru recycling [36] offer viable pathways to overcome these concerns. To further enhance PEM efficiency, the reduction of membrane thickness is proposed [37], but inherently leads to mechanical issues when operated under high pressure of ~30 bar. PEM electrolyzers offer additional advantages regarding compactness, which allows faster ramping and response times to the intermittent nature of renewable electricity [38].

In recent years, the anion exchange membrane (AEM) electrolysis has emerged as a promising technique for hydrogen production, garnering significant attention due to its potential cost-effectiveness [39–41].

Anion exchange membrane electrolyzers

This technology obtains significant attention due to its potential to merge the benefits of PEM with those of alkaline electrolysis. PEM electrolysis offers advantages such as high efficiency, current density, and quick ramping capabilities. Meanwhile, alkaline electrolysis provides advantages like the use of non-precious metal catalysts, stable operation, scalability, and durability. As a result, the advancement of AEM water electrolysis (AEMWE) is viewed as highly important in the field [42].

Current pressurized alkaline electrolyzers face challenges due to their substantial weight, which results in relatively slow ramp-up times. Typically, a ~4 MW system weights about 70 t. Ideally, these systems operate therefore continuously without interruption at temperatures of approximately 80° C. To address the intermittent nature of renewable energy sources, it is necessary to develop lighter and more compact systems that can be ramped up quickly.

AEM technology offers the use of thin gas separators; hence, decreased internal resistance and higher efficiency, and high current densities of more than 5 A cm^{-2} in membrane electrode assemblies (MEAs) have been demonstrated manifold [43–45]. This illustrates the capabilities of AEM technology in terms of enhanced catalyst stability and elevated production rates. However, the AE membrane still has room for improvement in terms of mechanical stability and gas tightness to be considered as a valid alternative to PEM electrolysis [46–49]. To pursue weight reduction, the concept of a dry cathode for AEMs was introduced in recent developments [50–53]. Using this configuration, current densities above 1 A cm^{-2}, requiring less than 2 V in MEA devices,

were achieved. Another possible benefit of this configuration is that the H_2 produced is free from water and requires less subsequent processing than the traditionally generated H_2 in alkaline vapor. However, KOH is typically fed at both the anode and cathode to ensure the electrical conductivity and hydroxide availability.

Objective and scope of the thesis

The primary objective of this investigation was to examine the oxygen evolution reaction (OER) in the gas diffusion electrode (GDE) configuration under alkaline conditions, analogous to a dry cathode anion exchange membrane (AEM) setup but with inverted polarized electrodes.

Context

The initial GDE configuration employed during this work was developed to investigate the acidic oxygen reduction reaction (ORR) for fuel cell applications [54–57] and to bridge fundamental studies utilizing conventional rotating disk electrode (RDE) setups with more applied MEA research cell configurations [58]. Subsequently, at the beginning of this thesis, it was adapted to explore the acidic OER [59–62], wherein enhanced performance was achieved for a particular Ir catalyst through electrode feeding with liquid water rather than gas [63]. This setup then reflects similarities with flow-cell configurations and was introduced as porous transport electrode (PTE) setup.

Initiation

As a starting point, pure nickel (Ni) catalysts were synthesized using the hydrogen bubble template (HBT) method. These experiments were conducted on carbon paper-based gas diffusion layers (GDLs). Subsequently, Ir-based catalyst samples were evaluated to demonstrate the concept of the alkaline OER in the GDE. The Ir benchmark exhibited superior performance compared to the pure Ni benchmark, as anticipated, and initial current densities of approximately 100 mA cm^{-2} were achieved at $V_{RHE} = 1.8$ V for the most competitive Ni samples.

Proof of concept

Following the evaluation of initial tests, it became apparent that substantial improvements were necessary to address the performance issues in the GDE compared to literature values in a liquid environment. Consequently, several modifications were

implemented: the substrate was altered from carbon paper to metallic meshes, a PTFE sealing was introduced for sealing and to ensure consistent gas flow, various membrane configurations and diaphragms were assessed, and electrochemical protocols in continuous and pulsed potentiostatic and galvanostatic modes were investigated. The pure Ni benchmark catalyst remained particularly unchanged during this period, as it was not anticipated to impede electrochemical performance. Additionally, the electrolyte concentration was maintained at a constant 4 M KOH throughout the investigation. The outcomes of this study are summarized in Manuscript I.

Further development

Following the successful implementation of the GDE in alkaline OER, numerous avenues for further investigation emerged. Several potentially more promising Ni alloy catalyst candidates were synthesized in accordance with the proof of concept study. Subsequent investigations revealed that focusing on the iron-nickel (FeNi) alloy space yielded more direct research outcomes compared to diverse multi-metal Ni alloy compositions. Furthermore, it became apparent that no published study had comprehensively examined the entire FeNi alloy space at varying Fe:Ni ratios under elevated current densities exceeding 2 A cm^{-2}. Consequently, the research focus was directed toward this specific aspect, and the summarized results are presented in Manuscript II.

2. Methods

This section provides an overview of the methodologies employed in the thesis. The catalytic coatings were electroplated utilizing the hydrogen bubble template (HBT) method, which is elaborated at the commencement of this chapter. Subsequently, an overview of the physical characterization methods is presented, followed by the methodology to characterize the catalysts electrochemically and its data preparation. The theoretical principles of standard characterization methods are not expounded upon in detail, but are summarized, and specific references are incorporated.

Electrochemical syntheses of catalytical coatings

The HBT approach was used to electrodeposit catalytic coatings. This is a versatile and efficient method for electrodepositing catalytic coatings with enhanced surface areas and porosity [64,65]. This technique employs the concurrent evolution of hydrogen gas bubbles during the electrodeposition process to generate a template for the formation of a porous metallic structure. In conventional electroplating of homogeneous films, hydrogen evolution must be suppressed. Consequently, this method represents an atypical electrodeposition approach.

As the metal ions are reduced and deposited onto the substrate, the hydrogen bubbles generated at the cathode surface act as templates, resulting in the formation of interconnected pores and channels within the growing metal film. The resulting catalytic coatings produced by the HBT method exhibit a highly porous, three-dimensional architecture with increased surface area and hence improved mass transport properties. For individual metals, the three-dimensional architecture can exhibit diverse structures. For instance, copper (Cu) demonstrates a distinct three-dimensional foam-like structure, with fine surface dendrite structures resembling fir trees [66–68], while zinc (Zn) displays pellet-like dendrites [69,70], and Cu-Zn co-deposition combines these microstructures [71]. Cu and Zn are recognized for their efficacy in the HBT method and are frequently employed for the CO_2 electro-reduction reaction.

For nickel (Ni), initial HBT approaches date back to the year 2000, and the resulting microstructures exhibit cauliflower-like dendritic formations [72,73]. Initially, the application of Raney-Nickel catalysis was proposed [74], and subsequently [75], alternative de-alloying strategies, such as those utilizing gold (Au) [76], in conjunction with the HBT method, emerged for electrochemical sensing applications.

Furthermore, a wider range of metals including silver [77] and noble metals such as Pt and Pd were investigated using HBT [78]. The unique structures obtained offer several advantages for catalytic applications, including enhanced accessibility of reactants to active sites, improved diffusion of products, and increased stability due to the interconnected metallic network. The method allows for precise control over the porosity and morphology of the coatings by adjusting various parameters such as applied potential, electrolyte composition, and deposition time. Additionally, this approach can be applied to a wide range of metals and alloys, making it a versatile technique for synthesizing catalytic materials with tailored properties for specific applications in fields such as energy conversion, environmental remediation, and chemical synthesis.

Pure nickel foams

Nickel electroplating constitutes an important process in global manufacturing, offering enhanced corrosion resistance, increased hardness, and improved aesthetic qualities to diverse metal surfaces [79,80]. This methodology finds extensive application across multiple industrial sectors, including electronics, automotive, aerospace, and consumer goods, where robust and protective surface treatments are essential for extending component longevity and optimizing performance for both decorative and functional coatings.

A commonly used Ni plating solution is the "Watts bath" [81], containing Ni sulphate hexahydrate ($NiSO_4 \cdot 6\ H_2O$, 240 - 300 g l^{-1} (0.9 – 1.1 M)), Ni chloride hexahydrate ($NiCl_2 \cdot 6\ H_2O$, 30 - 90 g l^{-1} (0.1 – 0.4 M)), and boric acid (H_3BO_3, 30 - 45 g l^{-1} (0.5 – 0.7 M)). Bath temperature is typically 40 – 60° C, with a pH = 3.5 - 4.5. The cathode current density typically applied for these baths is 20 – 70 mA cm^{-2}, which results to deposition rates between 25 and 85 µm h^{-1}. The Ni chloride serves dual functions: it enhances the solution conductivity and facilitates the sacrificial Ni anode dissolution. Boric acid functions as a buffer, primarily serving to regulate the pH of the

solution. Due to the cathode efficiency being less than 100 %, there exists a propensity for the pH to increase as hydrogen ions (H$^+$) are discharged, resulting in the typically undesired liberation of hydrogen gas.

The possibilities for bath composition are extensive [82,83]. Further, multi-layer Ni coatings comprising different bath compositions can be implemented, i.e. a relatively thick semi-bright Ni base coating, upon which a thin bright nickel layer is deposited, which typically contains a higher sulphate content.

To ensure a constant electrical field within the bath between the anode and cathode and to obtain reproducible coating results at galvanostatic fixed current densities, a geometric fixation mount was designed and implemented during the electroplating, shown in **Fig. 5**.
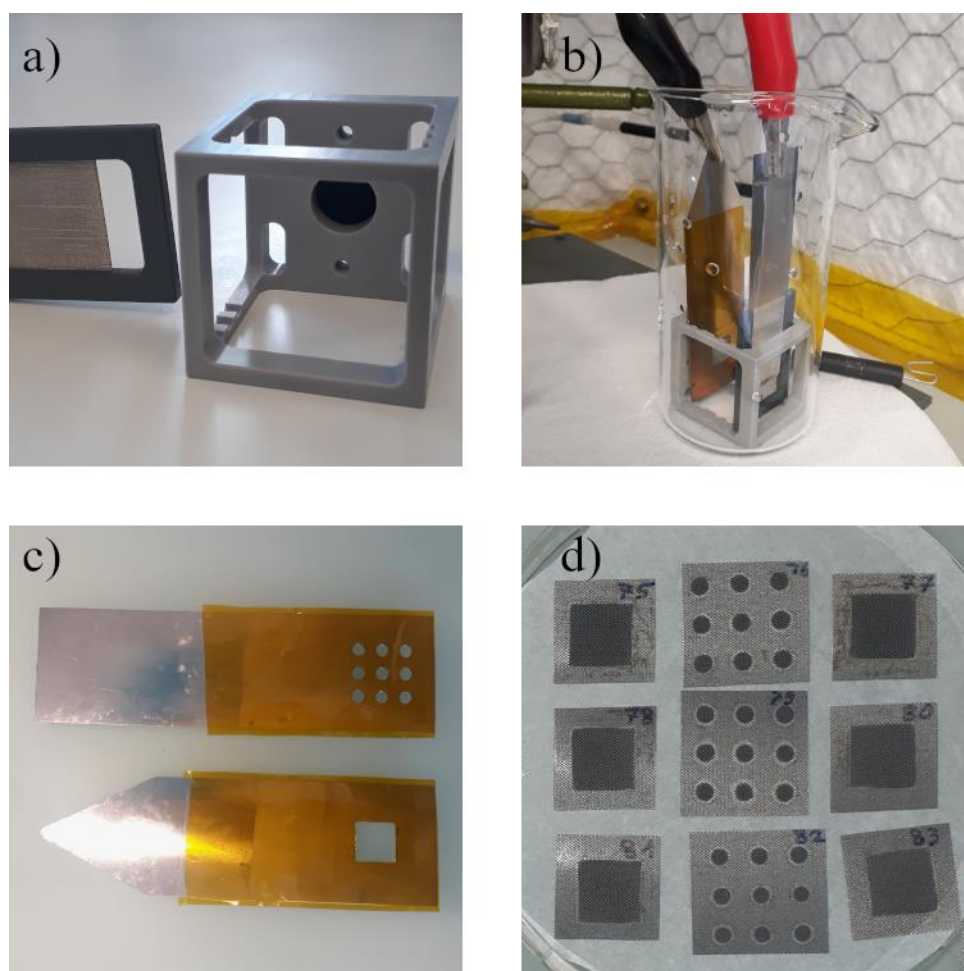
Figure 5: (a) The polymer fixation mount with a sacrificial Ni anode is illustrated. (b) The current source is connected to both electrodes, the plating bath is missing. (c) Electrodeposition masks are displayed, with one designated for 1x1 cm^{-2} deposits and another for GDE sample generation. (d) Ni-based catalysts, electroplated using the HBT technique, are shown.

Ni foams synthesized by the HBT method require different bath concentrations than standard Watts baths, particularly to enhance the solution conductivity, as elevated current densities exceeding 1 A cm^{-2} are applied. HBT Ni foams have been synthesized utilizing both exclusively chloride Ni salt [84–86] and exclusively sulfate Ni salt [73] precursors, alongside different electrolytes, complexing agents, and buffers.

Initially, for pure Ni HBT foams, the precursor Ni salts (chloride, sulphate, and nitrate) were evaluated at various concentrations, ranging from 0.005 to 0.8 M, with ammonium chloride (NH$_4$Cl) serving as an electrolyte buffer at a high concentration of 1.0 - 2.0 M. The power source employed (Voltcraft, model CPPS-160-42) was software-controlled and enabled the application of high current densities, 1.5 to 4 A cm^{-2}, with rapid ramping and control in the sub-second range. This facilitated the investigation of foams in relation to extended deposition times and enabled reproducible results. The process did not incorporate the ramping of current densities, which can be considered necessary to ensure film adhesion. Furthermore, the power source consists of a two-electrode system without a reference electrode. As voltages significantly exceeding 10 V were required to drive the current, a reference electrode was regarded as unnecessary.

Nickel-alloy foams

The range of metals alloyed in electrodeposited films with Ni is extensive and encompasses Fe, Cr, Co, Cu, W, Zn, and numerous others. A comprehensive overview is provided in various textbooks [87,88].

Principally, all these alloys can be synthesized utilizing the HBT approach. However, co-depositions necessitate additional consideration, due to, for example, anomalous deposition behavior of Ni and Fe [89]. Challenges arise due to the disparate electrodeposition behaviors of the metals, such as variations in reduction potentials, which influence the simultaneous deposition rates. For instance, Ni and Fe exhibit anomalous competition with respect to the electrochemical series for deposition under a given potential [90,91]. The electrochemical series categorizes metals according to their reduction potentials, indicating their relative propensity to accept electrons. Ni, possessing a more positive potential (Ni^{2+} + 2 e$^-$ $\rightleftharpoons$ Ni, E$_0$ = -0.257 V), is expected to deposit faster than iron (Fe^{2+} + 2 e$^-$ $\rightleftharpoons$ Fe, E$_0$ = -0.447 V). Given that Ni exhibits a more noble potential, it would be expected to deposit preferentially over Fe. However, during co-electrodeposition, Fe exhibits preferential deposition over Ni. This deviation

from expected behavior is attributed to factors such as localized pH alterations [92], hydroxide formation [93], and surface adsorption phenomena [94]. Precise control of bath composition, pH, and current density is essential to mitigate these issues.

NiFe co-deposition is of significant importance in the micro electro mechanical systems (MEMS) industry due to the magnetic properties of permalloy (80 at.% Ni, 20 at.% Fe) [95,96]. For the alkaline OER, NiFe alloys are considered a promising catalyst candidate [97–103]. Consequently, a substantial body of literature regarding this co-deposition process is available [104], including pulsed electrodeposition [105].

Chromium (Cr) is alloyed with Ni when addressing corrosion issues [106]. High Cr ratios of 90 at.% can be deposited; however, the Ni-Cr co-deposition is susceptible to cracking. Consequently, post-treatments such as annealing can be implemented to mitigate these issues [107]. Electrodeposited Cr-Ni-Fe alloys can be synthesized from divalent (Cr^{2+}), trivalent (Cr^{3+}), and hexavalent (Cr^{6+}) Cr solutions [108]. Stainless steel (SS) is characterized as a material with Fe as its primary constituent and a minimum of 10.5 at.% Cr [109]. While the Fe-Cr system serves as the foundation, SS incorporates various additional alloying elements to enhance specific properties. For instance, Ni is incorporated to promote the formation of austenite crystal structure. Consequently, SS containing Ni has been investigated for the alkaline OER [110,111].

The electrodeposition of a "Cantor alloy" [112,113] (referred to as the concept underlying high entropy alloys (HEA), with approximately equimolar proportions of CrMnFeCoNi) is feasible [114]. Electrodeposited HEAs have been demonstrated [115,116] and are considered a scalable synthesis approach [117] among others such as arc-melting.

Given our research group's focus on nanoelectrocatalysis and interest in HEA, an exploratory study was initiated to investigate multi-metal Ni alloy foams. This investigation aimed to examine the broad alloy space for potential Ni-based HBT foam catalysts. The "Cantor" composition was prepared in plating solutions primarily utilizing sulfate-based precursor salts; however, in the case of Cr, the $Cr_2(SO_4)_3$ is trivalent, in contrast to the divalent nature of the other metal precursors. Furthermore, the compositions were extended to include Cu and Zn, which are known for their favorable HBT behavior. The results, which will be discussed in the subsequent section,

were challenging to interpret, particularly with regard to the stability of the plating bath.

To streamline the methodology and based on preliminary findings, the investigation was focused on NiFe foams. Although HBT NiFe foams electrodeposited from chloride precursor salt have been reported [118], sulfate-based plating solutions were utilized to synthesize various Ni:Fe ratios.

Physical characterization methods

The electrodeposited samples were initially examined utilizing a digital microscope (Keyence, VHX-6000). This methodology facilitated preliminary developments for HBT syntheses of novel plating bath compositions, enabling current density evaluations through visual inspection of the resultant film morphologies. Furthermore, precise area measurements and geometrical properties could be determined. The calibration was verified with a specific calibration plate for the selected magnifications.

Scanning electron microscopy

Scanning electron microscopy (SEM) is a sophisticated instrument used for the optical characterization of materials, offering high-resolution imaging capabilities for the analysis of surface morphology and microstructure [119]. When applied to HBT foams, SEM enables detailed observation of the pore structure, film thickness via cross-sectioning, and surface features that result from the electrodeposition process.

SE micrographs were acquired using a Zeiss GeminiSEM 450 equipped with SmartSEM 6.05 software. A secondary electron (SE) Everhart-Thornley detector was employed to capture images. For high-resolution and surface-sensitive imaging, an in-lens detector was utilized at low acceleration voltages (approximately 2 kV) and short working distances (WD) of 2 to 3 mm.

During this thesis, a straightforward methodology incorporating liquid nitrogen for cross-sectional examination of samples on carbon paper was implemented. This technique and obtained images resulted in three co-authorships. Furthermore, one image was selected for inclusion in an ACS Catalysis review article [120].

SEM - Energy dispersive X-ray spectroscopy

The combination of SEM and energy dispersive X-ray spectroscopy (SEM-EDS) is ideally suited for evaluating the uniformity of a foam's porous structure, both visually

and elementally, which are essential aspects of this study. SEM delivers detailed surface topography images, while EDS offers the ability to detect and measure elemental composition at specific locations and across regions. An EDS detector identifies X-rays emitted by the specimen, which result from the excitation of electrons by the electron beam and their subsequent transition to lower energy shells within the atom. The X-ray's energies are quantized and element-specific, enabling the identification and quantitative analysis of individual elements in the material. When utilized for HBT foams, SEM-EDS allows for a thorough analysis of the foam's microscopic structure while concurrently mapping the distribution of present elements. This integrated approach is useful for examining the composition and homogeneity of the foam material, as well as identifying any potential contaminants or irregularities that might occur during electrodeposition processes.

The SEM-EDS analysis was conducted by an Oxford Instruments Ultim max 150 photodetector, operated through AZTec software (version 6.0). The instrument settings included a working distance (WD) ranging from 8.3 to 8.7 mm, an acceleration voltage of 15 kV, and a probe current between 200 and 500 pA. In addition to the presented measurements, a separate study of HEA nanoparticles was conducted at EPF Lausanne to identify benefits from an ultra-sensitive EDS detector, Ultim Extreme.

X-ray diffraction

X-ray diffraction (XRD) plays a crucial role in examining the crystalline structure, composition of phases, and microstructural characteristics of crystalline films [121]. A STOE StadiP instrument was employed to obtain XRD patterns using reflection mode and Bragg-Brentano geometry. The device utilized a Cu K_α radiation source (40 keV, 40 mA, $\lambda = 0.1540$ nm) and was controlled through WinXPow software. Diffraction data were collected at 0.1° intervals, with each measurement lasting 30 s, covering a 2θ range from 10° to 90°. A zero-matrix quartz sample holder was used for the analysis.

The metallic crystal structures of Ni, Fe, Ti, and NiFe alloys investigated by XRD in this study were compared with reference crystal structures from the "Crystallography Open Database". The Scherrer equation could be utilized to estimate an average crystallite size [122]. However, due to relatively low signal intensity and limited relevance of bulk properties, this analysis was not pursued. The primary focus was on

detecting metal specifications and the Ni-oxide layer in high-performing samples. XRD has inherent limitations when characterizing thin films, including weak diffraction signals for very thin layers, potential interference from substrate peaks, and reduced sensitivity to amorphous or nanocrystalline phases. For thin films, the grazing incidence (GI-XRD) methodology is typically employed; however, it was not available for the given experimental setup.

Gas diffusion electrode setup

Gas diffusion electrodes (GDEs) are well-established devices employed in electrochemical production and research. The typical composition of GDEs includes a porous conductive material, also referred as porous transport layer (PTL), serving as the electrode foundation, decorated with catalytic components to promote the intended chemical reaction. Hence, GDEs enable chemical reactions to occur at extensive interfaces of the three-phase boundary and enhance the transport of gaseous reactants or products. They serve for diverse applications, including the electrosynthesis of chloride gas in brine electrolysis [123], where they are commonly referred to as oxygen depolarized cathodes or air cathodes [124] to suppress H_2 evolution. It is noteworthy that this industry typically does not utilize the H_2 produced as a by-product, but rather disposes of it due to additional cost associated with investments in H_2 treatment and storage. For the commercial electrosynthesis of hydrogen peroxide (H_2O_2) in a GDE, oxygen passes through the rear of a hydrophobic porous electrode before undergoing reduction at the interface between the solid and liquid phases [125].

In fuel cell devices, gaseous H_2 and O_2 react to liberate electricity, thus representing a model example of GDE devices. Fuel cells can operate in alkaline media, such as anion exchange membrane fuel cells (AEMFC) [126–128], or under acidic conditions as proton exchange membrane fuel cells (PEMFC) [129–131]. Further areas of research for GDEs encompass metal-air batteries [132–134], wherein GDEs function as air cathodes, and in the electrochemical reduction of CO_2 [135,136] and N_2 [137] to value-added products. Consequently, GDEs play a crucial role in connecting gas-phase reactants with underlying electrochemical processes, influencing mass transport, charge transfer, and overall device efficiency. Furthermore, they facilitate electrochemical reactions involving gaseous species at higher current densities compared to electrodes utilized in purely liquid environments.

Marini et al. (2012) presented a concept involving a circulating liquid alkaline electrolyte that separates both anodic and cathodic GDE compartments [138]. As previously discussed in the Introduction regarding alkaline AEMWE, GDEs to evolve cathodic H_2 were adopted as dry cathodes. Consequently, in the investigation of the anodic OER via a GDE, the terminology "dry anode" is introduced.

"Dry anode" setup for the alkaline OER

Although research has been conducted on OER in GDEs [139,140], it remains a relatively understudied area in comparison to other aspects of AEM technology. Our investigation presents an anodic GDE approach for AEMWE, introduced as dry anode conditions. In this configuration, the catalyst is not immersed in a liquid medium, in contrast to conventional anodes supplied with a liquid electrolyte. Instead, the anode is subjected to a humidified gas stream and the catalyst is in a zero-gap configuration connected to the membrane. The schematic representation is illustrated in **Fig. 6 (a)**.
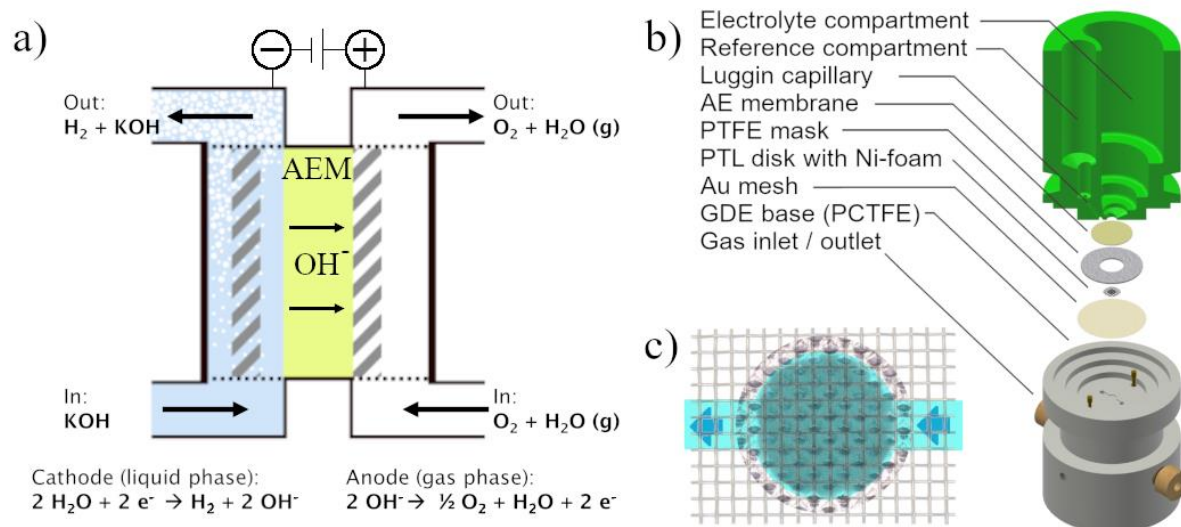
Figure 6: (a) Schematic representation of the "dry anode": The cathode compartment generates H_2 in an alkaline environment. Hydroxide transport across the AEM enables the anodic OER, where humidified O_2 is purged in and exits the compartment with increased partial pressure. (b) Setup drawing: The catalytically coated PTL is connected via Au mesh and pins to the WE and is in direct contact with the membrane, which is separating the liquid electrolyte compartment from the GDE. An RHE (RE) senses the AEM via a Luggin capillary, minimizing solution resistance. (c) The gas flow field is illustrated in blue. A catalytic disk substrate is on top of the current collecting Au mesh. The flow field was extruded from the GDE base body, running beneath the entire catalytic disk ($\o = 3$ mm).

Figure 6 (b) illustrates the GDE setup. The PTL with electrodeposited catalyst layer is connected via Au mesh and Au pins as the working electrode (WE) to the potentiostat. The AE membrane, which separates the liquid electrolyte from the GDE, is in direct contact at its lower surface with the catalyst, thus forming a zero-gap configuration. The reference electrode (RE) is connected via Luggin capillary to the upper surface of the AE membrane, thereby minimizing solution resistance. The electrolyte compartment was filled with 4 M KOH and initially agitated with a stirrer, subsequently equipped with a software-controlled ultrasonic horn homogenizer (**Fig. 7**). A Pt coil counter electrode (CE) served to evolve H_2 in the caustic potash.

Gas bubble formation management

A significant challenge for high reaction rates, specifically high current densities, of gaseous products pertains to gas bubble formation. Typically, bubbles function as insulators in environments where high electrical conductivity is required. While bubbles are not anticipated to be a significant concern at the dry anode due to their expected minimal occurrence in the gaseous atmosphere, bubble-related phenomena are observed in the liquid cathode department between the RE and the Luggin capillary, as well as on the membrane surface, as evidenced by the presence of adhered bubbles post-experiment. These bubbles exert a significant impact on the measurement, as they substantially increase the internal resistances and deactivate potential active sites, thereby affecting the performance [141]. Furthermore, this phenomenon could potentially lead to misinterpretation of catalyst degradation.

The occurrence of bubble formation is prevalent, and numerous bubble elimination strategies have been proposed [142]. These include ultrasonic (US) pulses [143,144], pressure swings [145], electrolyte flow rate adjustments [146], and the orientation of the electrodes submerged in liquid electrolyte. Electrode orientation is preferentially vertical or inverted in comparison to conventional RDE configurations, to facilitate the "natural" release of bubbles [147]. The used setup is therefore in the favorable orientation, however, for sticking or micro bubbles the orientation is not sufficient to overcome the issue. Therefore, ultrasonic pulses were applied to degas the cathode compartment for specifically determined threshold values (described in the subsequent section: Electrochemical measurements).

An ultrasonic horn homogenizer (Shanghai Ultrasonic Instrument Co., Model SC-150, 30 kHz, horn $\varnothing$ = 3 mm) was integrated via software control, implemented using a custom-developed LabVIEW program designed specifically for this application, to the potentiostat and a power source (Voltcraft, model CPPS-160-42), see Fig. 7.
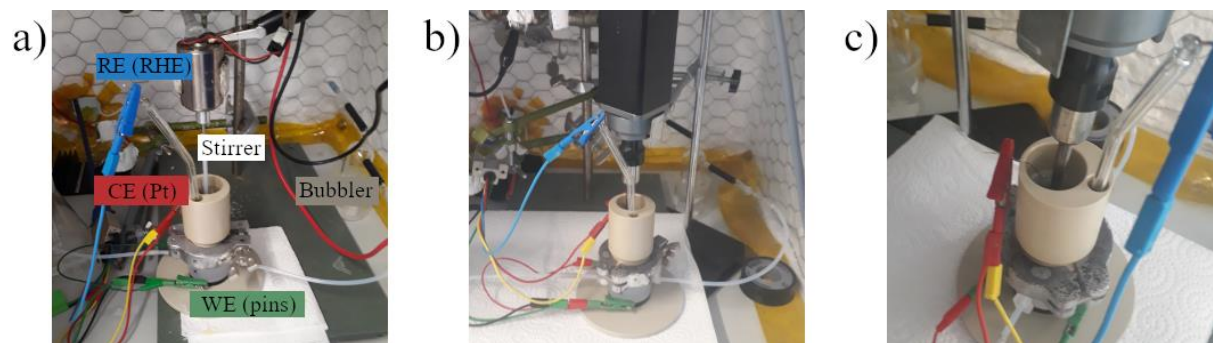
Figure 7: (a) A photograph of the GDE setup. WE, RE, and CE are indicated. To humidify the O_2, a bubbler was used. Initially, a PTFE stirrer was utilized to mitigate gas bubble formation on the membrane surface. (b) The analogous apparatus, with an installed US horn for degassing bubbles. (c) A magnified view depicting visible liquid KOH.

Electrochemical measurements

Measurements were performed using an ECi 210 potentiostat from Nordic Electrochemistry ApS, operated by EC4 DAQ 4.2.142 software. To monitor bubble formation and facilitate subsequent iR-correction of measured potentials, a 5 kHz AC signal with either 5 or 10 mV amplitude was overlaid on all electrochemical measurement protocols. This allowed for the measurement of system resistances and maintenance of comparable measurement conditions. The solution resistance, also known as the uncompensated resistance, is defined as the high-frequency resistance (HFR) measured between the working electrode (WE) and the Luggin capillary end (HFR$_{Sol.}$), primarily representing membrane resistance in this setup. Similarly, cell resistance is defined as the HFR between the WE and CE (HFR$_{Cell}$). During experiments, solution and cell resistance were monitored in situ. Upon reaching threshold values of 2 Ω for HFR$_{Sol.}$ or 16 Ω for HFR$_{Cell}$, software-controlled activation of the ultrasonic horn was implemented to mitigate bubble formation during electrochemical measurements. This activation protocol included an immediate application of a 12 V US pulse for one second, followed by a retention time of two

seconds. If the resistance persisted, the applied voltage was incrementally increased for each subsequent pulse up to 24 V.

Cyclic Voltammetry

Cyclic voltammograms (CVs) were recorded at various scan rates and in different potential windows. Initially, samples were examined using a brief CV protocol to verify correct assembly and functionality of the setup. These protocols also served as an "activation" process to form the oxidized surface of Ni, specifically $Ni(OH)_2$, or the oxidized surface of the Ni alloy catalytic layer for subsequent measurements.

For electrochemical active surface area (ECSA) measurements, a straightforward CV protocol was employed to measure the double-layer capacitance [148]. Prior to CV measurements for ECSA, the samples underwent oxidation to incorporate the surface oxide characteristics.

For low-current regime analysis, CV was employed at scan rates of 5 mV s^{-1} [149].

Potentio- and galvanostatic pulses

This investigation employs pulsed electrochemistry to evaluate quasi steady-states, driven by multiple contributing factors. It was demonstrated that at high current densities, pulsing can enhance the performance of water splitting due to bubble retention [150–152]. In initial samples, which were characterized potentiostatically, the current response decreased by more than 10 % within one minute. Upon reinitiating the measurement using the same sample, the initial current response recovered, followed by rapid degradation. Consequently, pulsed potentiostatic measurements were conducted to preserve as much of the initial performance as possible. Furthermore, due to the coupling of electrolyzers with intermittent electricity from renewable sources, rapid system responses are preferable. The pulsed electrolyzer approach can potentially address this challenge [153,154]. Considering that pulsed electrolysis is utilized in accelerated stress tests [155,156], the application of pulses in this study is unlikely to obscure or artificially enhance the results. Moreover, this methodology enables the assessment of the entire measurement period, rather than selectively choosing a time interval toward the conclusion of a particular steady-state duration, which is subsequently averaged, facilitating unbiased statistical analysis. Consequently,

applying a pulsed approach to determine quasi steady-states was considered appropriate.

Initially, pulsed potentiostatic steps were employed to mitigate the application of excessive potential, which was particularly crucial for samples on carbon tape. As the research progressed, improved performances were anticipated, and higher potentials were tolerated. Subsequently, it became evident that a transition to galvanostatic pulses was necessary, as electrolyzers are typically characterized by their potential response at specified current densities.

Data curation

Analysis of the potentiostat datasets was conducted using Jupyter notebook (version 6.3.0), which was set up within Anaconda Navigator (version 2.0.3). The resulting data was visualized using Matplotlib (version 3.7.4). These tools are open-source, Python-based software, and the availability of the raw data and source code would be desirable in accordance with the principle of full transparency.

Each sample's data was stored in a discrete folder, named according to the sample name and measurement type. Typically, a series of samples was enumerated with a prefix indicating their composition, such as FeNixy. The sample nomenclature was then formatted as FeNixy_dz, where "z" identified disk z of the synthesized FeNixy. The measurement type, either CV or galvanodynamic, was included to categorize the data appropriately. For example, a representative folder designation would be FeNi82_d2_galvanodynamic. Within these folders, the raw datasets were archived for subsequent evaluation.

Previously described, the measured potential response for a pulsed galvanostatic protocol was characterized as quasi steady-state. The following section provides a systematic explanation to elucidate the examination of data for a specific protocol, serving as a model for the evaluation procedure of pulsed datasets.

The experimental protocol involved applying a galvanostatic current density for 6 seconds, followed by a 1-second period of no current. This cycle was repeated 50 times for each geometrical current density, resulting in 5 minutes of active OER per investigated current density. The total duration per current density was 350 seconds, with 86 % of that time dedicated to active OER. Using a 10 Hz measurement

frequency, 3500 readings were collected per absolute current, per applied potential vs. the RHE, per applied cell potential, per HFR$_{Sol.}$ and per HFR$_{Cell}$ for each current density.

1) List the files in the directory, with each current density corresponding to one *.tdms file.

```
[1]: import os
     os.listdir()
     os.listdir('data/FeNi082_d2_galvanodynamic1')
```

```
[1]: ['Macro.EC_Macro',
      'Macro_Log.txt',
      'Steps_162614.tdms',
      'Steps_163204.tdms',
      'Steps_163755.tdms',
      'Steps_164345.tdms',
      'Steps_164936.tdms',
      'Steps_165526.tdms']
```

2) Import the *.tdms data by selecting the corresponding files and assign it to NumPy data arrays. Repeat this process for all current densities, i.e., 6 times.

```
[2]: import numpy as np
     import pandas as pd
     import matplotlib.pyplot as plt
     from nptdms import TdmsFile

     # file import and define data frames 500mA cm-2
     tdms_file = TdmsFile.read("data/FeNi082_d2_galvanodynamic1/Steps_162614.tdms")
     tdms_file_groups = tdms_file.groups()
     tdms_file_df = tdms_file.as_dataframe()

     tdms_file_groupEC_i_FeNi082_d2_s1_500mamppulsed = tdms_file_groups[0]['i']
     tdms_file_groupEC_t_FeNi082_d2_s1_500mamppulsed = tdms_file_groups[0]['Time']
     tdms_file_groupEC_E_FeNi082_d2_s1_500mamppulsed = tdms_file_groups[0]['E']
     tdms_file_groupEC_R_FeNi082_d2_s1_500mamppulsed = tdms_file_groups[0]['Z_E']
     tdms_file_groupEC_Rcell_FeNi082_d2_s1_500mamppulsed =␣
      ↪tdms_file_groups[0]['Z_cell']
     tdms_file_groupEC_Ecell_FeNi082_d2_s1_500mamppulsed =␣
      ↪tdms_file_groups[0]['Ucell']

     current_FeNi082_d2_s1_500mamppulsed =␣
      ↪tdms_file_groupEC_i_FeNi082_d2_s1_500mamppulsed.data
     time_FeNi082_d2_s1_500mamppulsed =␣
      ↪tdms_file_groupEC_t_FeNi082_d2_s1_500mamppulsed.data
```

3) Check the obtained raw dataset with Matplotlib.

FeNiO82_d2_s1_galvanostatic_pulsed
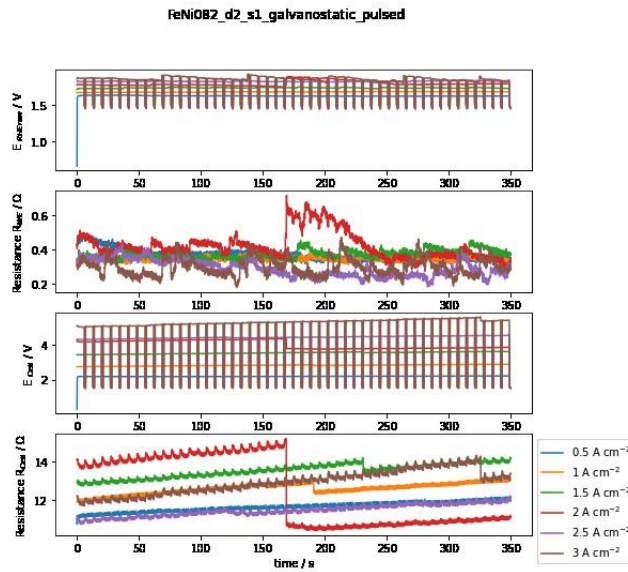
4) Calculate the iR-correction by multiplying the $HFR_{Sol.}$ with the absolute current.

```
[6]:  # calculate iR-drop of every datapoint:
      iR_drop_FeNi082_d2_s1_500mamppulsed = resistivity_FeNi082_d2_s1_500mamppulsed *␣
       ↪current_FeNi082_d2_s1_500mamppulsed
      iR_drop_FeNi082_d2_s1_1amppulsed = resistivity_FeNi082_d2_s1_1amppulsed *␣
       ↪current_FeNi082_d2_s1_1amppulsed
      iR_drop_FeNi082_d2_s1_1500mamppulse d= resistivity_FeNi082_d2_s1_1500mamppulsed␣
       ↪* current_FeNi082_d2_s1_1500mamppulsed
```

5) Subsequently, subtract the obtained iR-correction from the measured potential and assign the results to new arrays designated as iR-corrected potentials.

```
# compute the iR-corrected potentials
pot_iRcorr_FeNi082_d2_s1_500mamppulsed = potential_FeNi082_d2_s1_500mamppulsed␣
 ↪- iR_drop_FeNi082_d2_s1_500mamppulsed
pot_iRcorr_FeNi082_d2_s1_1amppulsed = potential_FeNi082_d2_s1_1amppulsed -␣
 ↪iR_drop_FeNi082_d2_s1_1amppulsed
pot_iRcorr_FeNi082_d2_s1_1500mamppulsed =␣
 ↪potential_FeNi082_d2_s1_1500mamppulsed - iR_drop_FeNi082_d2_s1_1500mamppulsed
```

6) Normalize the absolute current to the current density in A cm^{-2}.

```
[7]:  # normalize current to A / cm2

      current_FeNi082_d2_s1_500mamppulsed=(current_FeNi082_d2_s1_500mamppulsed/0.0707)
      current_FeNi082_d2_s1_1amppulsed=(current_FeNi082_d2_s1_1amppulsed/0.0707)
      current_FeNi082_d2_s1_1500mamppulsed=(current_FeNi082_d2_s1_1500mamppulsed/0.
       ↪0707)
```

7) Create index arrays in ascending order based on normalized current densities.

```
[8]: #sorting array in ascending order for currents with maintained indices of arrays

     # Get the indices that would sort the array of currents
     sorted_indices_500mamp = np.argsort(current_FeNi082_d2_s1_500mamppulsed)
     sorted_indices_1amp = np.argsort(current_FeNi082_d2_s1_1amppulsed)
     sorted_indices_1500mamp = np.argsort(current_FeNi082_d2_s1_1500mamppulsed)
```

8) Create the sorted arrays, based on the sorted indices, for the normalized current, iR-corrected potentials and HFR$_{Sol.}$ for all current densities.

```
# Sort currents and other arrays based on the sorted indices
sorted_current_FeNi082_d2_s1_500mamppulsed =␣
 ↪current_FeNi082_d2_s1_500mamppulsed[sorted_indices_500mamp]
sorted_pot_iRcorr_FeNi082_d2_s1_500mamppulsed =␣
 ↪pot_iRcorr_FeNi082_d2_s1_500mamppulsed[sorted_indices_500mamp]
sorted_resistivity_FeNi082_d2_s1_500mamppulsed =␣
 ↪resistivity_FeNi082_d2_s1_500mamppulsed[sorted_indices_500mamp]
```

9) Check the obtained data.
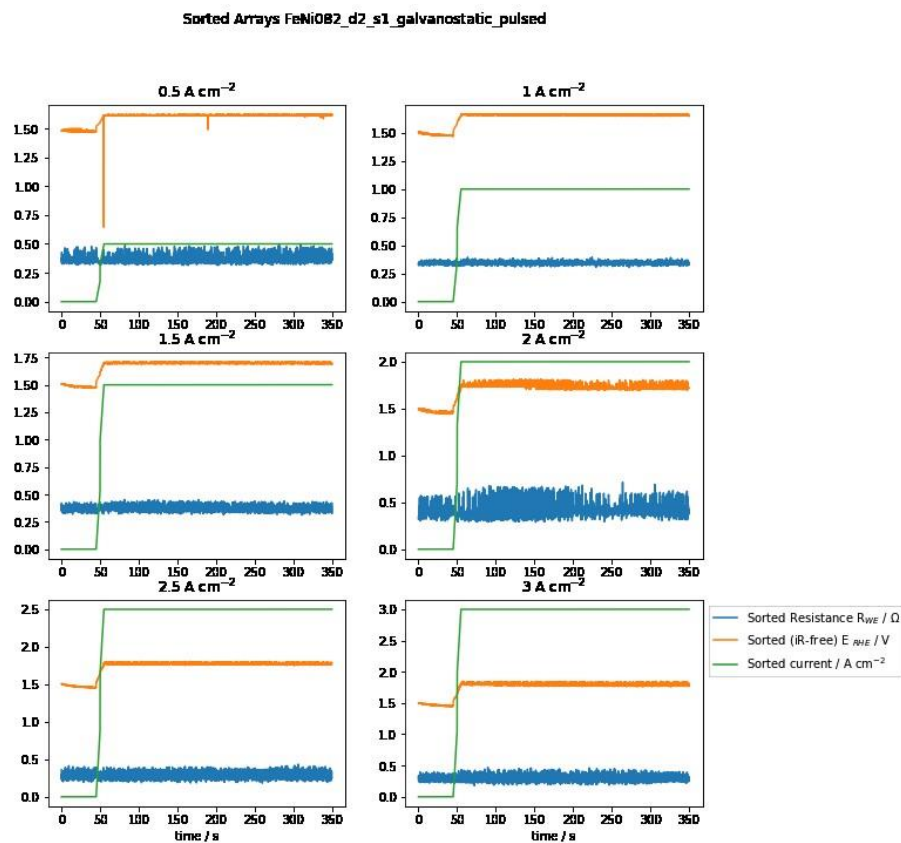
10) Ensure the selection of only iR-corrected potentials that effectively experience the assigned normalized current density, i.e., from 55 seconds onwards.

Sorted Arrays FeNi082_d2
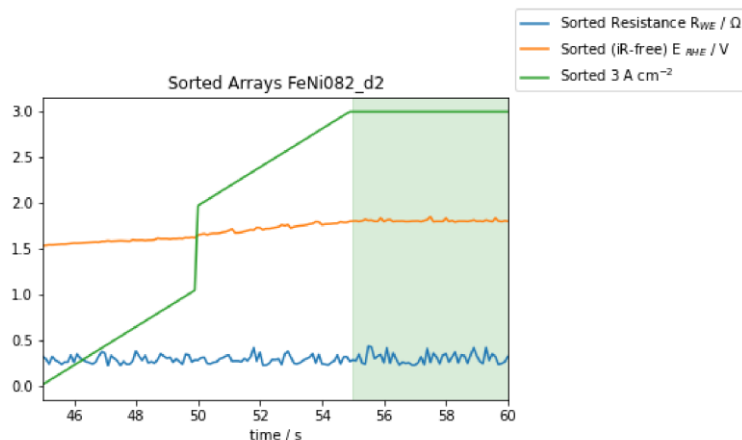
11) Generate new arrays, comprising solely the iR-corrected potentials of the designated normalized current density.

```
pot_iRcorr_FeNi082_d2_s1_500mamppulsed_selection =␣
 ↪sorted_pot_iRcorr_FeNi082_d2_s1_500mamppulsed[550: 3499]
pot_iRcorr_FeNi082_d2_s1_1amppulsed_selection =␣
 ↪sorted_pot_iRcorr_FeNi082_d2_s1_1amppulsed[550: 3499]
pot_iRcorr_FeNi082_d2_s1_1500mamppulsed_selection =␣
 ↪sorted_pot_iRcorr_FeNi082_d2_s1_1500mamppulsed[550: 3499]
```

12) Export the iR-corrected potential and current density arrays as a single NumPy array for subsequent analysis, ensuring the inclusion of the sample identifier.

```
[21]: #create the data array of corrected potentials and currents for export

      # Create a 6x2 array, where each element is an array of 2950 elements
      data_FeNi082_d2 = np.empty((6, 2), dtype=object)

      # Fill each element with an array of 2950 elements
      for i in range(6):
          for j in range(2):
              data_FeNi082_d2[i, j] = np.zeros(2949)


      data_FeNi082_d2[0,0] = pot_iRcorr_FeNi082_d2_s1_500mamppulsed_selection
      data_FeNi082_d2[1,0] = pot_iRcorr_FeNi082_d2_s1_1amppulsed_selection
      data_FeNi082_d2[2,0] = pot_iRcorr_FeNi082_d2_s1_1500mamppulsed_selection
      data_FeNi082_d2[3,0] = pot_iRcorr_FeNi082_d2_s1_2amppulsed_selection
      data_FeNi082_d2[4,0] = pot_iRcorr_FeNi082_d2_s1_2500mamppulsed_selection
      data_FeNi082_d2[5,0] = pot_iRcorr_FeNi082_d2_s1_3amppulsed_selection
```

Using the obtained sample arrays, which consist exclusively of iR-corrected potentials at designated current densities, various graphical representations - such as histograms, box plots, mean values with standard deviations, and medians - can be generated by selecting appropriate functions from the extensive Python library. The analysis

31

accommodates both individual and combined samples by correctly assessing the data structure within the generated NumPy arrays.

One advantage of this data handling approach is that it minimizes the likelihood of sample mix-ups, as each script requires manual input of the corresponding raw data filename. Additionally, quality assessments are conducted at multiple stages within the script execution, with results plotted to facilitate robust sample comparisons and establish precise exclusion criteria. Conversely, a limitation is the absence of higher degree in automation.

Moreover, the execution of standardized plotting functions is restricted to measurements following identical electrochemical protocols. The sorting of arrays is not automated; rather, the number of elements is manually specified in the code. Typically, the same script is used for data analysis for a specific protocol, meaning that any changes to the measurement protocol necessitate adaptations to the scripts.

In summary, data curation with Jupyter enables statistical evaluation once the data are properly organized in the NumPy structure. Handling large datasets with spreadsheet software for pulsed electrochemical protocols is less convenient and more error-prone. Precise control of data operations is essential and should be consistently verified at multiple stages. The obtained values were selectively cross-checked, especially when initiating new analysis scripts, using the official EC4.View software from Nordic Electrochemistry ApS to ensure accuracy.

Disclosure of the use of large language model technologies

During the preparation of this thesis, I engaged with large language models (LLMs), specifically Paperpal (V. 2.14.2) and ChatGPT (V. 3.5), to improve the readability and the grammatical quality. Subsequently, comprehensive reviews and editing processes were undertaken, assuming full responsibility for content accuracy. No scientific conclusions or insights, and no references were derived by LLMs.

3. Results and discussion

This section presents a concise overview of the thesis findings and examines the principal points from the two manuscripts. It commences with a brief review of the initial Ni films, followed by a summary of the publication on the Ni-benchmark foam. The text subsequently addresses Ni alloys combined with various metals, before exploring the significant outcomes of the FeNi alloy investigation.

Initial Ni foams

At first, Ni HBT foams were deposited on large, unmounted carbon tape, while masking a 1x1 cm^{-2} area using a Teflon tape. This approach resulted in inconsistent coating formation, an outcome that could have been anticipated. Consequently, the presented fixation mount (Fig. 5) was developed. The implementation of the software-controlled power source further enhanced reproducibility. Various plating bath compositions were evaluated, including the Watts bath, nickel sulfate (0.05 to 0.8 M) alone or in combination with nickel chloride (0.005 to 0.05 M), and diverse electrolytes such as ammonium chloride (NH_4Cl), nitrate (NH_4NO_3), and boric acid (0.3 to 2.0 M) [72,73,81]. The applied current density was maintained at a constant 3 A cm^{-2} for 45 s per deposition. The resultant films exhibited distinct morphologies, which were visually apparent (**Fig. 8**).
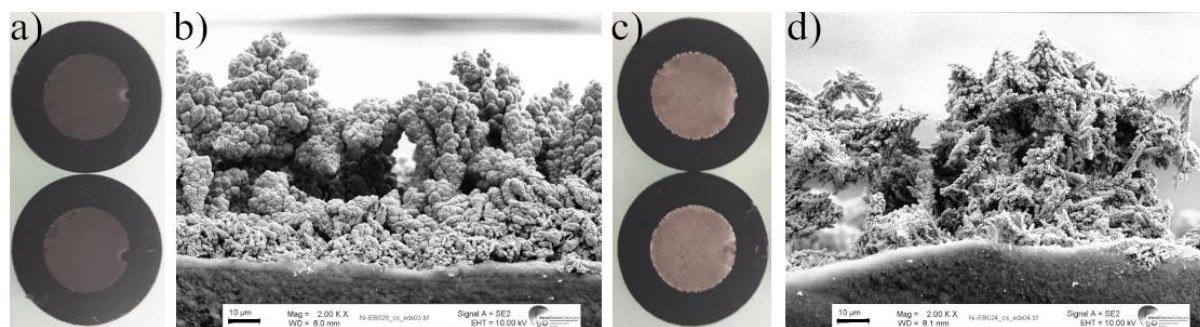
Figure 8: (a) Photograph of two reproduced Ni HPT foams on carbon tape (0.5 M $NiSO_4$ bath conc.). The coated area measured 1 cm^{-2}, i.e. Ø = 1.13 cm. The cross-sectional SE micrograph of the sample is shown in (b): Scale bar is 10 µm, film thickness ~60 µm. Cauliflower subunits are evident. (c) Photograph of two reproduced Ni HBT foams with varying bath composition (0.05 M $NiSO_4$ bath conc.), the films were brighter. (d) The SEM cross-section revealed more pronounced spiked dendrites compared to the previous samples.

The initial OER performance was suboptimal, with CV measurements yielding only approximately 100 mA cm^{-2} at E_{RHE} = 1.8 V. Potentiostatic current responses exhibited rapid decline, e.g. decreasing from approximately 70 to 40 mA cm^{-2} at E_{RHE} = 1.675 V within a 4-minute interval. However, the occurrence of sudden increases in current responses was observed in multiple samples and attributed to gas bubble release. Consequently, pulsed potentiostatic protocols were investigated, resulting in more stable current responses over extended periods. The utilization of carbon paper coated with a hydrophobic micro porous layer (MPL) facilitated testing without a membrane, revealing enhanced film performance by eliminating the membrane from the experimental setup.

Subsequently, metal mesh substrates were implemented (Ti expanded metal and SS woven mesh), as the carbon paper was determined to be an inadequate substrate for this application. The optimal performing Ni foam recipe was identified, and the plating bath was marginally optimized for the preferred Ti substrate. Ti was selected due to its inertness toward alkaline OER, to demonstrate OER activity solely related to the synthesized catalyst. Furthermore, the KOH concentration in the cathodic electrolyte was investigated with respect to performance. 4 M KOH exhibited significantly superior performance compared to the lower concentrated 1 M KOH, which was attributed to lower HFR$_{Sol.}$ for higher concentrated KOH. Additionally, a decrease in current response was observed toward the conclusion of the potentiostatic pulses, which could be mitigated by incorporating a PTFE stirrer into the liquid KOH electrolyte. These subsequent development steps resulted in an increased current response of approximately 200 mA cm^{-2} at E_{RHE} = 1.8 V for a Ni HBT foam on a Ti PTL.

A significant advancement was achieved through the introduction of a novel upper cathodic compartment, which incorporated the Luggin capillary contacting the membrane instead of the liquid electrolyte compartment [57]. This modification further reduced HFR$_{Sol.}$, resulting in current responses exceeding 1 A cm^{-2} at E_{RHE} = 1.9 V in cyclic voltammograms. These results necessitated verification and reproduction, with effective catalyst coating areas required not to exceed the normalization factor of the experimental setup. Additionally, further experimental details were to be elucidated in preparation for the initial manuscript.

Manuscript I

Description

The research article titled "Attaining Substantially Enhanced Oxygen Evolution Reaction Rates on Ni Foam Catalysts in a Gas Diffusion Electrode Setup" explores the use of a pure Ni foam benchmark catalysts in a dry anode configuration to compare OER rates to an identical electrode submerged in liquid environment. The study addresses the challenge of achieving high current densities, a critical factor regarding competitiveness for future application.

Primary conclusions

High current densities were achieved by a pure Ni foam catalyst, synthesized via HBT electrodeposition, which demonstrated to sustain high OER current densities of 4 A cm^{-2} under quasi steady-state conditions at an iR-corrected set potential of 2.1 V$_{RHE}$. (**Fig. 9**). This performance was attributed to the porous structure of the Ni foam integrated to the GDE setup, which facilitates enhanced mass transport of gaseous products.
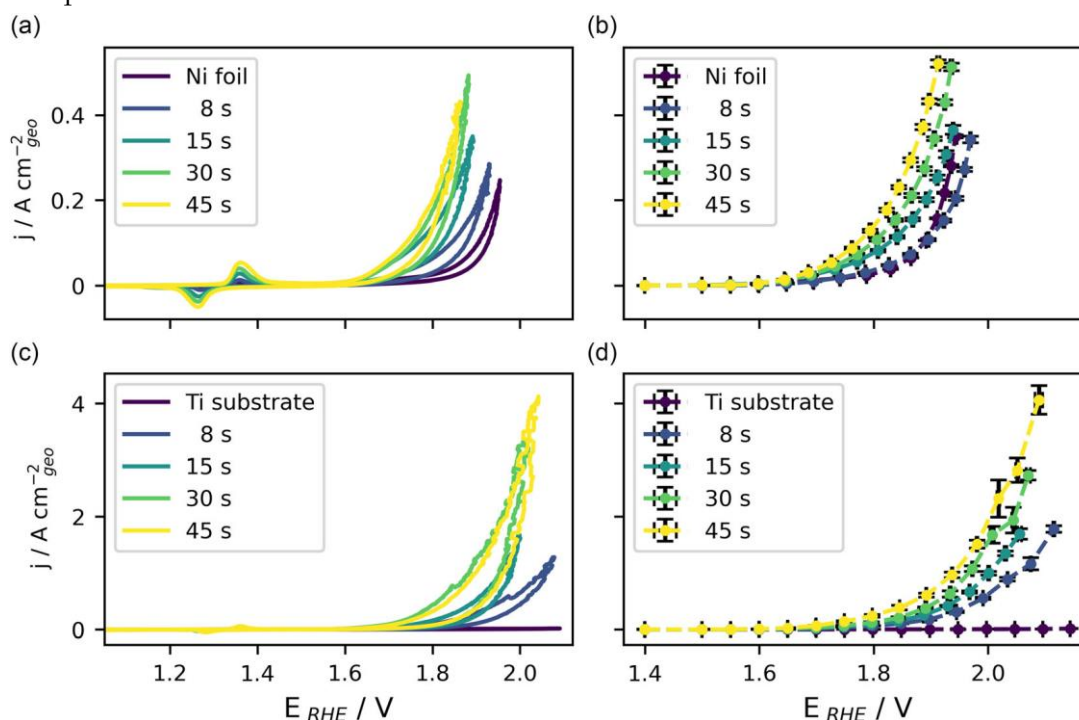
Figure 9: iR-corrected CVs and quasi steady-state current densities for Ni foams with varying deposition times in both liquid electrolyte and dry anode configurations. CVs were measured at a 50 mV s^{-1} scan rate. The results are presented as follows: a) CVs in liquid environment; b) quasi steady-states in liquid environment; c) CVs in GDE setup; d) quasi steady-states in GDE setup.

The dry anode implementation revealed an advantage compared to liquid environment, and demonstrated superior performance against traditional liquid electrolyte setups at high current densities, providing up to 30 % higher activity at an iR-corrected set potential of 1.9 V_{RHE} (**Fig. 10**). This outcome is predominantly influenced by the applied iR-correction, which impedes a rigorous comparison. Both electrodes underwent identical electrochemical protocols; however, due to elevated solution resistance in the liquid environment, the iR-correction for liquid-immersed electrodes was substantially higher. This highlights a common issue in electrochemistry, where different potential correction methods in different setups and environments are applied, e.g. hardware compensation or posterior iR-correction [157]. This comparison could have further be clarified by the application of galvanostatic investigations.
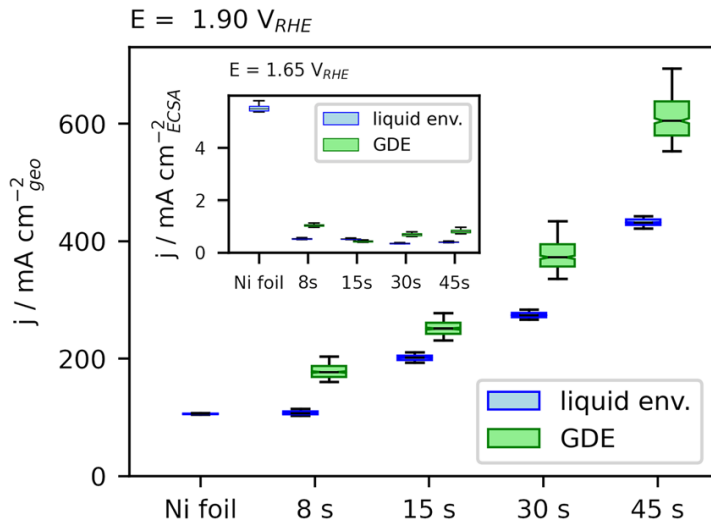
Figure 10: Analysis of current density measurements in the diffusion-limited region at set iR-corrected potential of 1.90 V_{RHE} under quasi steady-state conditions, represented by box plots, indicates that the GDE configuration demonstrates approximately 30 % higher activity compared to catalytic foams in a liquid medium. Inset: Conversely, in the kinetic-limited region at 1.65 V_{RHE}, the current densities normalized to the ECSA demonstrate comparable values between the GDE setup and the liquid electrolyte environment, whereas the pure Ni exhibits the highest activity.

ECSA investigation revealed a correlation between the ECSA and OER activity, suggesting that extended deposition periods increase surface area and enhance current density [158]. However, upon normalization to "intrinsic" nickel activity, the Ni foam catalysts demonstrate reduced activity compared to a planar Ni foil [159–162]. The implementation of a pure Ni catalyst simplified the methodology; however, various factors for a precise electrochemical surface analysis render the "correct" intrinsic

activity subject to speculative assumptions. Such factors include the surface lattice structures, their type of surface oxide, the penetration depth of this and/or several oxide types, and the controversially discussed aspect of Fe impurities in the alkaline electrolyte [163–167]. Concurrently, investigations have incorporated Fe impurities into the electrolyte to enhance the performance of NiFe OER electrocatalysts [141], which represents a viable strategy for high current rates.

The intended detection of the surface oxide via XRD measurement was unsuccessful, leading to the conclusion that the oxide layers were thin, measuring only a few nanometers. The introduction of box plots in this paper facilitated the subsequent data-driven analysis. Stability tests were conducted for one hour, during which no degradation was observed. In retrospect, this duration was insufficient to conclusively determine the stability of catalytic coatings. Nevertheless, stability testing was not a primary objective of the investigation and was conducted as a standard procedure in electrochemical research. Furthermore, at the time, no software control over the US horn was available, and the US pulses were manually applied, which impeded extended stability testing.

Author contributions

Etienne Berner: Sample synthesis and preparation, electrochemical measurements, data curation, GDE setup optimization, SEM-EDS and XRD measurements, paper writing.
Gustav K. H. Wiberg: GDE setup optimization, reviewing, editing.
Matthias Arenz: Supervision, conceptualization, reviewing, editing.

Multi-metal Ni alloys

The initial objective was, in analogy to HEA nanoparticles, to deposit a HEA HBT foam. As the concept of HEA originated from Cantor [112] and this alloy contains Ni and Fe, it seemed appropriate to attempt its synthesis using HBT. In this paragraph, the metal compositions are presented according to the periodic table for the purpose of simplification.

The Cantor alloy comprises approximately equimolar CrMnFeCoNi. The corresponding sulfate salts were available in-house, with the exception of $Cr_2(SO_4)_3$. Subsequently, in an initial investigation, a total metal concentration analogous to the first manuscript of 0.2 M, with each metal at 0.04 M concentration, was selected for the plating bath.

Cr was introduced as CrO_3, and 1.5 M NH_4Cl was utilized as the electrolyte. The sacrificial anode comprised pure Ni. This bath composition exhibited high instability and resulted in immediate precipitations following deposition (**Fig. 11**). A parallel plating bath without the addition of Cr demonstrated improved stability post-deposition. $CrCl_2$ as divalent Cr and $Cr_2(SO_4)_3$ as trivalent Cr were investigated, with more stable plating baths observed for the trivalent Cr. However, the stability of the plating baths remained a concern regarding reproducibility, and several carbon-based sacrificial anodes were evaluated due to the observed enhanced Ni content in subsequent films resulting from Ni anode dissolution. The substitution of $(NH_4)_2SO_3$ for NH_4Cl did not improve stability. An additional challenge was the high current density required for the Cantor composition to form a foam-like structure, which amounted to 6 A cm^{-2}, leading to inherent problems with, for example, burning carbon foam anodes. The addition of several complexing agents, including ethylenediaminetetraacetic acid (EDTA), ascorbic acid, and boric acid, was minimally effective.
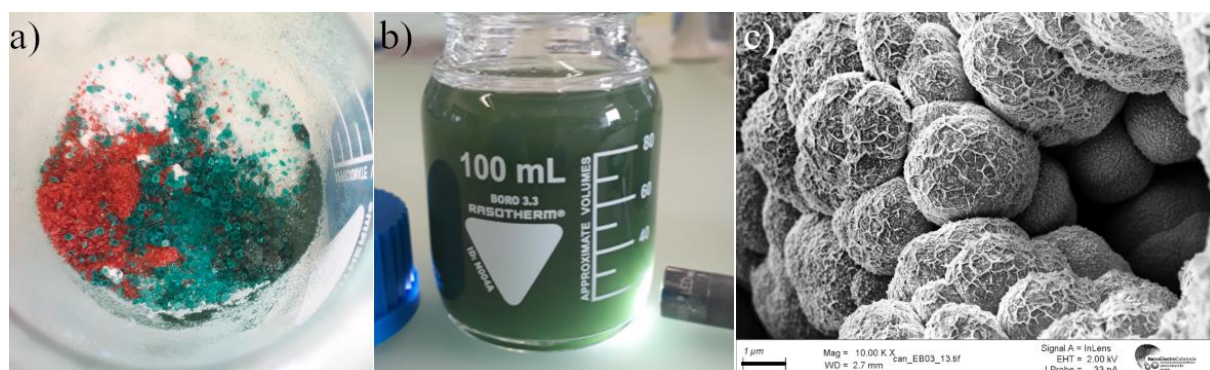
Figure 11: Cantor alloy impressions: (a) The metal sulphates for the plating bath. (b) Precipitation after the deposition is evident. (c) SE micrograph of a HBT foam containing CrMnFeCoNi deposited at 6 A cm^{-2} for 30 s, scale bar is 1 µm.

Furthermore, three additional compositions were investigated: MnFeCoNiCu, FeCoNiCuZn, and CrFeNiCuZn. The suitability of substituting these metals, particularly Cu and Zn, for HBT foams was evident, as foam structures were obtained at relatively moderate current densities of 1 A cm^{-2} [69,70], and more stable plating baths could be achieved. The compositions of the synthesized foams varied with varying current densities, as anticipated [88], which rendered a systematical research more complex. Nevertheless, the activity toward OER was not as promising for the majority

of synthesized samples as for the parallel developed NiFe alloy foams, and consequently, it was determined not to further investigate multi-metal Ni alloy foams. The acquired knowledge, however, proved valuable for the FeNi alloy plating bath compositions, which are presented in the subsequent section.

Manuscript II

Description

The preprint titled "Investigation of FeNi alloy foams at high oxygen evolution reaction rates using a dry anode setup in alkaline environment" examines the performance of porous FeNi alloy HBT foams as electrocatalysts for the OER in alkaline water electrolysis. The research introduces the terminology of a dry anode configuration for AEMWE, in analogy to the recently introduced dry cathode. Thereby the anode is not submerged in a liquid electrolyte but instead exposed to humidified gas. The primary objective of this investigation is to elucidate the composition-activity relationship of porous FeNi alloy foams toward the OER performance, with particular emphasis on high current densities, by applying rigorous statistical analysis to demonstrate reproducibility.

Primary conclusions

The developed dry anode configuration presents a research platform for the systematic investigation of promising OER catalysts for alkaline environments under high reaction rates. The 11 different FeNi alloy compositions, ranging from 93 to 2 at.% Fe, were synthesized utilizing the HBT method, and represent a relatively fine dispersed alloy distribution [98,168]. Particular emphasis was placed on stable plating solutions, which encompassed the development of sulfate-based plating baths for the HBT methodology. All synthesized FeNi foams exhibited relatively active electrocatalysis for alkaline OER. Employing a slow CV scan rate of 5 mV s^{-1}, Tafel analysis and "onset potentials" were derived for comparative purposes with the existing literature. Alloys containing 60 to 40 at.% Fe demonstrated Tafel slopes below 40 mV dec^{-1} and "onset potentials" between 260 and 290 mV to achieve 10 mA cm^{-2}. Although CVs to asses these benchmarks is discussed controversy [149,169], the measured activities demonstrate anticipated values for typical FeNi electrocatalyst.

The study comprised a total of 88 measured sample disks (8 disks for each composition), with dispersed data. This dispersion was attributed to several factors, including manual cell assembly, misalignment of disks, uncontrolled gas flow field, and uneven initial $HFR_{Sol.}$ values. Reproducibility, which is expected but occasionally overlooked in electrochemistry [170], was addressed with a second synthesis of similar alloy Fe:Ni content and a rigorous statistical approach. All measured data were included, except for 6 sample disks, which failed to meet defined qualification criteria and were subsequently remeasured.
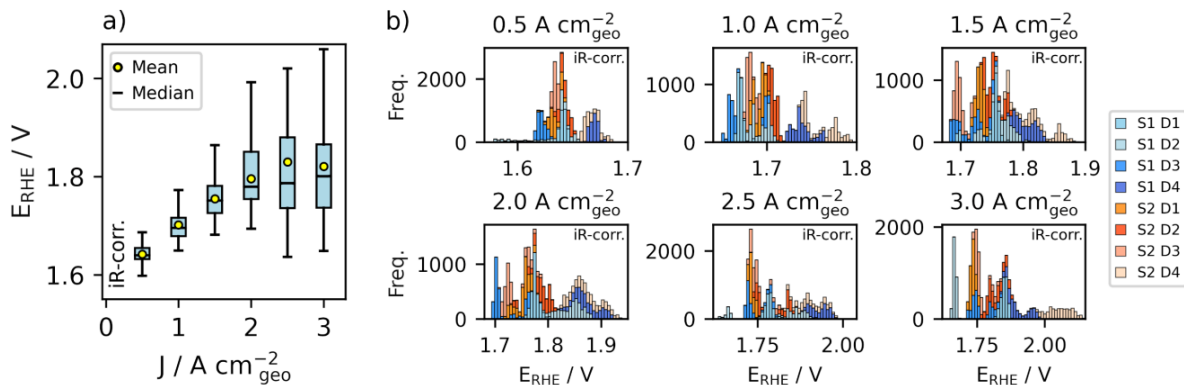
Figure 12: Analysis of the 59 at.% Fe alloy foam, encompassing eight distinct disk measurements from two separate syntheses (S1 and S2). The data comprises 144k points, based on five-minute OER per disk and galvanostatic pulsed current density, measured at 10 Hz frequency. (a) The potential required at the applied current density is illustrated in a box plot. Generally, mean and median values align closely. However, this specific alloy shows a slight deviation of the mean toward higher potentials compared to the median at current densities exceeding 2 A cm^{-2}. At a pulsed current density of 3 A cm^{-2}, there is a 20 mV difference between mean and median. (b) Corresponding histograms elucidate the data structure and individual sample contributions. The initial synthesis's four disks (D1-D4) are represented in blue, while the repeated synthesis's disks are shown in red. The plot excludes outliers and does not employ a specifically normalized bin size.

The applied boxplot representation of the required potentials to drive the pulsed galvanostatic current densities between 0.5 and 3 A cm^{-2} was determined to be the most appropriate method for illustrating the dispersed data. In **Fig. 12**, in addition to the box plot, the corresponding histograms are presented. Each individual sample disk is identifiable, with the blue color code for the initial synthesis (S1: D1 – D4) and the red color code for the resynthesized samples (S2: D1 – D4). This approach was adopted in accordance with the full transparency philosophy [171]. Minor deviations between

mean and median values are explained in the manuscript. The obtained values are representative and counterbalance individual measurements, thereby obviating the need to present "representative" samples.

The obtained potentials for high pulsed current densities of 1, 2, and 3 A cm⁻² are presented in **Fig. 13**. The observed activity differences at low current densities become less pronounced, and in certain instances, such as for the invar alloy, the measurements yielded results contrary to expectations.

The stability test was significantly prolonged compared to the first manuscript, extending to 10 h at a pulsing rate of 3 A cm⁻². Sample degradation was observed, potentially attributable to mechanical stress from pulsing, anode desiccation [53], or corrosion of the Ti PTL. Furthermore, the $HFR_{Sol.}$ was evaluated during the active OER pulse and retention times, revealing a relative increase of 18 % for $HFR_{Sol.}$ during active OER. This observation underscores the importance of accurate iR determination for subsequent data processing and interpretation of electrochemical performance [141]. In conclusion, the synthesized catalyst lacks durability, and additional research is required to improve its longevity. Utilizing a dry anode proves to be an effective approach for evaluating stability at high currents over long durations.

Author contributions

Etienne Berner: Sample synthesis and preparation, electrochemical measurements, data curation, GDE setup optimization, SEM-EDS and XRD measurements, conceptualization, paper writing.

Gustav K. H. Wiberg: GDE setup optimization, reviewing, editing.

Matthias Arenz: Supervision, conceptualization, reviewing, editing.
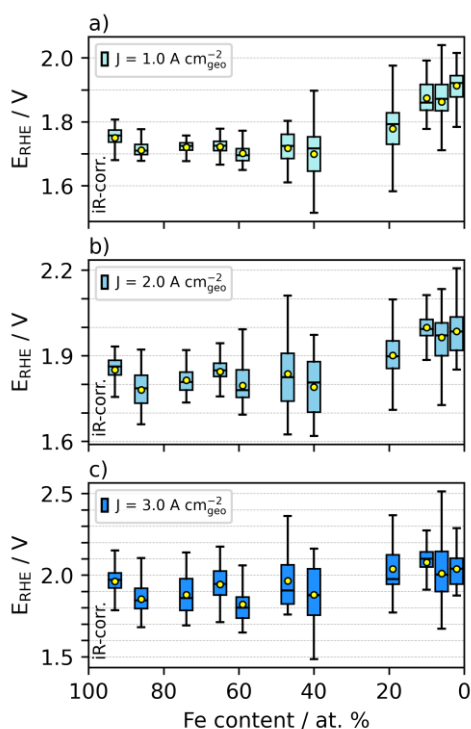
Figure 13: Box plots to display the galvanostatic current densities at 1 (a), 2 (b), and 3 (c) A cm⁻².

4. Conclusions and perspectives

Key conclusions

This dissertation explored the alkaline OER using Ni-based foams synthesized via galvanically deposited hydrogen bubble templating. The investigations during this thesis demonstrated a significant potential of GDE setups with dry anode configurations for advancing AEMWE technology. The experimental installation reached substantial OER rates, with current densities reaching 4 A cm^{-2} at room temperature under quasi steady-states, illustrating the feasibility of operation under ambient conditions. The dry anode offers appreciable advantages, including enhanced mass transport of evolved oxygen compared to conventional liquid electrolyte systems and reduced ohmic resistance, thereby enhancing process efficiency. The OER performance is facilitated through the driving force of hydroxides migrating through the AEM toward the positively charged anode. The catalytic coating of the PTL is in direct contact with the membrane, forming a zero-gap configuration. A liquid film on the catalyst surface facilitates hydroxide conductivity, which is crucial for promoting high OER rates. This process resulted in more effective water splitting at elevated currents, which has the potential to contribute to efficient hydrogen production.

Following an initial investigation into the operational characteristics of the setup through the implementation of a pure Ni benchmark HBT foam, the obtained results were subsequently corroborated by exploring the more reactive NiFe alloy space. A rigorous statistical approach was employed to mitigate individual sample performance variations, thereby facilitating unbiased data presentation and reproducibility.

The use of pulsed electrolysis allowed for the possible adaptation to intermittent current supply typical of renewable energy sources. The presented studies adjusted to rapid electrochemical responses, facilitating the achievement of quasi steady-state conditions. Although pulsed electrolysis is not yet extensively researched, it holds the potential to play a more significant role in the future. Stability testing revealed a gradual degradation after an extended period of pulsing at 3 A cm^{-2}, indicating a need for further optimization toward more robustness.

The management of bubbles in the liquid cathodic compartment requires particular attention. Gas bubble formation was successfully anticipated using an ultrasonic horn, and various alternative methods could potentially address this issue.

Future perspectives

Further examination of the stability is required in regard to the presented catalytic coatings, given the observed linear degradation. To address potential corrosion concerns, the usage of stainless steel or Ni-based alloys as PTLs could be considered. A Ti-based PTL was ultimately selected due to its inertness toward the OER, thus allowing for the demonstration of OER activity exclusively associated with the catalytic coating.

Furthermore, additional catalytic sample compositions could be synthesized to explore the catalytic landscape of multi-metal NiFe alloys. This could lead to more active, or more stable catalysts. Concerning the HBT methodology, reducing the applied current density during the synthesis was favorable for large-scale application.

The experimental setup could also be operated under pressure and tested at elevated temperatures to increase catalytic efficiency. This would increase the current densities even further, which ultimately will require consolidated research.

The setup can be implemented as platform with novel catalyst designs at elevated current densities, enabling a more informative stability assessment. Additionally, membrane evaluations at high current loads could be considered.

Final words

Returning to the Introduction, it is evident that the transition to new technologies may span several decades to centuries. It is my hope that this thesis can serve as an inspirational source for future researchers and engineers. The development of a constantly functional dry anode setup took almost three years, and further progress will be necessary before it could be integrated into a practical AEM device and hopefully demonstrate its robustness. Nevertheless, I am optimistic that the tradition of Swiss innovation in water electrolysis technology will continue to make a global impact. This journey has also been personally transformative, profoundly shaping how I interpret, analyze, and present data. These experiences will undoubtedly aid me in articulating my ideas with greater clarity and precision in my future career.

Bibliography

1. Bard, A.J., and Faulkner, L.R. (2001) *Electrochemical Methods: Fundamentals and Applications*, John Wiley & Sons, Inc, New York.

2. Bockris, J.O.M., and Reddy, A.K.N. (2002) *Modern Electrochemistry (Vol 1 & 2)*, Kluwer Academic Publishers, New York.

3. Zollikofer, H. (1928) *Notizen zur Geschichte der schweizerischen Gasversorgung und Gasindustrie*, Fachschriften-Verlag, Zürich.

4. Wullschleger, B. (1943) *Hundert Jahre Gaswerk Bern 1843-1943*, K. J. Wyss Erben AG, Bern.

5. Egger, K.W. (1993) *Von der Gaslaterne zum Erdgas*, Benteli-Werd Verlags AG, Wabern-Bern.

6. Markwalder, H. (1928) *Die Stadtbeleuchtung in Bern 1760 - 1843*, K. J. Wyss Erben, Bern.

7. Strache, H. (1913) *Gasbeleuchtung und Gasindustrie*, Vieweg & Sohn, Braunschweig.

8. İlbaş, M., and Karyeyen, S. (2014) Modelling of combustion performances and emission characteristics of coal gases in a model gas turbine combustor. *Int. J. Energy Res.*, **38** (9), 1171–1180.

9. Schley, P., Beck, M., Uhrig, M., Sarge, S.M., Rauch, J., Haloua, F., Filtz, J.-R., Hay, B., Yakoubi, M., Escande, J., Benito, A., and Cremonesi, P.L. (2010) Measurements of the Calorific Value of Methane with the New GERG Reference Calorimeter. *Int. J. Thermophys.*, **31** (4–5), 665–679.

10. Smolinka, T., and Garche, J. (2022) *Electrochemical Power Sources: Fundamentals, Systems, and Applications*, Elsevier, Amsterdam.

11. Nikolaidis, P., and Poullikkas, A. (2017) A comparative overview of hydrogen production processes. *Renew. Sustain. Energy Rev.*, **67**, 597–611.

12. Turner, J.A. (2004) Sustainable Hydrogen Production. *Science (80-.).*, **305** (5686), 972–974.

13. Schmidt, O. (1899) Apparat zur Elektrolyse von Wasser. 111,113, issued 1899.

14. Godula-Jopek, A. (2015) *Hydrogen Production by Electrolysis*, Wiley-VCH Verlag GmbH & Co, Weinheim.

15. Kreuter, W., and Hofmann, H. (1998) Electrolysis: the important energy transformer in a world of sustainable energy. *Int. J. Hydrogen Energy*, **23** (8), 661–666.

16. Brown, M.J. (1978) Brown Boveri electrolyzers today and in the near future. *Proc. Symp. Ind. Water Electrolysis*, **78**–**4**, 16–23.

17. Müller, J., and Wuellenweber, H. (1978) Lurgi Pressure Electrolysis. *Proc. Symp. Ind. Water Electrolysis*, 1–15.

18. Zdansky, E.A. (1951) Water electrolyzer. 2,739,936, issued 1951.

19. Sandstede, G. (1989) Moderne Elektrolyseverfahren für die Wasserstoff-Technologie. *Chemie Ing. Tech.*, **61** (5), 349–361.

20. Aldag, N., and Sury, S. (2024) Sunfire Builds 100-Megawatt Electrolyzer for RWE.

21. "United Nations Framework Convention on Climate Change (UNFCCC)" (ed.) (2015) Paris Agreement.

22. IEA, "International Energy Agency" (2021) *Global Hydrogen Review 2021*, OECD Publishing.

23. Bockris, J.O.M. (1972) A Hydrogen Economy. *Science (80-.).*, **176** (4041), 1323–1323.

24. Vesborg, P.C.K., and Jaramillo, T.F. (2012) Addressing the terawatt challenge: scalability in the supply of chemical elements for renewable energy. *RSC Adv.*, **2** (21), 7933.

25. Staffell, I., Scamman, D., Velazquez Abad, A., Balcombe, P., Dodds, P.E., Ekins, P., Shah, N., and Ward, K.R. (2019) The role of hydrogen and fuel cells in the global energy system. *Energy Environ. Sci.*, **12** (2), 463–491.

26. Schmidt, O., Hawkes, A., Gambhir, A., and Staffell, I. (2017) The future cost of electrical energy storage based on experience rates. *Nat. Energy*, **2** (8), 17110.

27. Chatenet, M., Pollet, B.G., Dekel, D.R., Dionigi, F., Deseure, J., Millet, P., Braatz, R.D., Bazant, M.Z., Eikerling, M., Staffell, I., Balcombe, P., Shao-Horn, Y., and Schäfer, H. (2022) Water electrolysis: from textbook knowledge to the latest scientific strategies and industrial developments. *Chem. Soc. Rev.*, **51** (11), 4583–4762.

28. Nuttall, L., and Russell, J. (1980) Solid polymer electrolyte water electrolysis—development status. *Int. J. Hydrogen Energy*, **5** (1), 75–84.

29. Ito, H., Maeda, T., Nakano, A., and Takenaka, H. (2011) Properties of Nafion membranes under PEM water electrolysis conditions. *Int. J. Hydrogen Energy*, **36** (17), 10527–10540.

30. Grot, W.G. (1982) Nafion® Membrane and its Applications, in *Electrochemistry*

in Industry, Springer US, Boston, MA, pp. 73–87.

31. Seitz, L.C., Dickens, C.F., Nishio, K., Hikita, Y., Montoya, J., Doyle, A., Kirk, C., Vojvodic, A., Hwang, H.Y., Norskov, J.K., and Jaramillo, T.F. (2016) A highly active and stable IrO x /SrIrO 3 catalyst for the oxygen evolution reaction. *Science (80-.).*, **353** (6303), 1011–1014.

32. Lettenmeier, P., Majchel, J., Wang, L., Saveleva, V.A., Zafeiratos, S., Savinova, E.R., Gallet, J.J., Bournel, F., Gago, A.S., and Friedrich, K.A. (2018) Highly active nano-sized iridium catalysts: Synthesis and operando spectroscopy in a proton exchange membrane electrolyzer. *Chem. Sci.*, **9** (14), 3570–3579.

33. Kibsgaard, J., and Chorkendorff, I. (2019) Considerations for the scaling-up of water splitting catalysts. *Nat. Energy*, **4** (6), 430–433.

34. Ayers, K., Danilovic, N., Ouimet, R., Carmo, M., Pivovar, B., and Bornstein, M. (2019) Perspectives on Low-Temperature Electrolysis and Potential for Renewable Hydrogen at Scale. *Annu. Rev. Chem. Biomol. Eng.*, **10** (1), 219–239.

35. Yu, H., Danilovic, N., Wang, Y., Willis, W., Poozhikunnath, A., Bonville, L., Capuano, C., Ayers, K., and Maric, R. (2018) Nano-size IrOx catalyst of high activity and stability in PEM water electrolyzer with ultra-low iridium loading. *Appl. Catal. B Environ.*, **239** (May), 133–146.

36. Melke, J., Maletzko, A., Gomez Villa, E.D., Bornet, A., Wiberg, G.K.H., Arenz, M., Sandig-Predzymirska, L., Thiere, A., Charitos, A., Stelter, M., Wang, Z., Pitscheider, S., Bertheussen, E., Pedersen, C.M., Finsdóttir, S., Kokborg, M.S., Berman, D.G., Dalvang, S., Müller, S.S., Seidel, F., Seselj, N., Höglinger, M., Kartusch, S., Eder, J., Macherhammer, M., Trattner, A., and Kallesøe, C. (2024) Recycalyse – New Sustainable and Recyclable Catalytic Materials for Proton Exchange Membrane Electrolysers. *Chemie Ing. Tech.*, **96** (1–2), 126–142.

37. Schuler, T., Weber, C.C., Wrubel, J.A., Gubler, L., Pivovar, B., Büchi, F.N., and Bender, G. (2024) Ultrathin Microporous Transport Layers: Implications for Low Catalyst Loadings, Thin Membranes, and High Current Density Operation for Proton Exchange Membrane Electrolysis. *Adv. Energy Mater.*, **14** (7), 1–12.

38. Carmo, M., Fritz, D.L., Mergel, J., and Stolten, D. (2013) A comprehensive review on PEM water electrolysis. *Int. J. Hydrogen Energy*, **38** (12), 4901–4934.

39. Miller, H.A., Bouzek, K., Hnat, J., Loos, S., Bernäcker, C.I., Weißgärber, T., Röntzsch, L., and Meier-Haack, J. (2020) Green hydrogen from anion exchange membrane water electrolysis: a review of recent developments in critical materials and operating conditions. *Sustain. Energy Fuels*, **4** (5), 2114–2133.

40. Du, N., Roy, C., Peach, R., Turnbull, M., Thiele, S., and Bock, C. (2022) Anion-

Exchange Membrane Water Electrolyzers. *Chem. Rev.*, **122** (13), 11830–11895.

41. Sugawara, Y., Sankar, S., Miyanishi, S., Illathvalappil, R., Gangadharan, P.K., Kuroki, H., Anilkumar, G.M., and Yamaguchi, T. (2023) Anion Exchange Membrane Water Electrolyzers: An Overview. *J. Chem. Eng. Japan*, **56** (1).

42. Vincent, I., and Bessarabov, D. (2018) Low cost hydrogen production by anion exchange membrane electrolysis: A review. *Renew. Sustain. Energy Rev.*, **81** (February 2017), 1690–1704.

43. Chen, N., Paek, S.Y., Lee, J.Y., Park, J.H., Lee, S.Y., and Lee, Y.M. (2021) High-performance anion exchange membrane water electrolyzers with a current density of 7.68 A cm -2 and a durability of 1000 hours. *Energy Environ. Sci.*, **14** (12), 6338–6348.

44. Zheng, Y., Ma, W., Serban, A., Allushi, A., and Hu, X. (2024) Anion Exchange Membrane Water Electrolysis at 10 A·cm-2 Over 800 Hours. *Angew. Chemie Int. Ed.*, e202413698.

45. Wan, L., Liu, J., Lin, D., Xu, Z., Zhen, Y., Pang, M., Xu, Q., and Wang, B. (2024) 3D-ordered catalytic nanoarrays interlocked on anion exchange membranes for water electrolysis. *Energy Environ. Sci.*, **17** (10), 3396–3408.

46. Santoro, C., Lavacchi, A., Mustarelli, P., Di Noto, V., Elbaz, L., Dekel, D.R., and Jaouen, F. (2022) What is Next in Anion-Exchange Membrane Water Electrolyzers? Bottlenecks, Benefits, and Future. *ChemSusChem*, **15** (8).

47. Li, D., Motz, A.R., Bae, C., Fujimoto, C., Yang, G., Zhang, F.-Y., Ayers, K.E., and Kim, Y.S. (2021) Durability of anion exchange membrane water electrolyzers. *Energy Environ. Sci.*, **14** (6), 3393–3419.

48. Krivina, R.A., Lindquist, G.A., Beaudoin, S.R., Stovall, T.N., Thompson, W.L., Twight, L.P., Marsh, D., Grzyb, J., Fabrizio, K., Hutchison, J.E., and Boettcher, S.W. (2022) Anode Catalysts in Anion-Exchange-Membrane Electrolysis without Supporting Electrolyte: Conductivity, Dynamics, and Ionomer Degradation. *Adv. Mater.*, **34** (35), 1–10.

49. Henkensmeier, D., Najibah, M., Harms, C., Žitka, J., Hnát, J., and Bouzek, K. (2021) Overview: State-of-the Art Commercial Membranes for Anion Exchange Membrane Water Electrolysis. *J. Electrochem. Energy Convers. Storage*, **18** (2).

50. Lim, A., Kim, H., Henkensmeier, D., Jong Yoo, S., Young Kim, J., Young Lee, S., Sung, Y.-E., Jang, J.H., and Park, H.S. (2019) A study on electrode fabrication and operation variables affecting the performance of anion exchange membrane water electrolysis. *J. Ind. Eng. Chem.*, **76**, 410–418.

51. Xu, D., Stevens, M.B., Cosby, M.R., Oener, S.Z., Smith, A.M., Enman, L.J.,

Ayers, K.E., Capuano, C.B., Renner, J.N., Danilovic, N., Li, Y., Wang, H., Zhang, Q., and Boettcher, S.W. (2019) Earth-Abundant Oxygen Electrocatalysts for Alkaline Anion-Exchange-Membrane Water Electrolysis: Effects of Catalyst Conductivity and Comparison with Performance in Three-Electrode Cells. *ACS Catal.*, **9** (1), 7–15.

52. Wang, R., Ohashi, M., Ishida, M., and Ito, H. (2022) Water transport analysis during cathode dry operation of anion exchange membrane water electrolysis. *Int. J. Hydrogen Energy*, **47** (97), 40835–40848.

53. Koch, S., Disch, J., Kilian, S.K., Han, Y., Metzler, L., Tengattini, A., Helfen, L., Schulz, M., Breitwieser, M., and Vierrath, S. (2022) Water management in anion-exchange membrane water electrolyzers under dry cathode operation. *RSC Adv.*, **12** (32), 20778–20784.

54. Wiberg, G.K.H., Fleige, M., and Arenz, M. (2015) Gas diffusion electrode setup for catalyst testing in concentrated phosphoric acid at elevated temperatures. *Rev. Sci. Instrum.*, **86** (2), 024102.

55. Inaba, M., Jensen, A.W., Sievers, G.W., Escudero-Escribano, M., Zana, A., and Arenz, M. (2018) Benchmarking high surface area electrocatalysts in a gas diffusion electrode: Measurement of oxygen reduction activities under realistic conditions. *Energy Environ. Sci.*, **11** (4), 988–994.

56. Nösberger, S., Du, J., Quinson, J., Berner, E., Zana, A., Wiberg, G.K.H., and Arenz, M. (2022) The Gas diffusion electrode setup as a testing platform for evaluating fuel cell catalysts: a comparative RDE-GDE study. *Electrochem. Sci. Adv.*, (October 2021), 1–12.

57. Wiberg, G.K.H., Nösberger, S., and Arenz, M. (2022) Evolution of a GDE setup: Beyond ambient conditions. *Curr. Opin. Electrochem.*, **36**, 101129.

58. Ehelebe, K., Schmitt, N., Sievers, G., Jensen, A.W., Hrnjić, A., Collantes Jiménez, P., Kaiser, P., Geuß, M., Ku, Y.-P., Jovanovič, P., Mayrhofer, K.J.J., Etzold, B., Hodnik, N., Escudero-Escribano, M., Arenz, M., and Cherevko, S. (2022) Benchmarking Fuel Cell Electrocatalysts Using Gas Diffusion Electrodes: Inter-lab Comparison and Best Practices. *ACS Energy Lett.*, **7** (2), 816–826.

59. Schröder, J., Mints, V.A., Bornet, A., Berner, E., Fathi Tovini, M., Quinson, J., Wiberg, G.K.H., Bizzotto, F., El-Sayed, H.A., and Arenz, M. (2021) The Gas Diffusion Electrode Setup as Straightforward Testing Device for Proton Exchange Membrane Water Electrolyzer Catalysts. *JACS Au*, jacsau.1c00015.

60. Bornet, A., Pittkowski, R., Nielsen, T.M., Berner, E., Maletzko, A., Schröder, J., Quinson, J., Melke, J., Jensen, K.M.Ø., and Arenz, M. (2023) Influence of Temperature on the Performance of Carbon- and ATO-supported Oxygen

Evolution Reaction Catalysts in a Gas Diffusion Electrode Setup. *ACS Catal.*, **13** (11), 7568–7577.

61. Bornet, A., Pitscheider, S., Maletzko, A., Seselj, N., Bertheussen, E., Pedersen, C.M., Wiberg, G.K.H., Melke, J., Kallesøe, C., and Arenz, M. (2024) Beyond RDE characterisation – Unveiling IrRu/ATO OER catalyst stability with a GDE setup. *Electrochim. Acta*, **501** (June).

62. Collantes Jiménez, P., Sievers, G., Quade, A., Brüser, V., Pittkowski, R.K., and Arenz, M. (2023) Gas diffusion electrode activity measurements of iridium-based self-supported catalysts produced by alternated physical vapour deposition. *J. Power Sources*, **569** (January), 232990.

63. Jiménez, P.C., Wiberg, G.K.H., Sievers, G.W., Brüser, V., and Arenz, M. (2023) Bridging the gap between basic research and application: a half-cell setup for high current density measurements of Ir-based oxygen evolution reaction catalysts on porous transport electrodes. *J. Mater. Chem. A*, **11** (37), 20129–20138.

64. Plowman, B.J., Jones, L.A., and Bhargava, S.K. (2015) Building with bubbles: The formation of high surface area honeycomb-like films via hydrogen bubble templated electrodeposition. *Chem. Commun.*, **51** (21), 4331–4346.

65. Popov, K.I., Djokić, S.S., Nikolić, N.D., and Jović, V.D. (2016) *Morphology of Electrochemically and Chemically Deposited Metals*, Springer International Publishing Switzerland, Cham.

66. Shin, H.C., and Liu, M. (2004) Copper foam structures with highly porous nanostructured walls. *Chem. Mater.*, **16** (25), 5460–5464.

67. Nikolić, N.D., Branković, G., Maksimović, V.M., Pavlović, M.G., and Popov, K.I. (2009) Influence of potential pulse conditions on the formation of honeycomb-like copper electrodes. *J. Electroanal. Chem.*, **635** (2), 111–119.

68. Vesztergom, S., Dutta, A., Rahaman, M., Kiran, K., Zelocualtecatl Montiel, I., and Broekmann, P. (2021) Hydrogen Bubble Templated Metal Foams as Efficient Catalysts of CO2 Electroreduction. *ChemCatChem*, **13** (4), 1039–1058.

69. Moreno-García, P., Schlegel, N., Zanetti, A., Cedeno López, A., Gálvez-Vázquez, M.D.J., Dutta, A., Rahaman, M., and Broekmann, P. (2018) Selective Electrochemical Reduction of CO2 to CO on Zn-Based Foams Produced by Cu2+ and Template-Assisted Electrodeposition. *ACS Appl. Mater. Interfaces*, **10** (37), 31355–31365.

70. Luo, W., Zhang, J., Li, M., and Züttel, A. (2019) Boosting CO Production in Electrocatalytic CO 2 Reduction on Highly Porous Zn Catalysts. *ACS Catal.*, **9**

(5), 3783–3791.

71.   Varzi, A., Mattarozzi, L., Cattarin, S., Guerriero, P., and Passerini, S. (2018) 3D Porous Cu–Zn Alloys as Alternative Anode Materials for Li-Ion Batteries with Superior Low T Performance. *Adv. Energy Mater.*, **8** (1), 1–11.

72.   Marozzi, C.A., and Chialvo, A.C. (2000) Development of electrode morphologies of interest in electrocatalysis. Part 1: Electrodeposited porous nickel electrodes. *Electrochim. Acta*, **45** (13), 2111–2120.

73.   Iarchuk, A., Dutta, A., and Broekmann, P. (2022) Novel Ni foam catalysts for sustainable nitrate to ammonia electroreduction. *J. Hazard. Mater.*, **439** (March), 129504.

74.   Gao, Y., and Ding, Y. (2020) Nanoporous Metals for Heterogeneous Catalysis: Following the Success of Raney Nickel. *Chem. – A Eur. J.*, **26** (41), 8845–8856.

75.   An, Y., Tian, Y., Wei, C., Tao, Y., Xi, B., Xiong, S., Feng, J., and Qian, Y. (2021) Dealloying: An effective method for scalable fabrication of 0D, 1D, 2D, 3D materials and its application in energy storage. *Nano Today*, **37**, 101094.

76.   van der Zalm, J., Chen, S., Huang, W., and Chen, A. (2020) Review—Recent Advances in the Development of Nanoporous Au for Sensing Applications. *J. Electrochem. Soc.*, **167** (3), 037532.

77.   Cherevko, S., and Chung, C.-H. (2010) Impact of key deposition parameters on the morphology of silver foams prepared by dynamic hydrogen template deposition. *Electrochim. Acta*, **55** (22), 6383–6390.

78.   Du, R., Jin, X., Hübner, R., Fan, X., Hu, Y., and Eychmüller, A. (2020) Engineering Self-Supported Noble Metal Foams Toward Electrocatalysis and Beyond. *Adv. Energy Mater.*, **10** (11).

79.   Dennis, J.K., and Such, T.E. (1972) *Nickel and chromium plating*, Woodhead Publishing, Cambridge.

80.   Rose, I., and Whittington, C. (2013) *Nickel Plating Handbook*, Nickel Institute, Bruxelles.

81.   Mohanty, U.S., Tripathy, B.C., Singh, P., Keshavarz, A., and Iglauer, S. (2019) Roles of organic and inorganic additives on the surface quality, morphology, and polarization behavior during nickel electrodeposition from various baths: a review. *J. Appl. Electrochem.*, **49** (9), 847–870.

82.   Oriňáková, R., Turoňová, A., Kladeková, D., Gálová, M., and Smith, R.M. (2006) Recent developments in the electrodeposition of nickel and some nickel-based alloys. *J. Appl. Electrochem.*, **36** (9), 957–972.

83. Lee, J.M., Jung, K.K., and Ko, J.S. (2016) Effect of NaCl in a nickel electrodeposition on the formation of nickel nanostructure. *J. Mater. Sci.*, **51** (6), 3036–3044.

84. Siwek, K.I., Eugénio, S., Santos, D.M.F., Silva, M.T., and Montemor, M.F. (2019) 3D nickel foams with controlled morphologies for hydrogen evolution reaction in highly alkaline media. *Int. J. Hydrogen Energy*, **44** (3), 1701–1709.

85. Yu, X., Wang, M., Wang, Z., Gong, X., and Guo, Z. (2016) The structure evolution mechanism of electrodeposited porous Ni films on NH4Cl concentration. *Appl. Surf. Sci.*, **360**, 502–509.

86. Marozzi, C.A., and Chialvo, A.C. (2001) Development of electrode morphologies of interest in electrocatalysis:: Part 2: Hydrogen evolution reaction on macroporous nickel electrodes. *Electrochim. Acta*, **46** (6), 861–866.

87. York, I., and White, E. (2010) *Electrodeposition*, Springer New York, New York, NY.

88. Gamburg, Y.D., and Zangari, G. (2011) *Theory and Practice of Metal Electrodeposition*, Springer New York, New York, NY.

89. Dahms, H., and Croll, I.M. (1965) The Anomalous Codeposition of Iron-Nickel Alloys. *J. Electrochem. Soc.*, **112** (8), 771.

90. Matlosz, M. (1993) Competitive Adsorption Effects in the Electrodeposition of Iron-Nickel Alloys. *J. Electrochem. Soc.*, **140** (8), 2272–2279.

91. Vanysek, P. (2018) Electrochemical Series, in *CRC Handbook of Chemistry and Physics*, 99ed., Taylor & Francis Group, LLC, pp. 665–671.

92. Kieling, V.C. (1997) Parameters influencing the electrodeposition of Ni-Fe alloys. *Surf. Coatings Technol.*, **96** (2–3), 135–139.

93. Vaes, J., Fransaer, J., and Celis, J.-P. (2000) The Role of Metal Hydroxides in NiFe Deposition. *J. Electrochem. Soc.*, **147** (10), 3718.

94. Kang, N.-Y., and Lee, J.-H. (2023) Effects of Bath Composition and Current Density on the Electrodeposition Behavior of Fe–Ni Invar Alloy. *Electron. Mater. Lett.*, **19** (6), 503–509.

95. Myung, N. V., Park, D.-Y., Yoo, B.-Y., and Sumodjo, P.T.A. (2003) Development of electroplated magnetic materials for MEMS. *J. Magn. Magn. Mater.*, **265** (2), 189–198.

96. Zhang, Y., Ding, G., Cai, Y., Wang, H., and Cai, B. (2006) Electroplating of low stress permalloy for MEMS. *Mater. Charact.*, **57** (2), 121–126.

97. Miller, E.L., and Rocheleau, R.E. (1997) Electrochemical Behavior of Reactively Sputtered Iron-Doped Nickel Oxide. *J. Electrochem. Soc.*, **144** (9), 3072–3077.

98. Louie, M.W., and Bell, A.T. (2013) An investigation of thin-film Ni-Fe oxide catalysts for the electrochemical evolution of oxygen. *J. Am. Chem. Soc.*, **135** (33), 12329–12337.

99. Zhao, J., Zhang, J., Li, Z., and Bu, X. (2020) Recent Progress on NiFe-Based Electrocatalysts for the Oxygen Evolution Reaction. *Small*, **16** (51), 1–23.

100. Mohammed-Ibrahim, J. (2020) A review on NiFe-based electrocatalysts for efficient alkaline oxygen evolution reaction. *J. Power Sources*, **448** (October 2019), 227375.

101. Zhou, Y., Wang, Z., Cui, M., Wu, H., Liu, Y., Ou, Q., Tian, X., and Zhang, S. (2024) NiFe-Based Electrocatalysts for Alkaline Oxygen Evolution: Challenges, Strategies, and Advances Toward Industrial-Scale Deployment. *Adv. Funct. Mater.*, **2410618**, 1–26.

102. Asnavandi, M., Yin, Y., Li, Y., Sun, C., and Zhao, C. (2018) Promoting Oxygen Evolution Reactions through Introduction of Oxygen Vacancies to Benchmark NiFe-OOH Catalysts. *ACS Energy Lett.*, **3** (7), 1515–1520.

103. Song, F., Bai, L., Moysiadou, A., Lee, S., Hu, C., Liardet, L., and Hu, X. (2018) Transition Metal Oxides as Electrocatalysts for the Oxygen Evolution Reaction in Alkaline Solutions: An Application-Inspired Renaissance. *J. Am. Chem. Soc.*, **140** (25), 7748–7759.

104. Torabinejad, V., Aliofkhazraei, M., Assareh, S., Allahyarzadeh, M.H., and Rouhaghdam, A.S. (2017) Electrodeposition of Ni-Fe alloys, composites, and nano coatings–A review. *J. Alloys Compd.*, **691**, 841–859.

105. Batchellor, A.S., and Boettcher, S.W. (2015) Pulse-Electrodeposited Ni–Fe (Oxy)hydroxide Oxygen Evolution Electrocatalysts with High Geometric and Intrinsic Activities at Large Mass Loadings. *ACS Catal.*, **5** (11), 6680–6689.

106. Okonkwo, B.O., Jeong, C., and Jang, C. (2022) Advances on Cr and Ni Electrodeposition for Industrial Applications—A Review. *Coatings*, **12** (10), 1555.

107. Huang, C.A., Lin, C.K., and Chen, C.Y. (2009) Hardness variation and corrosion behavior of as-plated and annealed Cr–Ni alloy deposits electroplated in a trivalent chromium-based bath. *Surf. Coatings Technol.*, **203** (24), 3686–3691.

108. Li, B., Lin, A., Wu, X., Zhang, Y., and Gan, F. (2008) Electrodeposition and characterization of Fe–Cr–P amorphous alloys from trivalent chromium sulfate electrolyte. *J. Alloys Compd.*, **453** (1–2), 93–101.

109. Lo, K.H., Shek, C.H., and Lai, J.K.L. (2009) Recent developments in stainless steels. *Mater. Sci. Eng. R Reports*, **65** (4–6), 39–104.

110. Zamanizadeh, H.R., Sunde, S., Pollet, B.G., and Seland, F. (2022) Tailoring the oxide surface composition of stainless steel for improved OER performance in alkaline water electrolysis. *Electrochim. Acta*, **424** (May), 140561.

111. Magnier, L., Cossard, G., Martin, V., Pascal, C., Roche, V., Sibert, E., Shchedrina, I., Bousquet, R., Parry, V., and Chatenet, M. (2024) Fe–Ni-based alloys as highly active and low-cost oxygen evolution reaction catalyst in alkaline media. *Nat. Mater.*, **23** (2), 252–261.

112. Cantor, B., Chang, I.T.H., Knight, P., and Vincent, A.J.B. (2004) Microstructural development in equiatomic multicomponent alloys. *Mater. Sci. Eng. A*, **375**–**377** (1-2 SPEC. ISS.), 213–218.

113. Cantor, B. (2021) Multicomponent high-entropy Cantor alloys. *Prog. Mater. Sci.*, **120** (October 2020), 100754.

114. Aliyu, A., and Srivastava, C. (2019) Microstructure and corrosion properties of MnCrFeCoNi high entropy alloy-graphene oxide composite coatings. *Materialia*, **5** (November 2018), 100249.

115. Glasscott, M.W., Pendergast, A.D., Goines, S., Bishop, A.R., Hoang, A.T., Renault, C., and Dick, J.E. (2019) Electrosynthesis of high-entropy metallic glass nanoparticles for designer, multi-functional electrocatalysis. *Nat. Commun.*, **10** (1), 2650.

116. Shojaei, Z., Khayati, G.R., and Darezereshki, E. (2022) Review of electrodeposition methods for the preparation of high-entropy alloys. *Int. J. Miner. Metall. Mater.*, **29** (9), 1683–1696.

117. Ritter, T.G., Pappu, S., and Shahbazian-Yassar, R. (2024) Scalable Synthesis Methods for High-Entropy Nanoparticles. *Adv. Energy Sustain. Res.*, **5** (8).

118. Arévalo-Cid, P., Vaz, M.F., and Montemor, M.F. (2022) Highly porous FeNi 3D foams produced by one-step electrodeposition: Electrochemical stability and mechanical properties. *Mater. Charact.*, **193** (September), 112311.

119. Goldstein, J.I., Newbury, D.E., Michael, J.R., Ritchie, N.W.M., Scott, J.H.J., and Joy, D.C. (2018) *Scanning Electron Microscopy and X-Ray Microanalysis*, Springer New York, New York, NY.

120. Quinson, J., Kunz, S., and Arenz, M. (2023) Surfactant-Free Colloidal Syntheses of Precious Metal Nanoparticles for Improved Catalysts. *ACS Catal.*, **13** (7), 4903–4937.

121. Cullity, B.D. (1987) *Elements of X-Ray Diffraction*, Addison-Wesley Publishing Company, Reading, Massachusetts.

122. Zhang, S., and Kobayashi, S. (2021) Multilayered structure control for obtaining electrodeposited nanocrystalline iron–nickel alloy with high strength and ductility. *J. Mater. Sci.*, **56** (15), 9484–9498.

123. Moussallem, I., Jörissen, J., Kunz, U., Pinnow, S., and Turek, T. (2008) Chlor-alkali electrolysis with oxygen depolarized cathodes: history, present status and future prospects. *J. Appl. Electrochem.*, **38** (9), 1177–1194.

124. Chatenet, M., Genies-Bultel, L., Aurousseau, M., Durand, R., and Andolfatto, F. (2002) Oxygen reduction on silver catalysts in solutions containing various concentrations of sodium hydroxide - Comparison with platinum. *J. Appl. Electrochem.*, **32** (10), 1131–1140.

125. Perry, S.C., Pangotra, D., Vieira, L., Csepei, L.I., Sieber, V., Wang, L., Ponce de León, C., and Walsh, F.C. (2019) Electrochemical synthesis of hydrogen peroxide from water and oxygen. *Nat. Rev. Chem.*, **3** (7), 442–458.

126. Bidault, F., Brett, D.J.L., Middleton, P.H., and Brandon, N.P. (2009) Review of gas diffusion cathodes for alkaline fuel cells. *J. Power Sources*, **187** (1), 39–48.

127. Xiao, F., Wang, Y.C., Wu, Z.P., Chen, G., Yang, F., Zhu, S., Siddharth, K., Kong, Z., Lu, A., Li, J.C., Zhong, C.J., Zhou, Z.Y., and Shao, M. (2021) Recent Advances in Electrocatalysts for Proton Exchange Membrane Fuel Cells and Alkaline Membrane Fuel Cells. *Adv. Mater.*, **33** (50), 1–38.

128. Dekel, D.R. (2018) Review of cell performance in anion exchange membrane fuel cells. *J. Power Sources*, **375**, 158–169.

129. Mehta, V., and Cooper, J.S. (2003) Review and analysis of PEM fuel cell design and manufacturing. *J. Power Sources*, **114** (1), 32–53.

130. Lapicque, F., Belhadj, M., Bonnet, C., Pauchet, J., and Thomas, Y. (2016) A critical review on gas diffusion micro and macroporous layers degradations for improved membrane fuel cell durability. *J. Power Sources*, **336**, 40–53.

131. Wang, Y., Ruiz Diaz, D.F., Chen, K.S., Wang, Z., and Adroher, X.C. (2020) Materials, technological status, and fundamentals of PEM fuel cells – A review. *Mater. Today*, **32** (February), 178–203.

132. Lee, J., Tai Kim, S., Cao, R., Choi, N., Liu, M., Lee, K.T., and Cho, J. (2011) Metal–Air Batteries with High Energy Density: Li–Air versus Zn–Air. *Adv. Energy Mater.*, **1** (1), 34–50.

133. Wang, Z.-L., Xu, D., Xu, J.-J., and Zhang, X.-B. (2014) Oxygen electrocatalysts

in metal–air batteries: from aqueous to nonaqueous electrolytes. *Chem. Soc. Rev.*, **43** (22), 7746–7786.

134. Pan, J., Xu, Y.Y., Yang, H., Dong, Z., Liu, H., and Xia, B.Y. (2018) Advanced Architectures and Relatives of Air Electrodes in Zn–Air Batteries. *Adv. Sci.*, **5** (4), 1700691.

135. Nguyen, T.N., and Dinh, C.-T. (2020) Gas diffusion electrode design for electrochemical carbon dioxide reduction. *Chem. Soc. Rev.*, **49** (21), 7488–7504.

136. Pan, F., and Yang, Y. (2020) Designing CO2reduction electrode materials by morphology and interface engineering. *Energy Environ. Sci.*, **13** (8), 2275–2309.

137. Rabiee, H., Ge, L., Zhang, X., Hu, S., Li, M., and Yuan, Z. (2021) Gas diffusion electrodes (GDEs) for electrochemical reduction of carbon dioxide, carbon monoxide, and dinitrogen to value-added products: a review. *Energy Environ. Sci.*, **14** (4), 1959–2008.

138. Marini, S., Salvi, P., Nelli, P., Pesenti, R., Villa, M., Berrettoni, M., Zangari, G., and Kiros, Y. (2012) Advanced alkaline water electrolysis. *Electrochim. Acta*, **82**, 384–391.

139. Marini, S., Salvi, P., Nelli, P., Pesenti, R., Villa, M., and Kiros, Y. (2013) Oxygen evolution in alkali with gas diffusion electrodes. *Int. J. Hydrogen Energy*, **38** (26), 11496–11506.

140. Koj, M., Qian, J., and Turek, T. (2019) Novel alkaline water electrolysis with nickel-iron gas diffusion electrode for oxygen evolution. *Int. J. Hydrogen Energy*, **44** (57), 29862–29875.

141. Lira Garcia Barros, R., Kelleners, M.H.G., van Bemmel, L., van der Leegte, T.V.N., van der Schaaf, J., and de Groot, M.T. (2024) Elucidating the increased ohmic resistances in zero-gap alkaline water electrolysis. *Electrochim. Acta*, **507** (February), 145161.

142. Karimi, V., Sharma, R., Morgen, P., and Andersen, S.M. (2023) Multiple Bubble Removal Strategies to Promote Oxygen Evolution Reaction: Mechanistic Understandings from Orientation, Rotation, and Sonication Perspectives. *ACS Appl. Mater. Interfaces*, **15** (42), 49233–49245.

143. Pollet, B.G., Foroughi, F., Faid, A.Y., Emberson, D.R., and Islam, M.H. (2020) Does power ultrasound (26 kHz) affect the hydrogen evolution reaction (HER) on Pt polycrystalline electrode in a mild acidic electrolyte? *Ultrason. Sonochem.*, **69** (June), 105238.

144. Hartig-Weiss, A., Tovini, M.F., Gasteiger, H.A., and El-Sayed, H.A. (2020) OER Catalyst Durability Tests Using the Rotating Disk Electrode Technique: The

Reason Why This Leads to Erroneous Conclusions. *ACS Appl. Energy Mater.*, **3** (11), 10323–10327.

145. Bleeker, J., van Kasteren, C., van Ommen, J.R., and Vermaas, D.A. (2024) Gas bubble removal from a zero-gap alkaline electrolyser with a pressure swing and why foam electrodes might not be suitable at high current densities. *Int. J. Hydrogen Energy*, **57** (January), 1398–1407.

146. Rocha, F., Delmelle, R., Georgiadis, C., and Proost, J. (2022) Effect of pore size and electrolyte flow rate on the bubble removal efficiency of 3D pure Ni foam electrodes during alkaline water electrolysis. *J. Environ. Chem. Eng.*, **10** (3), 107648.

147. Moreno-García, P., Kovács, N., Grozovski, V., Gálvez-Vázquez, M.D.J., Vesztergom, S., and Broekmann, P. (2020) Toward CO 2 Electroreduction under Controlled Mass Flow Conditions: A Combined Inverted RDE and Gas Chromatography Approach. *Anal. Chem.*, **92** (6), 4301–4308.

148. Cossar, E., Houache, M.S.E., Zhang, Z., and Baranova, E.A. (2020) Comparison of electrochemical active surface area methods for various nickel nanostructures. *J. Electroanal. Chem.*, **870**, 114246.

149. van der Heijden, O., Park, S., Eggebeen, J.J.J., and Koper, M.T.M. (2023) Non-Kinetic Effects Convolute Activity and Tafel Analysis for the Alkaline Oxygen Evolution Reaction on NiFeOOH Electrocatalysts. *Angew. Chemie Int. Ed.*, **62** (7), 1–9.

150. Yang, F., Kim, M.J., Brown, M., and Wiley, B.J. (2020) Alkaline Water Electrolysis at 25 A cm−2 with a Microfibrous Flow-through Electrode. *Adv. Energy Mater.*, **10** (25), 2001174.

151. Vincent, I., Choi, B., Nakoji, M., Ishizuka, M., Tsutsumi, K., and Tsutsumi, A. (2018) Pulsed current water splitting electrochemical cycle for hydrogen production. *Int. J. Hydrogen Energy*, **43** (22), 10240–10248.

152. Liu, T., Wang, J., Yang, X., and Gong, M. (2021) A review of pulse electrolysis for efficient energy conversion and chemical production. *J. Energy Chem.*, **59**, 69–82.

153. Cheng, H., Xia, Y., Hu, Z., and Wei, W. (2024) Optimum pulse electrolysis for efficiency enhancement of hydrogen production by alkaline water electrolyzers. *Appl. Energy*, **358** (January), 122510.

154. Monk, N., and Watson, S. (2016) Review of pulsed power for efficient hydrogen production. *Int. J. Hydrogen Energy*, **41** (19), 7782–7791.

155. Peng, Y., Choi, J.-Y., Bai, K., Zhang, Y., and Banham, D. (2021) Pulsed vs.

galvanostatic accelerated stress test protocols: Comparing predictions for anode reversal tolerance in proton exchange membrane fuel cells. *J. Power Sources*, **500** (May), 229986.

156. Alinejad, S., Inaba, M., Schröder, J., Du, J., Quinson, J., Zana, A., and Arenz, M. (2020) Testing fuel cell catalysts under more realistic reaction conditions: accelerated stress tests in a gas diffusion electrode setup. *J. Phys. Energy*, **2** (2), 024003.

157. Oelßner, W., Berthold, F., and Guth, U. (2006) The iR drop - Well-known but often underestimated in electrochemical polarization measurements and corrosion testing. *Mater. Corros.*, **57** (6), 455–466.

158. Voiry, D., Chhowalla, M., Gogotsi, Y., Kotov, N.A., Li, Y., Penner, R.M., Schaak, R.E., and Weiss, P.S. (2018) Best Practices for Reporting Electrocatalytic Performance of Nanomaterials. *ACS Nano*, **12** (10), 9635–9638.

159. Weininger, J.L., and Breiter, M.W. (1963) Effect of Crystal Structure on the Anodic Oxidation of Nickel. *J. Electrochem. Soc.*, **110** (6), 484.

160. Weininger, J.L., and Breiter, M.W. (1964) Hydrogen Evolution and Surface Oxidation of Nickel Electrodes in Alkaline Solution. *J. Electrochem. Soc.*, **111** (6), 707.

161. Bode, H., Dehmelt, K., and Witte, J. (1966) Zur kenntnis der nickelhydroxidelektrode-I. Über das nickel (II)-hydroxidhydrat. *Electrochim. Acta*, **11** (8), 1079–1087.

162. Beden, B., FloneSr, D., Léger, J.M., and Lamy, C. (1985) A voltammetric study of the formation on hydroxides and oxyhydroxides on nickel single crystal electrodes in contact with an alkaline solution. *Surf. Sci.*, **162** (1–3), 822–829.

163. Corrigan, D.A. (1987) The Catalysis of the Oxygen Evolution Reaction by Iron Impurities in Thin Film Nickel Oxide Electrodes. *J. Electrochem. Soc.*, **134** (2), 377–384.

164. Trotochaud, L., Young, S.L., Ranney, J.K., and Boettcher, S.W. (2014) Nickel-Iron oxyhydroxide oxygen-evolution electrocatalysts: The role of intentional and incidental iron incorporation. *J. Am. Chem. Soc.*, **136** (18), 6744–6753.

165. Spanos, I., Tesch, M.F., Yu, M., Tüysüz, H., Zhang, J., Feng, X., Müllen, K., Schlögl, R., and Mechler, A.K. (2019) Facile Protocol for Alkaline Electrolyte Purification and Its Influence on a Ni–Co Oxide Catalyst for the Oxygen Evolution Reaction. *ACS Catal.*, **9** (9), 8165–8170.

166. Márquez, R.A., Kawashima, K., Son, Y.J., Castelino, G., Miller, N., Smith, L.A., Chukwuneke, C.E., and Mullins, C.B. (2023) Getting the Basics Right: Preparing

Alkaline Electrolytes for Electrochemical Applications. *ACS Energy Lett.*, 1141–1146.

167. Wei, C., Sun, S., Mandler, D., Wang, X., Qiao, S.Z., and Xu, Z.J. (2019) Approaches for measuring the surface areas of metal oxide electrocatalysts for determining their intrinsic electrocatalytic activity. *Chem. Soc. Rev.*, **48** (9), 2518–2534.

168. Pérez-Alonso, F.J., Adán, C., Rojas, S., Peña, M.A., and Fierro, J.L.G. (2014) Ni/Fe electrodes prepared by electrodeposition method over different substrates for oxygen evolution reaction in alkaline medium. *Int. J. Hydrogen Energy*, **39** (10), 5204–5212.

169. Anantharaj, S., Noda, S., Driess, M., and Menezes, P.W. (2021) The Pitfalls of Using Potentiodynamic Polarization Curves for Tafel Analysis in Electrocatalytic Water Splitting. *ACS Energy Lett.*, **6** (4), 1607–1611.

170. Akbashev, A.R. (2022) Electrocatalysis Goes Nuts. *ACS Catal.*, **12** (8), 4296–4301.

171. Fosang, A.J., and Colbran, R.J. (2015) Transparency Is the Key to Quality. *J. Biol. Chem.*, **290** (50), 29692–29694.

5. Manuscript I

This peer-reviewed publication describes a pure Ni foam benchmark for the dry anode setup in alkaline OER. Under quasi steady-state conditions, 2 A cm^{-2} utilizing pulsed galvanostatic electrolysis necessitated a potential of 2.00 V$_{RHE}$ during a 1-hour stability assessment.

Etienne Berner, Gustav K. H. Wiberg, Matthias Arenz

Attaining substantially enhanced oxygen evolution reaction rates on Ni foam catalysts in a gas diffusion electrode setup

RESEARCH ARTICLE

ADVANCED
ENERGY & SUSTAINABILITY
RESEARCH
Open Access

www.advenergysustres.com

Attaining Substantially Enhanced Oxygen Evolution Reaction Rates on Ni Foam Catalysts in a Gas Diffusion Electrode Setup

Etienne Berner, Gustav Karl Henrik Wiberg, and Matthias Arenz*

Water electrolysis plays a central role in the transition to a fossil-free society, but there are significant challenges to overcome in order to increase its availability on a large scale. Alkaline water electrolysis is a mature and scalable technology, although it has several disadvantages compared to electrolyzers working in acidic environments. In particular, the use of highly alkaline aqueous electrolytes can lead to corrosion, and the achieved current densities are relatively low. This study addresses the latter limitation by introducing a gas diffusion electrode (GDE) setup as a novel development tool that bridges the gap between research and practical applications in commercial devices such as fuel cells and electrolyzers. A high surface area Ni foam catalyst that can sustain exceptional oxygen evolution reaction (OER) current densities of up to $4\,A\,cm^{-2}$ in a quasi-steady-state within our GDE setup operating in an alkaline environment is presented. The high performance of this Ni-based benchmark catalyst is attributed to its deposition onto a mesh-like porous transport layer (PTL) via hydrogen-templated electrodeposition. This forms a porous foam-like structure that augments the mass transport of the gaseous reactants at the GDE.

1. Introduction

Interest in green hydrogen production has sparked numerous discussions regarding current and future developments that could pave the way for large-scale electrolysis in the gigawatt (GW) and terawatt (TW) ranges. There is a growing focus on exploring alternative energy landscapes aimed at establishing a hydrogen-based economy at individual, continental, and global levels. These efforts are driven by the imperative to decarbonize production and transportation sectors.[1–8]

Electrolysis in acidic environments within proton exchange membrane water electrolyzers (PEMWEs) relies heavily on catalysts such as IrO_2 and RuO_2, which are known for their exceptional performance.[9,10] However, there is growing concern regarding the availability of iridium, given that optimistic estimates suggest that 400–800 tons of iridium are required to produce hydrogen at a scale of 1 TW. Considering that the global annual mining output of iridium is approximately 8 tons year^{-1} (t a^{-1}),[11] achieving the necessary quantities for 1 TW production appears quite challenging. Alternatively, alkaline electrolysis utilizes abundant catalysts, such as nickel and iron, both of which are mined annually in the range of millions of tons (Ni: approx. $2.5\,Mt\,a^{-1}$, Fe: approx. $1800\,Mt\,a^{-1}$).[12,13] This ensures a substantial supply of catalytic material. However, there are limitations, such as lower current densities and slower system responses, when compared to state-of-the-art PEMWE technology. Enhancements in these aspects are required to make alkaline electrolysis competitive, which includes a theoretical comprehension of the surface reactions and technical improvements, for instance, regarding the electrode separator.[14–16] Despite various options for operational optimization, prevailing assumptions hinge on achieving anodic current densities exceeding $2\,A\,cm^{-2}$ for alkaline and anion exchange membrane (AEM) water electrolyzers (AEMWE), similar to present operational current densities of PEMWEs.[17] This target represents a manifold increase over the conventional standard current of approximately $0.2–0.5\,A\,cm^{-2}$ for alkaline systems.[18] A critical consideration for both acidic and alkaline systems pertains to the robustness and reliability of the catalysts, particularly when subjected to operational stress factors such as temperature variations, varying and high current loads, and cyclic on-off switches. In particular, a fast and flexible response to surplus renewable electricity is a relevant criterion for running an electrolyzer economically profitable in the future, because a significant portion of the cost per kilogram of H_2 is closely tied to the cost per kilowatt-hour (kWh) of electricity.

Gas diffusion electrodes (GDEs) are an established class of devices for electrochemical production and research. For example, they serve for the electrosynthesis of chloride gas in chloralkali electrolysis[19] and H_2O_2,[20] as the air cathode of a zinc-air battery,[21] to reduce CO_2,[22] in fuel cells,[23–25] and possibly for electrolyzers. These electrodes enable chemical reactions

E. Berner, G. K. H. Wiberg, M. Arenz
Department of Chemistry, Biochemistry and Pharmaceutical Sciences
University of Bern
Freiestrasse 3, CH-3012 Bern, Switzerland
E-mail: matthias.arenz@unibe.ch

The ORCID identification number(s) for the author(s) of this article can be found under https://doi.org/10.1002/aesr.202400050.

ADVANCED
SCIENCE NEWS
www.advancedsciencenews.com

ADVANCED
ENERGY & SUSTAINABILITY
**RESEARCH**
Open Access
www.advenergysustres.com

at large interfaces of the three-phase boundary and facilitate the transport of gaseous reactants. Therefore, GDEs serve as a critical bridge between gas-phase reactants and the underlying electrochemical processes, influencing mass transport, charge transfer, and overall device efficiency. Consistently, GDEs promote electrochemical reactions involving gaseous species at elevated current densities compared to electrodes implemented in pure liquid environments. GDEs typically consist of a porous conductive material as the electrode backbone, decorated with catalytic components to promote the desired chemical reaction.

Here, we report an in-house developed and modified three-electrode GDE setup to promote OER under alkaline conditions. The GDE setup is used to test the response of a high surface area Ni-foam type catalyst to varying and high current densities. The Ni-foams are directly electroplated onto a Ti-mesh that serves as porous transport layer (PTL), thus forming a catalyst coated substrate. The synthesis of metallic coatings and nanostructures via electroplating is a widely used fabrication method. This process operates in a defined environment, in which an electrical field drives the reduction of metal ions from the plating bath onto an electrically conductive substrate. The particular method applied here for producing the porous high-surface-area Ni foams, is the hydrogen bubble templated electrodeposition.[26] This approach holds significant potential across various fields, including catalysis,[27,28] energy storage,[29] and sensing.[30] It allows for the precise deposition of porous metals and was initially explored using metals such as Ni[31] and Cu.[32] Over time, it has garnered interest for a broader range of metals, including Ag,[33] as well as noble metals such as Au, Pt, and Pd.[34] Furthermore, the incorporation of bimetallic films and post-deposition operations has expanded the repertoire of novel materials achievable through this technique. We present a straightforward method for the fabrication of a catalytic coating in the form of a pure Ni foam without organic compounds on a conductive mesh-like Ti PTL that can sustain varying and high OER current densities.

2. Results and Discussion

2.1. Physical Characterization and Film Growth

The hydrogen bubble templated electrodeposition method has been reported for different metals, such as Ni[27] and Au.[30] In general, the process induces a morphology gradient in the porous metal film, with pore sizes increasing along with the coating thickness. To characterize the structure of the porous Ni foam, we explored a series of ascending deposition times and analyzed the Ni catalysts by scanning electron microscopy (SEM). This analysis highlights the distinct morphological changes in the Ni catalysts based on different deposition times, emphasizing the significance of hydrogen bubble template-assisted film growth in tailoring pore size and thickness. In **Figure 1**, the porous structure of the Ni foam on the PTL substrate is clearly identifiable, as are the geometrical dimensions of the substrate cavities (solid black in the upper row). This is required for an effective gaseous reactant transport in the gas flow field within the GDE. Cauliflower-like subunits were present at all deposition times, whereas the pore sizes of the outer surface layer varied depending on the growth time. Notably, the pore size diameters increased for thicker films, and for longer deposition times, a wider distribution was observed. The pore sizes of the film with the shortest deposition time (8 s) ranged from 3 to 5 μm, whereas the pore size distribution of the film deposited for 45 s ranged from 6 to 18 μm. These results indicate that, in thicker films, a gradient in pore size from smaller to larger pores develops within the film. Furthermore, we investigated the growth rate by determining the film thickness as a function of deposition time. The cross-sectional SEM analysis (Figure S1, Supporting Information) revealed a growth rate in thickness of approximately 0.7 μm s^{-1}, with a nucleation time of approximately 5 s. However, the growth rate was not constant throughout the deposition period. After 8 s of deposition, a thin layer of approximately 3–5 μm is evident. Subsequently, at a deposition time of 15 s, the thickness increased to approximately 10 μm, whereas a film thickness of approximately 35 μm was
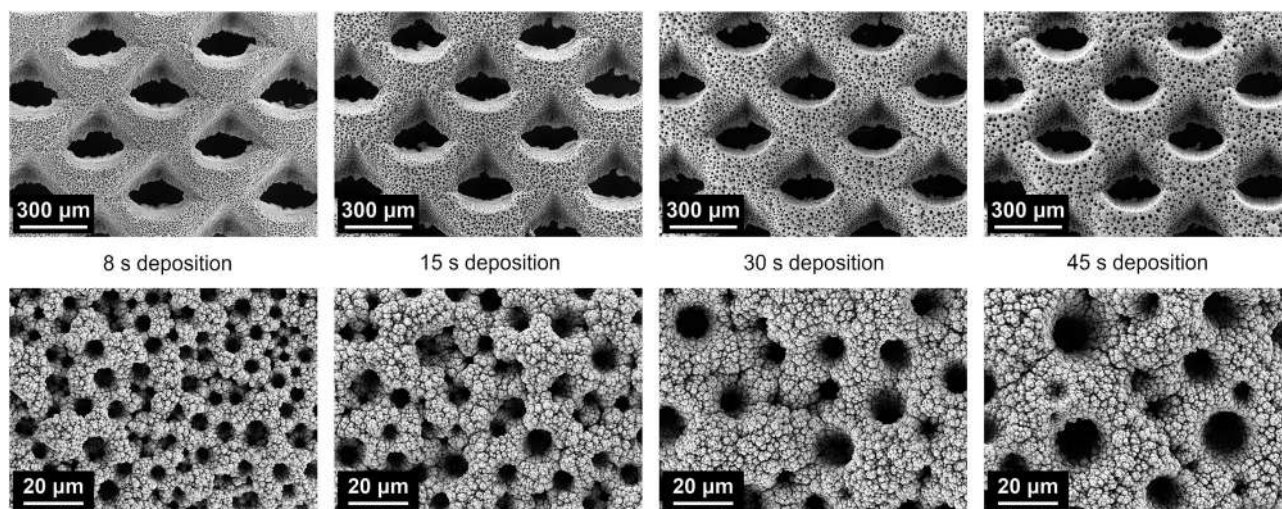
Figure 1. SE micrographs of Ni foams deposited on Ti-PTLs with varying deposition times. With prolonged growth, both the film thickness and the pore size diameter at the surface increase.

ADVANCED
SCIENCE NEWS

www.advancedsciencenews.com

ADVANCED
ENERGY & SUSTAINABILITY
RESEARCH
Open Access

www.advenergysustres.com

determined after 45 s of electrochemical deposition. Therefore, we conclude that the film thickness growth rate increases with an increase in pore size and prolonged deposition time. This phenomenon can be expected, considering that the deposition was performed at a fixed current density. Assuming a constant ratio between hydrogen evolution and metal deposition, that is, a constant Faradaic efficiency for metal deposition, an increase in the porosity also leads to an increase in the thickness growth rate. In this context, it should be mentioned that the film thickness was not completely homogeneous over the entire PTL substrate, which is attributed to its 3D geometrical texture.

The chemical compositions and structures of the PTL substrate and as-prepared Ni films were analyzed using energy-dispersive X-ray spectroscopy (SEM-EDS) (Figure S2, S3, Supporting Information) and X-ray diffraction (XRD) (Figure S4, Supporting Information). These measurements confirm the purity of the Ni films. In particular, the XRD measurements indicated a higher Ni to Ti ratio on the Ti substrate with longer deposition times. Interestingly, the XRD data did not reveal any visible Ni oxide formation after electrochemical activation of the films. This indicates that the oxide layer formed upon activation was too thin to be analyzed using XRD. Therefore, we propose the formation of a core–shell structure with a relatively thin NiO_x layer as the shell and metallic Ni as the core. The latter metal backbone provides "metallic" conductivity, which is essential when applying high current densities.

2.2. Electrochemical Surface Area Determination

Determination of the electrochemically active surface area (ECSA) is an important practice in electrocatalysis research.[35] When dealing with precious metals, comparing mass activity becomes crucial, as researchers focus on enhancing the effectiveness of applied materials. For Ni-based nanomaterials, electrochemical analysis of the surface area can involve various techniques, such as hydrogen or oxygen adsorption, underpotential deposition (UDP) of metals, determination of the double-layer capacitance by cyclic voltammetry (CV) or electrochemical impedance spectroscopy (EIS), and redox-couple currents based on specific molecules such as quinone-hydroquinone.[36–38] To determine the double-layer capacitance, it should be mentioned that the liquid electrolyte employed and its concentration may influence the obtained values and should be considered when presenting absolute values. In the case of Ni during alkaline OER, its surface exhibits various forms of hydroxides, such as $Ni(OH)_2$, and oxyhydroxides like NiOOH.[39] Particularly, the irreversible transformation of α-$Ni(OH)_2$ into β-$Ni(OH)_2$ above $0.5 V_{RHE}$,[40] rendering the determination of absolute values for the ECSA that considers active sites for the OER on Ni a challenging task.

Moderate oxidation of the Ni surface, for example via CV, can be described as follows

$$Ni + 2OH^- \rightleftarrows Ni(OH)_2 + 2e^- \qquad (1)$$

At potentials below $0.5 V_{RHE}$, a few monolayers of the hydroxide form, with the formation charge of α-$Ni(OH)_2$ reported as $364 \mu C cm^{-2}$ for the Ni(110) plane and $596 \mu C cm^{-2}$ for the Ni(111) plane. This irreversible formation was observed in the
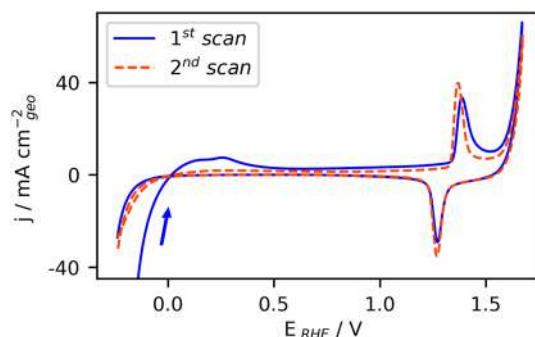
Figure 2. *iR*-corrected CVs acquired in the potential range spanning from the hydrogen evolution reaction to the OER of pristine Ni foam (45 s deposition) in 4 M KOH liquid electrolyte. As potentials exceed $0.5 V_{RHE}$, the irreversible formation of α-Ni (OH)$_2$ at ≈$0.3 V_{RHE}$ in the first CV is not present in the second scan. CVs initiated at $-0.25 V_{RHE}$ at a scan rate of $50 mV s^{-1}$ to $1.70 V_{RHE}$.

first and second CV curves of pristine Ni foam, as shown in **Figure 2**. The characteristic and reversible transformation of Ni(II) hydroxide to Ni(III) oxyhydroxide around $1.4 V_{RHE}$ is less sensitive to the surface structure due to the more amorphous nature of the surface oxides. The oxidation and reduction of $Ni(OH)_2$ can be described by the following equation:

$$Ni(OH)_2 + OH^- \rightleftarrows NiOOH + H_2O + e^- \qquad (2)$$
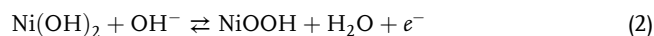
The reported interfacial double layer capacity of approximately $22 \mu F cm^{-2}$ see in ref. [41] for Ni is often used as a reference value and confirmed by different methods.[37] However, McCrory et al.[42] calculated with a general specific capacitance of $40 \mu F cm^{-2}$ in 1 M NaOH, whereas Zankowski et al.[43] measured $41 \mu F cm^{-2}$ using EIS in a 2 M KOH aqueous solution. Given this variety of values, we decided to measure a Ni foil in the electrolyte used in this study, which can be used as a benchmark. For the polished Ni foil, we measured a double-layer capacitance of $39 \mu F cm^{-2}$ when immersed in 4 M KOH, as depicted in the inset of **Figure 3**. This value is consistent with those reported by McCrory and Zankowski et al. The obvious variation in the reported values may be attributed to factors such as the polishing process creating a non-atomically flat surface, the pre-oxidation of Ni, or the specific parameters employed in our methodology. All ECSA values used a capacitance of $39 \mu F cm^{-2}$ as a normalization factor.

To determine the ECSA of the Ni foams as function of the deposition time, we investigated the capacitive current within the potential window of the non-Faradaic region, specifically between $0.55 V$ and $0.65 V_{RHE}$ (Figure S5, Supporting Information). Our procedure involved the pre-oxidation of Ni films immersed in a 4 M KOH liquid electrolyte, with variations in scan rates ranging from 25 to $1000 mV s^{-1}$. The analysis shown in Figure 3 reveals a nonlinear growth pattern in the ECSA relative to the electrodeposition time, with a declining rate of increase observed after 15 s of deposition time, as determined by examining the first derivative of the ECSA change. Our observations concerning the nucleation time during SEM studies conducted within the initial seconds of deposition align well with the
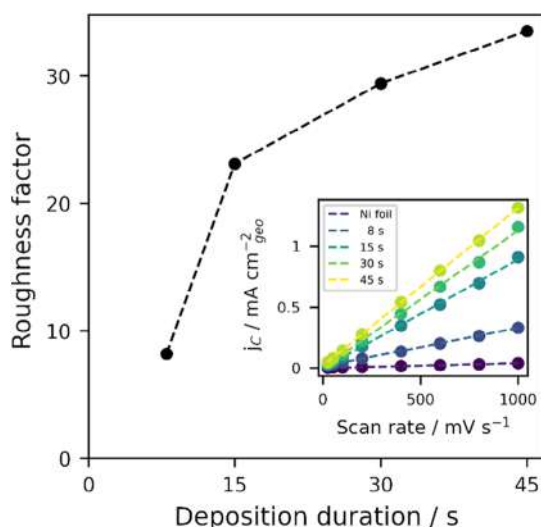
Figure 3. Surface area growth determined by capacitive currents in 4 M KOH electrolyte expressed by the roughness factor, representing the ECSA normalized to the geometrical area (cm^2_{ECSA}/cm^2_{geo}). The dashed line serves as a guide for the eye. Inset: Capacity determination of individual Ni foams at varying scan rates.

ECSA measurements. However, in contrast to the thickness, the ECSA growth rate decelerated after a deposition time of 15 s. This phenomenon may be attributed to the increased formation of larger hydrogen bubbles during the longer deposition periods. Consequently, the Ni foam became more porous with extended

deposition times. However, some underlying pores may become excessively deposited, rendering them inaccessible to the electrolyte. In summary, we conclude that for longer deposition times, the pore sizes increase and cause a faster growth rate of the film thickness. ECSA, specifically the surface-to-volume ratio, indicates the relationship between the available surface area and volume of the coating. After the initial growth on the seed layer, this ratio decreased. Thus, the growth rate of the available surface area differs from that of the layer thickness.

2.3. Electrochemical OER Performance

As discussed in the Introduction, achieving high current densities is one of the primary challenges in alkaline electrolysis. Furthermore, the ability to cope with varying loads is required. Hence, our testing focused on these topics, and we compared the potentiodynamic curves with the quasi-steady-state measurements obtained using pulsed potential assets. Furthermore, for each method, we compared the conventional approach using a standard electrochemical cell with the adapted GDE setup.

In **Figure 4**, we provide illustrative cyclic voltammograms and quasi-steady-state geometrical current density data for our Ni foam samples with varying deposition times on the Ti substrate. The left columns (a and c) display the CVs for both the liquid electrolyte and the GDE setup, whereas the right columns (b and d) show the corresponding quasi-steady-state measurements for these two setups. Notably, the substantial difference in current density magnitudes between the liquid electrolyte environment and the GDE setup is accentuated when comparing the two environments by rows, that is, a and b, and c and d. It is
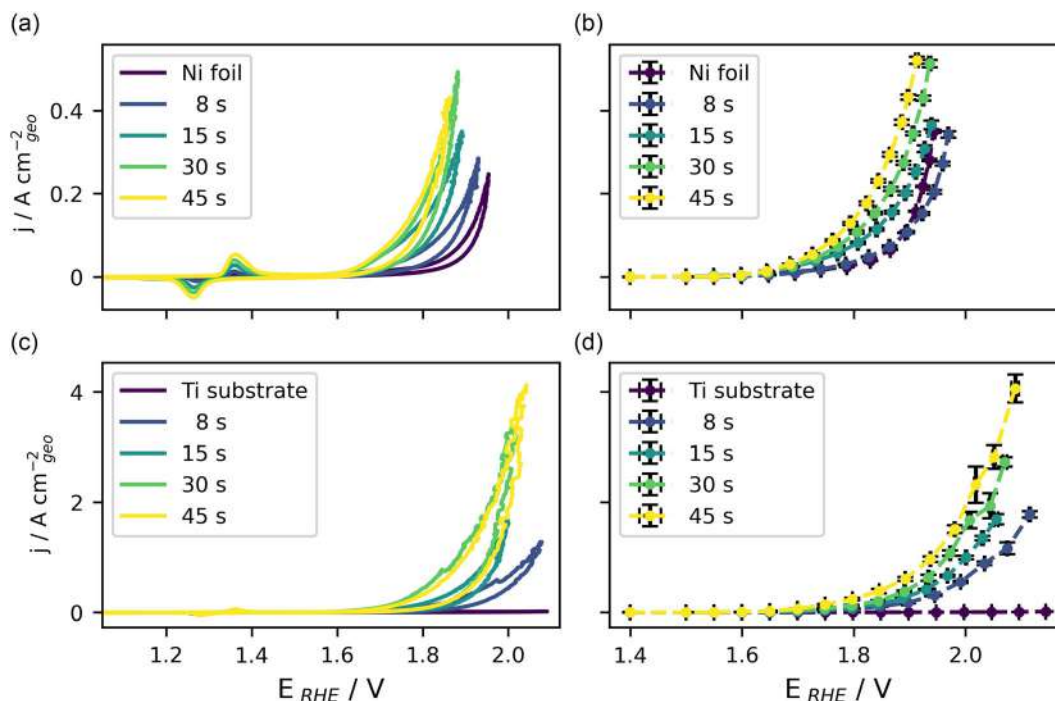
Figure 4. iR-corrected CVs and quasi-steady-state current densities for various deposition times of Ni foam in both the liquid electrolyte environment and GDE setup. CVs were recorded at an applied scan rate of 50 mV s^{-1}. a) Liquid environment, CVs; b) Liquid environment, quasi-steady-states; c) GDE setup, CVs; d) GDE setup, quasi-steady-states.

important to clarify that we are presenting not necessarily the best-performing, but the most representative sample from each measurement series. Each measurement was repeated a minimum of five times for each deposition time, and the values were derived from at least two independently synthesized coatings. The cyclic voltammograms correspond precisely to the same Ni foam samples presented under quasi-steady-state conditions.

By comparing the cyclic voltammograms with quasi-steady-state activities (Figure 4), it is evident that similar geometrical currents were achieved using the two measurement approaches in each separate environment. A discernible trend emerged, indicating that higher current activities were associated with longer deposition times, signifying the presence of larger surface areas. Employing our GDE setup, we can successfully demonstrate current densities under quasi-steady-state conditions of $4.06 \pm 0.25 \, A \, cm^{-2}$, corresponding to a potential of $2.09 \, V_{RHE}$ (see Figure 4d). Notably, this potential was iR-corrected by 60 mV (given the solution resistance of $199 \pm 27 \, m\Omega$) relative to the applied potential of $2.15 \, V_{RHE}$. In the dynamic CV, a current density of $4.12 \, A \, cm^{-2}$ was achieved at a potential of $2.04 \, V_{RHE}$. It is important to highlight that these exceptional current densities were achieved by the Ni foam with the highest ECSA, namely, that with the longest Ni deposition time of 45 s.

In contrast, in the liquid electrolyte environment, the current densities obtained using similar measurement protocols were substantially lower. Specifically, at an iR-corrected potential of $1.90 \, V_{RHE}$ (iR correction of 250 mV, given $R_{Sol.} \approx 2 \, \Omega$), we measured a current density of $0.432 \pm 0.006 \, A \, cm^{-2}$ under quasi-steady-state conditions for the foam with 45 s of Ni deposition. In the corresponding CV measurement, a current density of $0.431 \, mA \, cm^{-2}$ was observed at $1.86 \, V_{RHE}$. When compared to the current densities measured in our GDE setup under steady-state conditions at a potential of $1.90 \, V_{RHE}$, we recorded current densities of $0.610 \pm 0.037 \, A \, cm^{-2}$, as depicted in **Figure 5**. This performance surpasses that of the same Ni catalyst film in a liquid electrolyte environment by approximately 30% when considering a similar iR-corrected potential. However, it

should be noted that although the measurement protocols in the GDE and liquid environments were identical, the higher iR-correction of potentials in the liquid environment can lead to results that are more challenging to interpret. The reduction in resistivity between the reference and working electrodes played a significant role in the observed differences.

A recent study by Hodges et al.[44] involving a capillary-fed electrolysis cell demonstrated the importance of low resistivity for achieving highly efficient electrolysis and high current densities in alkaline environments. Similarly, Xu et al.[45] which explored the importance of catalyst conductivity and reported limitations for their "best" $NiFeO_xH_y$ oxyhydroxide OER catalyst in a liquid alkaline environment by its application in a membrane electrode assembly (MEA), particularly above current densities of $0.200 \, A \, cm^{-2}$ in an AEM setup. Consequently, it is imperative to measure current densities exceeding $0.2 \, A \, cm^{-2}$ to validate the stability of catalytic films. Furthermore, achieving current densities close to $1 \, A \, cm^{-2}$ in a liquid environment electrochemical cell is challenging, particularly at reasonable potentials.

Catalyst activity in conventional rotating disk electrode (RDE) measurements within a liquid electrolyte often relies on the potential at which $10 \, mA \, cm^{-2}$ is recorded. This value, although widely used, is somewhat arbitrary, considering that practical electrolyzers for hydrogen production typically operate at substantially higher current densities. In fact, current densities below $100 \, mA \, cm^{-2}$ are commonplace in liquid electrolyte measurements owing to mass transport limitations. To identify kinetic constraints, it is necessary to examine even lower current densities. In this context, it is notable that films with larger ECSAs achieve the $10 \, mA \, cm^{-2}$ benchmark at lower potentials than films with smaller ECSAs. However, it is essential to emphasize that the intrinsic activities of these catalysts remain consistent, as all coatings consist of pure Ni. The observed increase in activity arises from the availability of a greater number of active sites per unit geometric area, resulting in enhanced performance at the same potential. Interestingly, for steady-state measurements, the pure Ni foil in the liquid environment exhibited higher activity than the Ni foam deposited for 8 s. This disparity can be attributed to the more pronounced iR-correction effect associated with the Ni foil. However, when the iR correction was not considered, the performances of both materials were comparable. This discrepancy in behavior is not evident in dynamic CV measurements.

By normalizing the geometrical current densities to the ECSA, it is possible to assess the intrinsic activity of the Ni foams. Notably, we observed more consistent results in the measurements conducted within a liquid environment, wherein the ECSA-normalized current remains constant up to $1.8 \, V_{RHE}$ for all four deposition times. However, slight fluctuations were evident in the GDE setup. As illustrated in the inset of Figure 5, the ECSA-normalized currents closely align within the GDE setup in comparison with the liquid environment, particularly within the kinetic-limited region at $1.65 \, V_{RHE}$. This is justifiable, given the comparison of similar catalytic films. However, concerning the ECSA of the bare Ni foil, it is noteworthy that the electrodeposited Ni foams did not attain a similar level of activity across the range of the investigated potentials (Figure S6, Supporting Information). The bare Ni foil exhibits the highest intrinsic current density (j_{ECSA}). This observation suggests that the
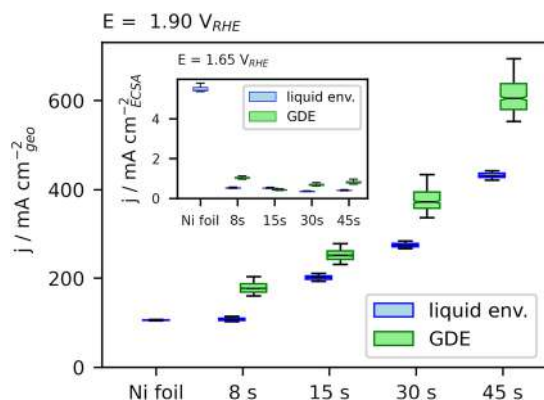

Figure 5. Box plots depicting current density measurements within the diffusion-limited region at $1.90 \, V_{RHE}$ under quasi-steady-state conditions reveal that the GDE setup exhibits approximately 30% greater activity than the catalytic foams in a liquid environment. Inset: In contrast, within the kinetic-limited region at $1.65 \, V_{RHE}$, the current densities normalized to the ECSA show analogous values between the GDE setup and the liquid electrolyte environment.

electrodeposited films may not fully unlock their catalytic potential, although it is worth considering that the measured ECSA may be relatively large. Examination of the morphology through SE micrographs indicates a relatively low calculated ECSA. At the potential of 1.98 V versus RHE, our foam with the highest ECSA achieved $j_{ECSA} = 45$ mA cm$^{-2}_{ESCA}$, a value comparable to the specific activities reported by Yang et al.[46] under the same potential. In summary, determining the true specific activity is challenging, and the geometrical current density may be more pertinent, especially given that Ni is an abundant metal and is typically not a critical factor in capital expenditure (CAPEX) considerations.

Through a comparative analysis of the overpotentials required to achieve a geometrical current density of 0.300 A cm^{-2}, the GDE setup demonstrated a modest yet notable advantage, ranging from 3% to 8%, compared with the liquid electrolyte environment across various deposition times (**Figure 6**). This reaffirms the parity of the activities observed in both environments (inset of Figure 5), particularly at a moderately standard current density, typical of classical alkaline electrolyzers. However, it is crucial to note that the overpotential required to achieve the same activity increases by approximately 100 mV when transitioning from the highest to the lowest ECSA. This underscores the paramount importance of having an adequate number of active sites per unit geometric area to achieve efficient electrolysis. Given the differences in synthesis time, which fall within the sub-minute range, and Ni material quantities, typically below 50 mg cm^{-2}, there is a strong rationale for the large-scale synthesis of films with higher ECSA.

The demonstrated activities under quasi-steady-state conditions can be further credited to the rapid and responsive protocol, which allows efficient bubble transport. Various studies have highlighted the critical role of bubble management in achieving high current densities. Iwata et al.[47] recently published a comprehensive study on bubble formation and release on Ni catalysts, particularly by applying a polytetrafluoroethylene (PTFE) coating onto the Ni surface. Examination of the film wettability in their work revealed the lowest overpotential, mainly attributed to ohmic losses due to bubble formation, when PTFE was absent on the Ni surfaces. This observation aligns with our coating approach, which did not involve organic additives. Notably, commercial Ni-plating baths often contain pH buffers and other additives that may potentially lead to catalyst inhibition. Last but not least, it should be mentioned that the exact reproducibility of
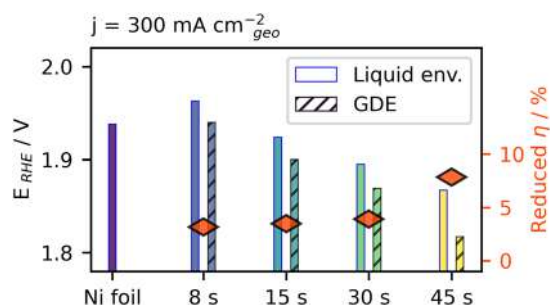
the presented measurements poses a significant challenge. A small active area of 7 mm^2 indicates that bubble formation has a substantial impact on the measured activity. Proper grid alignment of the Au-mesh on the Ni-coated Ti-PTL substrate is crucial for increasing the success rate of measurements, especially during high current densities in the GDE setup. Ideally, these components should be aligned at the same angle on top of each other, as and shown in Figure S9, Supporting Information. It is worth noting that the gas flow field was not optimized in this study. Nevertheless, we were able to improve the success rate of the measured protocols from 10% to >66%. In addition, stability remains a challenging aspect, particularly when the duration of the OER measurements is extended. This is due to the risk of internal resistivity caused by local bubble formation and the accompanying sensitivity owing to the small catalytic area. We performed galvanostatic pulsed stability tests at 2 A cm$^{-2}_{geo}$ for 1 h at elevated currents on four disks of the same 45 s electrodeposited Ni foam and measured an average potential of 2.004 V$_{RHE}$. In **Figure 7**, we show a representative sequence of the pulsed electrochemical protocol after one operational hour. We highlight the sensitive potential response to solution resistivity, which is directly influenced by bubble formation (Figure S7, Supporting Information). Applying a prolonged deposition time, the ECSA is expected to be larger and the necessary potential to reach 2 A cm^{-2} therefore anticipated to be below 2 V$_{RHE}$.
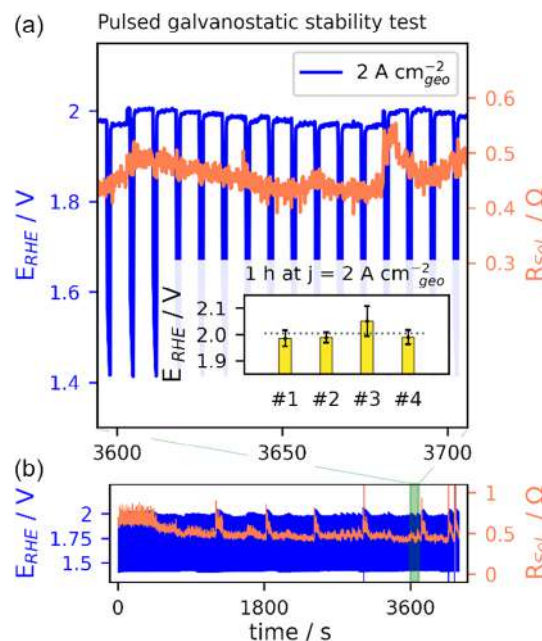
Figure 7. iR-corrected potentials at a pulsed current density of 2 A cm^{-2}. Four disks of a 45 s Ni foam deposition were measured during 600 pulses (each pulse for 6 s at 2 A cm^{-2}, then 1 s zero current). In a), we show a representative sequence of 100 s during the stability test after 1 h of operation. In the inset, the averaged potentials to perform for four different disks 1 h at 2 A cm^{-2} are shown. The average potential of 2.004 V$_{RHE}$ is indicated by the dashed line. In b), the entire potential course of the 600 pulses and the measured $R_{Sol.}$ are displayed of the particular disk. When the solution resistance exceeded 2 Ω, $R_{Sol.}$ can recover to the initial values after the selective application of short ultrasonic pulses in the liquid electrolyte compartment.

Figure 6. Intrapolated iR-corrected potentials at a current density of 300 mA cm^{-2} for quasi-steady-state conditions. The diamonds represent the moderate relative overpotential benefits in the GDE, reaching a maximum value of 8% for the 45 s electrodeposited Ni foam.

Multiple factors can lead to degradation of the system coupled with bubble-induced insulation, which causes local heating and hotspots. Membrane degradation poses a significant risk to system stability.[48,49] Hence, membrane development and gas flow fields require particular investigation. Furthermore, the components in the GDE setup were not specifically pressed, which may have affected their ability to ensure a longer endurance.

3. Conclusions

The demonstrated current densities of up to $4\,A\,cm^{-2}$ emphasize the potential for the additional development of AEMWEs. High OER reaction rates were achieved at room temperature under ambient conditions, using a GDE as the anodic OER electrode. This approach offers improved mass transport of the evolved oxygen gas compared with the liquid electrolyte environment and enables higher current densities. Another advantage of this setup is the driving force of the hydroxides through the membrane toward the positively charged anode. Furthermore, the ohmic resistance was reduced to enable a more effective water-splitting process at elevated currents. Galvanostatic stability tests at the high geometric current density of $2\,A\,cm^{-2}$ revealed no catalyst degradation. The introduction of quasi-steady-state behavior through electrochemical responses within subseconds and pulsed galvanostatic stability testing marks significant steps toward enhancing the reaction rates for grid-tied electricity integration. This paves the way for coupling electrolyzers with intermittently generated electricity from renewable resources, such as wind and photovoltaics. Fast-responsive, potentially mass-scalable AEMWEs can expedite the decarbonization of hydrogen production and contribute to mitigating greenhouse gas emissions. However, regarding stability, further research is required to improve the system setup operation. Given the choice of pure Ni as a catalyst, more catalytically active materials, such as NiFe and NiFeCo, are expected to outperform the presented results, and we work toward more active and efficient catalytic coatings to drive this progress.

4. Experimental Section

Chemicals, Materials and Gases: For the electrolyte solution, the plating bath and for rinsing the laboratory equipment ultrapure water (resistivity $\geq 18.2\,M\Omega\,cm$, total organic carbon [TOC] $\leq 5\,ppb$) from a Milli-Q system (Merck, IQ 7000) was employed. The electrolyte was prepared using potassium hydroxide pellets (KOH, Ph. Eur. grade; Hänseler, Switzerland) max. 15 wt% H_2O and Fe content below 3 ppm without further purification. Nickel sulphate hexahydrate (NiSO$_4$·6 H$_2$O, ACS reagent, $\geq 98\%$, Sigma-Aldrich) and ammonium chloride (NH$_4$Cl, ACS reagent, $\geq 99.5\%$, Sigma-Aldrich) were used as-received. Organic cleaning solvents were used as received, acetone (pure, Grogg Chemie, Switzerland), isopropanol (pure, Grogg Chemie, Switzerland), and ethanol (94%, Grogg Chemie, Switzerland).

Electrochemical Synthesis of Porous Ni Foam and Experimental Setup: Catalyst Synthesis via Electroplating: The catalyst samples were prepared by electrodeposition of Ni from a plating bath onto a titanium PTL substrate (MeliDiff TL 05/04-008 from MeliCon, Germany, with a thickness of 0.1 mm).[48] Electrodeposition was conducted using a computer-controlled power supply (Voltcraft, model CPPS-160-42). Prior to immersion in the plating bath, the PTLs were thoroughly cleaned. This cleaning

procedure involved subjecting the PTLs to an ultrasonic bath (US cleaner from VWR, model USC1200THD) for 5 min, twice each in soap water, acetone, isopropanol, and ethanol, and finally rinsing three times in ultrapure water using ultrasonic cleaning for 5 min each time. The plating bath composition consisted of 0.2 M NiSO$_4$ and 1.5 M NH$_4$Cl, with a pH measured at approximately 4 (pH-meter from Mettler-Toledo, model FEP20), and a conductivity of about $150\,mS\,cm^{-1}$ (conductivity meter from Greisinger, model GMH 3431). A pure Ni sheet (0.125 mm thickness, 99.9%, Sigma-Aldrich) was used as the sacrificial anode. To ensure reproducible coating conditions, the PTL and Ni sheet were fixed in specific sample holders and kept 30 mm apart in a custom-made cage. Galvano-controlled deposition was conducted at a geometrical area current density of $3\,A\,cm^{-2}$ for all the samples. At this current density, the applied potential between the electrodes exceeded 10 V, resulting in the majority of the charges being assigned to the reduction of hydrogen and only a fraction to the Ni deposition. The intentional formation of hydrogen bubbles was sought to achieve a porous, foam-like structure in the resulting catalytic coating.

Different deposition times, ranging from 8 to 45 s, were used to investigate the thicknesses and morphologies of the catalytic layer. The samples intended for measurements in the liquid electrolyte were deposited on a $1 \times 1\,cm^2$ square mask facing the Ni sheet anode and secured using polyimide film tape ("Kapton", 3M 5413, USA) on the backside of the Ti substrate to prevent coating. For the GDE measurements, Ni coatings were deposited on the Ti substrates with circular masks measuring 3 mm in diameter, with four or nine samples per run on the same PTL substrate. The backsides of the substrates were shielded with polyimide film tape (3M 5413, USA) to ensure that only the forefront was coated. To guarantee electrical contact in the GDE setup, 3 mm catalytic disks were die-cut using a 5 mm diameter circular blanking sleeve (Bohrbuechsen Heimberg AG, Switzerland) inserted into a custom-made precision tool before being assembled into the GDE setup (Figure S8, Supporting Information).

Gas Diffusion Electrode Assembly: The electrochemical activities under alkaline conditions were measured using a modified version of our GDE setup, which was initially developed to study the oxygen reduction reaction.[50–53] The technical illustration is shown in **Figure 8**. The main differences between the setups were the exchange of a carbon microporous layer (MPL) coated with platinum nanoparticles by the Ni-coated PTL substrate serving as the working electrode (WE) and the substitution of the PEM with an AEM. Coated PTLs with a diameter of 5 mm and a catalytic coating diameter of 3 mm were placed between an AEM (Sustainion X37-50 RT, Dioxide Materials, USA) and an Au mesh (woven from 0.102 mm ø wires, 99.99%, Thermo Scientific). The mesh acted as a current collector. To ensure proper sealing between the membrane and the liquid compartment, and homogeneous pressure distribution, a PTFE mask (inner ø = 7 mm, outer ø = 18 mm, 250 µm thickness) was used around the coated PTL disk (Figure S9, Supporting Information). Oxygen gas was introduced into the setup at a flow rate of $0.4\,L\,min^{-1}$ through a bubbler filled with ultrapure water to maintain a moist environment at the membrane interface. For the counter electrode (CE), a Pt wire was placed in a liquid 4 M KOH electrolyte (20 mL) in the upper part of the cell. During the measurements, the electrolyte was constantly agitated with a PTFE micro-surface stirrer shaft (Bola, Switzerland) to improve KOH accessibility and eliminate crossover bubbles.

Electrical contact with the working electrode was achieved through two Au plated pogo pins (Conrad Electronic, 1025-M-1.5N-AU-1.5) inserted into the hole channels, reaching the stainless-steel contacting screws. A reversible hydrogen electrode (RHE) in trapped hydrogen configuration was employed as the reference electrode (RE). It was placed in a Luggin capillary directly in contact with the membrane. To avoid contamination interference (from metal ions), all cell components in contact with the WE were made from polymers. Specifically, the upper cell body was constructed from polyether ether ketone (PEEK) and the lower cell body was made of polychlorotrifluoroethylene (PCTFE). Under optimal assembly conditions, the solution resistivity of the reference electrode was maintained below $1\,\Omega$, which translates to $200–500\,m\Omega$. The assembly is shown in Figure S10, Supporting Information.

Electrochemical Cell with Liquid Electrolyte: For comparison, both the coated PTLs and a bare Ni sheet were tested in an aqueous 4 M KOH

**ADVANCED
SCIENCE NEWS**

www.advancedsciencenews.com

**ADVANCED
ENERGY & SUSTAINABILITY
RESEARCH**
Open Access

www.advenergysustres.com
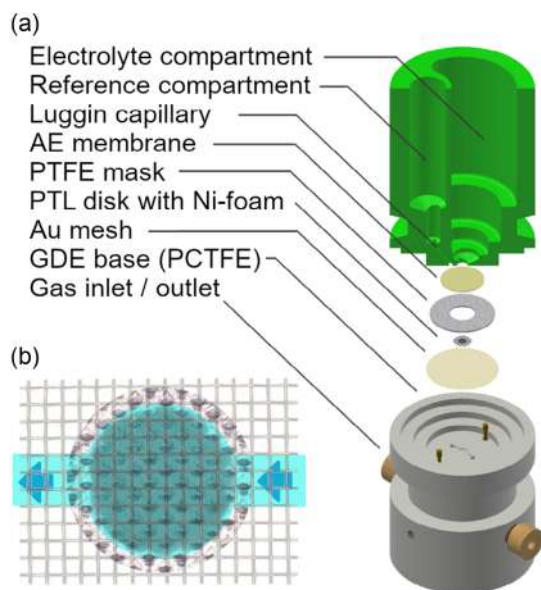
Figure 8. In a), the GDE setup is depicted, where the gold mesh acts as a current collector for the PTL to serve as WE via gold pins. The PTL makes direct contact with the membrane, separating the liquid electrolyte compartment from the GDE. A reference electrode senses the membrane via a Luggin capillary, minimizing solution resistance. In b), the gas flow field is illustrated in blue. An optical micrograph showing a catalytic disk substrate (Figure S8, Supporting Information) is on top of the current collecting mesh. The flow field was extruded from the GDE base body, running beneath the entire catalytic disk ($\varnothing = 3$ mm).

electrolyte (30 mL) using a standard electrochemical H-type glass cell without a membrane separating the electrodes.

The Ni sheet was subjected to a polishing process to reduce the roughness. It was first polished with sandpaper with a grain size of 2000, followed by a treatment with corundum slurry containing 300 and 50 nm particles (Buehler, Switzerland) for a few minutes each. Subsequently, it was thoroughly rinsed and cleaned twice in ultrapure water using ultrasonic baths for 5 min to achieve a mirror-like finish. The uncoated backsides of the PTLs and Ni foil were covered with Kapton tape to ensure a consistent active surface area for comparison with GDE measurements. Rectangular samples with typical geometrical areas of 20–30 mm^2 were used for the measurements, and the exact area of each sample was determined using a digital microscope for accurate area normalization. The samples were securely mounted on a PTFE sample holder and sealed with PTFE tape to ensure that only the desired catalytic surface was exposed to the electrolyte. A Pt wire was used as CE. The solution resistivity between RE and WE was measured to be approximately 2 Ω. The RHE was refreshed twice daily to maintain consistent conditions during characterization.

Characterization Methods: Physical Characterization: SEM micrographs were obtained using a Zeiss GeminiSEM 450 with SmartSEM 6.05 software. The scan parameters for the secondary electron (SE) Everhart-Thornley detector included a working distance (WD) of 3–3.5 mm, accelerating voltage of 2 kV, and probe current of 100 pA. For energy-dispersive X-ray spectroscopy (SEM-EDS), an Oxford Instruments photodetector Ultim max 150 controlled via AZTec software (5.0) was employed at a WD of 8–8.7 mm, acceleration voltage of 15 kV, and probe current of 500 pA. Optical micrographs were obtained using a Keyence VHX-6000 digital microscope. Pore size analysis of the SE micrographs was performed using ImageJ software.

XRD patterns were measured using a STOE StadiP in the reflection mode (Bragg−Brentano geometry). The apparatus was equipped with a

Cu Kα radiation source (40 keV, 40 mA, $\lambda = 0.1540$ nm) and operated using WinXPow software. X-ray diffractograms were recorded in steps of 0.1°/30 s with 2θ values ranging from 10° to 90° using a zero-matrix quartz sample holder.

Electrochemical Characterization: The measurements were performed using an ECi 210 potentiostat from the Nordic Electrochemistry ApS controlled via the EC4 DAQ 4.2.142 software. To investigate the OER performance, a similar approach was adopted for the GDE setup and standard electrochemical cell with a liquid electrolyte. Cyclic voltammograms were first recorded at scan rates of 100 (four cycles), 75 (three cycles), 50 (two cycles), and 25 (two cycles) mV s^{-1} in the range of 1.0–2.1 V$_{RHE}$. Subsequently, a dynamic potentiostatic protocol was applied to explore the quasi-steady-state conditions. This involved measuring the potentials at intervals of 1.40, 1.50, 1.55, 1.60, ... (with a step size of 50 mV) up to 2.15 V$_{RHE}$.

To simulate varying load and to avoid artefacts due to oxygen bubbles formed at the catalyst surface, the potential was reduced to 1.40 V$_{RHE}$ for one second after 6 s at the investigated potential. This procedure was repeated ten times per potential, resulting in a total measurement time of 60 s per investigated potential, with a total duration of 70 s (86% active OER time). The 700 measured currents (at a measurement frequency of 10 Hz) per potential were normalized to the geometric area and sorted in ascending order. Therefore, we refer to the current values presented as quasi-steady-state. They represent the mean of the data entries 150–600, with calculated standard deviations corresponding to 45 s of operation per potential at the steady state. The first 100 data entries corresponding to the inactive OER phase at 1.4 V$_{RHE}$ and were excluded. The highest last 100 current entries were not considered to eliminate capacitive currents from the measured OER activity.

In a separate study, CV was performed in 4 M KOH to determine the electrochemical surface area. Initially, the films were oxidized at 1.60 V$_{RHE}$ for 30 s. Cyclic voltammograms were recorded in the non-faradaic region between 0.55 and 0.65 V$_{RHE}$ at scan rates of 25, 50, 100, 200, 400, 600, 800, and 1000 mV s^{-1}. The measured currents were normalized to the geometric area and averaged between 0.595 and 0.605 V$_{RHE}$. The positive scan currents were added to the negative scan currents and then divided by two. These current densities, j_C, were used for linear regression for each deposition time to obtain their specific surface capacities in µF cm^{-2} at 1 V s^{-1}.

Galvanostatic stability tests at 2 A cm^{-2} included 600 pulses. Each pulse consisted of 6 s at 2 A cm^{-2}, followed by 1 s with no current. The total duration at 2 A cm^{-2} was 3600 s per measurement (total duration: 4200 s, 86% active OER time). To degas excessive bubbles, an ultrasonic horn homogenizer (Shanghai Ultrasonic Instrument Co., Model SC-150, 30 kHz, horn $\varnothing = 3$ mm) replaced the PTFE stirrer and was selectively applied to the electrolyte compartment when the resistance exceeded 2 Ω (solution resistance) or 16 Ω (cell resistance).

To track the solution resistance, a single-frequency EIS was performed during the entire experiment. An AC signal of 5 kHz and an amplitude of 5 mV was superposed to the control signal during the electrochemical measurements. The resulting impedance has a phase close to zero and is thus assumed to be related only to the solution resistance (due to the high frequency). Consequently, online monitoring of the solution resistance during the electrochemical measurements is possible. Then a posterior iR-correction for each recorded data point of the electrochemical data is done using the absolute impedance value.

Additionally Employed Software: The datasets of the potentiostat were evaluated with Jupyter Notebook 6.3.0, installed under Anaconda Navigator 2.0.3, and plotted with Matplotlib 3.7.4. During the preparation of this manuscript, the authors engaged with large language models (LLMs), specifically Paperpal and ChatGPT, to improve readability and grammatical quality. Subsequently, a comprehensive review and editing process were undertaken, assuming full responsibility for content accuracy. No references were derived from LLMs.

Supporting Information

Supporting Information is available from the Wiley Online Library or from the author.

[1] I. Staffell, D. Scamman, A. Velazquez Abad, P. Balcombe, P. E. Dodds, P. Ekins, N. Shah, K. R. Ward, *Energy Environ. Sci.* **2019**, *12*, 463.

[2] M. Nasser, T. F. Megahed, S. Ookawara, H. Hassan, *Environ. Sci. Pollut. Res.* **2022**, *29*, 86994.

[3] H. A. Miller, K. Bouzek, J. Hnat, S. Loos, C. I. Bernäcker, T. Weißgärber, L. Röntzsch, J. Meier-Haack, *Sustainable Energy Fuels* **2020**, *4*, 2114.

[4] G. Glenk, S. Reichelstein, *Nat. Energy* **2019**, *4*, 216.

[5] M. Kopp, D. Coleman, C. Stiller, K. Scheffer, J. Aichinger, B. Scheppat, *Int. J. Hydrogen Energy* **2017**, *42*, 13311.

[6] O. Schmidt, A. Gambhir, I. Staffell, A. Hawkes, J. Nelson, S. Few, *Int. J. Hydrogen Energy* **2017**, *42*, 30470.

[7] C. Van Pham, D. Escalera-López, K. Mayrhofer, S. Cherevko, S. Thiele, *Adv. Energy Mater.* **2021**, *11*, 2101998.

[8] J. Schneidewind, *Adv. Energy Mater.* **2022**, *12*, 2200342.

[9] P. Lettenmeier, J. Majchel, L. Wang, V. A. Saveleva, S. Zafeiratos, E. R. Savinova, J. J. Gallet, F. Bournel, A. S. Gago, K. A. Friedrich, *Chem. Sci.* **2018**, *9*, 3570.

[10] L. C. Seitz, C. F. Dickens, K. Nishio, Y. Hikita, J. Montoya, A. Doyle, C. Kirk, A. Vojvodic, H. Y. Hwang, J. K. Norskov, T. F. Jaramillo, *Science* **2016**, *353*, 1011.

[11] J. Kibsgaard, I. Chorkendorff, *Nat. Energy* **2019**, *4*, 430.

[12] S. Jasansky, M. Lieber, S. Giljum, V. Maus, *Sci. Data* **2023**, *10*, 52.

[13] C. Reichl, M. Schatz, *World Mining Data 2022, Vol. 37*, Austrian Federal Ministry of Agriculture, Regions and Tourism, Vienna **2022**.

[14] C. Hu, L. Zhang, J. Gong, *Energy Environ. Sci.* **2019**, *12*, 2620.

[15] M. R. Kraglund, M. Carmo, G. Schiller, S. A. Ansar, D. Aili, E. Christensen, J. O. Jensen, *Energy Environ. Sci.* **2019**, *12*, 3313.

[16] S. Anantharaj, V. Aravindan, *Adv. Energy Mater.* **2020**, *10*, 1902666.

[17] M. Chatenet, B. G. Pollet, D. R. Dekel, F. Dionigi, J. Deseure, P. Millet, R. D. Braatz, M. Z. Bazant, M. Eikerling, I. Staffell, P. Balcombe, Y. Shao-Horn, H. Schäfer, *Chem. Soc. Rev.* **2022**, *51*, 4583.

[18] A. Buttler, H. Spliethoff, *Renewable Sustainable Energy Rev.* **2018**, *82*, 2440.

[19] I. Moussallem, J. Jörissen, U. Kunz, S. Pinnow, T. Turek, *J. Appl. Electrochem.* **2008**, *38*, 1177.

[20] S. C. Perry, D. Pangotra, L. Vieira, L. I. Csepei, V. Sieber, L. Wang, C. Ponce de León, F. C. Walsh, *Nat. Rev. Chem.* **2019**, *3*, 442.

[21] J. Pan, Y. Y. Xu, H. Yang, Z. Dong, H. Liu, B. Y. Xia, *Adv. Sci.* **2018**, *5*, 1700691.

[22] F. Pan, Y. Yang, *Energy Environ. Sci.* **2020**, *13*, 2275.

[23] F. Xiao, Y. C. Wang, Z. P. Wu, G. Chen, F. Yang, S. Zhu, K. Siddharth, Z. Kong, A. Lu, J. C. Li, C. J. Zhong, Z. Y. Zhou, M. Shao, *Adv. Mater.* **2021**, *33*, 2006292.

[24] F. Bidault, D. J. L. Brett, P. H. Middleton, N. P. Brandon, *J. Power Sources* **2009**, *187*, 39.

[25] K. Ehelebe, N. Schmitt, G. Sievers, A. W. Jensen, A. Hrnjić, P. Collantes Jiménez, P. Kaiser, M. Geuß, Y.-P. Ku, P. Jovanovič, K. J. J. Mayrhofer, B. Etzold, N. Hodnik, M. Escudero-Escribano, M. Arenz, S. Cherevko, *ACS Energy Lett.* **2022**, *7*, 816.

[26] B. J. Plowman, L. A. Jones, S. K. Bhargava, *Chem. Commun.* **2015**, *51*, 4331.

[27] K. I. Siwek, S. Eugénio, D. M. F. Santos, M. T. Silva, M. F. Montemor, *Int. J. Hydrogen Energy* **2019**, *44*, 1701.

[28] S. Vesztergom, A. Dutta, M. Rahaman, K. Kiran, I. Zelocualtecatl Montiel, P. Broekmann, *ChemCatChem* **2021**, *13*, 1039.

[29] X. Zuo, K. Chang, J. Zhao, Z. Xie, H. Tang, B. Li, Z. Chang, *J. Mater. Chem. A* **2015**, *4*, 51.

[30] J. van der Zalm, S. Chen, W. Huang, A. Chen, *J. Electrochem. Soc.* **2020**, *167*, 037532.

[31] C. A. Marozzi, A. C. Chialvo, *Electrochim. Acta* **2000**, *45*, 2111.

[32] H. C. Shin, M. Liu, *Chem. Mater.* **2004**, *16*, 5460.

[33] S. Cherevko, C. H. Chung, *Electrochim. Acta* **2010**, *55*, 6383.

[34] R. Du, X. Jin, R. Hübner, X. Fan, Y. Hu, A. Eychmüller, *Adv. Energy Mater.* **2020**, *10*, 1901945.

[35] D. Voiry, M. Chhowalla, Y. Gogotsi, N. A. Kotov, Y. Li, R. M. Penner, R. E. Schaak, P. S. Weiss, *ACS Nano* **2018**, *12*, 9635.

[36] S. Trasatti, O. A. Petrii, *Pure Appl. Chem.* **1991**, *63*, 711.

[37] C. A. Marozzi, A. C. Chialvo, *Electrochim. Acta* **1996**, *41*, 2361.

[38] E. Cossar, M. S. E. Houache, Z. Zhang, E. A. Baranova, *J. Electroanal. Chem.* **2020**, *870*, 114246.

[39] H. Bode, K. Dehmelt, J. Witte, *Electrochim. Acta* **1966**, *11*, 1079.

[40] B. Beden, D. Floner, J. M. Léger, C. Lamy, *Surf. Sci.* **1985**, *162*, 822.

[41] J. L. Weininger, M. W. Breiter, *J. Electrochem. Soc.* **1964**, *111*, 707.

[42] C. C. L. McCrory, S. Jung, I. M. Ferrer, S. M. Chatman, J. C. Peters, T. F. Jaramillo, *J. Am. Chem. Soc.* **2015**, *137*, 4347.

[43] S. P. Zankowski, P. M. Vereecken, *J. Electrochem. Soc.* **2019**, *166*, D227.

[44] A. Hodges, A. L. Hoang, G. Tsekouras, K. Wagner, C. Y. Lee, G. F. Swiegers, G. G. Wallace, *Nat. Commun.* **2022**, *13*, 1304.

[45] D. Xu, M. B. Stevens, M. R. Cosby, S. Z. Oener, A. M. Smith, L. J. Enman, K. E. Ayers, C. B. Capuano, J. N. Renner, N. Danilovic, Y. Li, H. Wang, Q. Zhang, S. W. Boettcher, *ACS Catal.* **2019**, *9*, 7.

[46] F. Yang, M. J. Kim, M. Brown, B. J. Wiley, *Adv. Energy Mater.* **2020**, *10*, 2001174.

[47] R. Iwata, L. Zhang, K. L. Wilke, S. Gong, M. He, B. M. Gallant, E. N. Wang, *Joule* **2021**, *5*, 887.

[48] F. Razmjooei, T. Morawietz, E. Taghizadeh, E. Hadjixenophontos, L. Mues, M. Gerle, B. D. Wood, C. Harms, A. S. Gago, S. A. Ansar, K. A. Friedrich, *Joule* **2021**, *5*, 1776.

[49] C. Minnaar, F. De Beer, D. Bessarabov, *Energy Fuels* **2020**, *34*, 1014.

[50] G. K. H. Wiberg, M. Fleige, M. Arenz, *Rev. Sci. Instrum.* **2015**, *86*, 024102.

[51] M. Inaba, A. W. Jensen, G. W. Sievers, M. Escudero-Escribano, A. Zana, M. Arenz, *Energy Environ. Sci.* **2018**, *11*, 988.

[52] J. Schröder, V. A. Mints, A. Bornet, E. Berner, M. Fathi Tovini, J. Quinson, G. K. H. Wiberg, F. Bizzotto, H. A. El-Sayed, M. Arenz, *JACS Au* **2021**, *1*, 247.

[53] G. K. H. Wiberg, S. Nösberger, M. Arenz, *Curr. Opin. Electrochem.* **2022**, *36*, 101129.

2400050 (10 of 10)

Supporting Information

Attaining substantially enhanced oxygen evolution reaction rates on Ni foam catalysts in a gas diffusion electrode setup

Etienne Berner,[1] Gustav K. H. Wiberg,[1] Matthias Arenz[1]*

1: Department of Chemistry, Biochemistry and Pharmaceutical Sciences, University of Bern, Bern, Switzerland

* Corresponding Author: Prof. Dr. M. Arenz (matthias.arenz@unibe.ch)

SEM cross-section analysis
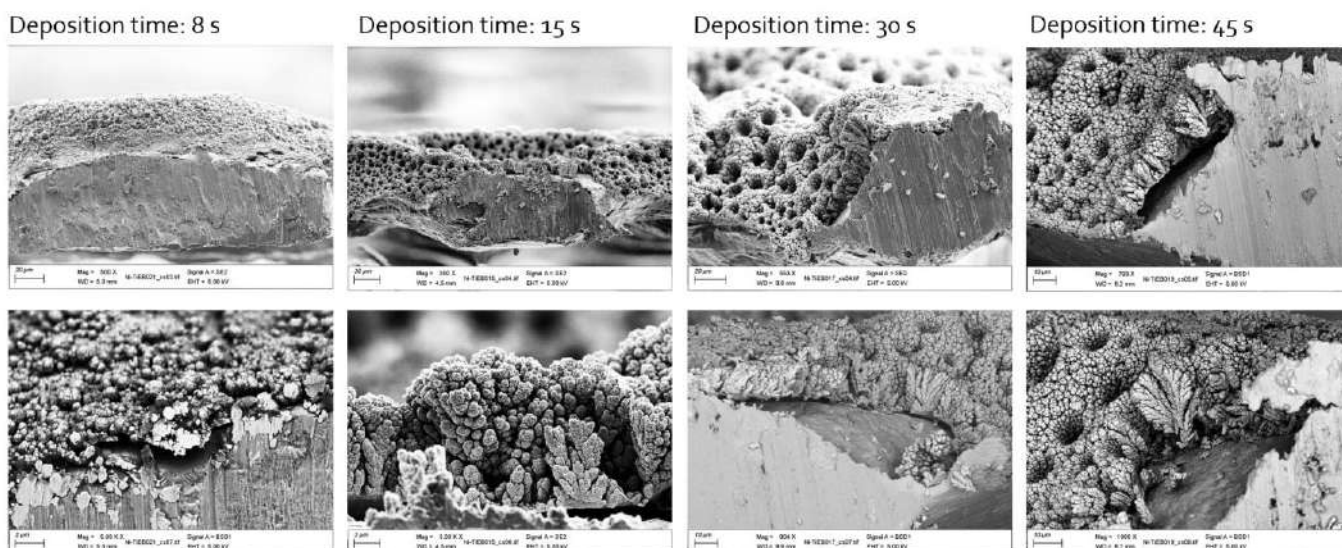
Figure S1. Exemplarily SEM cross sections of Ni foams deposited at various deposition times. The coated PTL substrates were cut using sheet metal shears.

SEM-EDS analysis
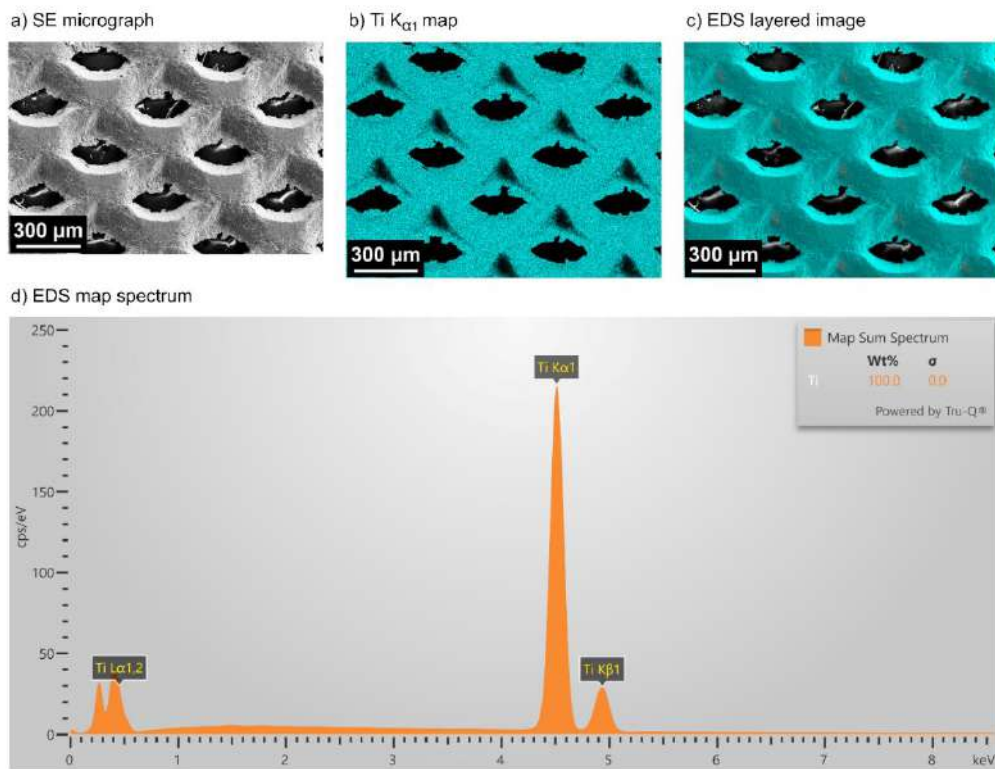
Figure S2. SEM-EDS analysis of the Ti PTL substrate. The purity of Ti was verified, along with the relatively even surface structure of the substrate. The peak left to Ti L_α in the spectrum shown in (e) at 0.28 keV originates from the carbon from the glue for sample fixation. The weak peak at 1.49 keV originated from the aluminum background (chamber and sample holder). Oxygen (0.53 keV) was detected but neglected in the automated element identification by the analysis software, although the slightly decelerated decrease in the Ti L_α peak indicated the presence of a small amount of oxygen.
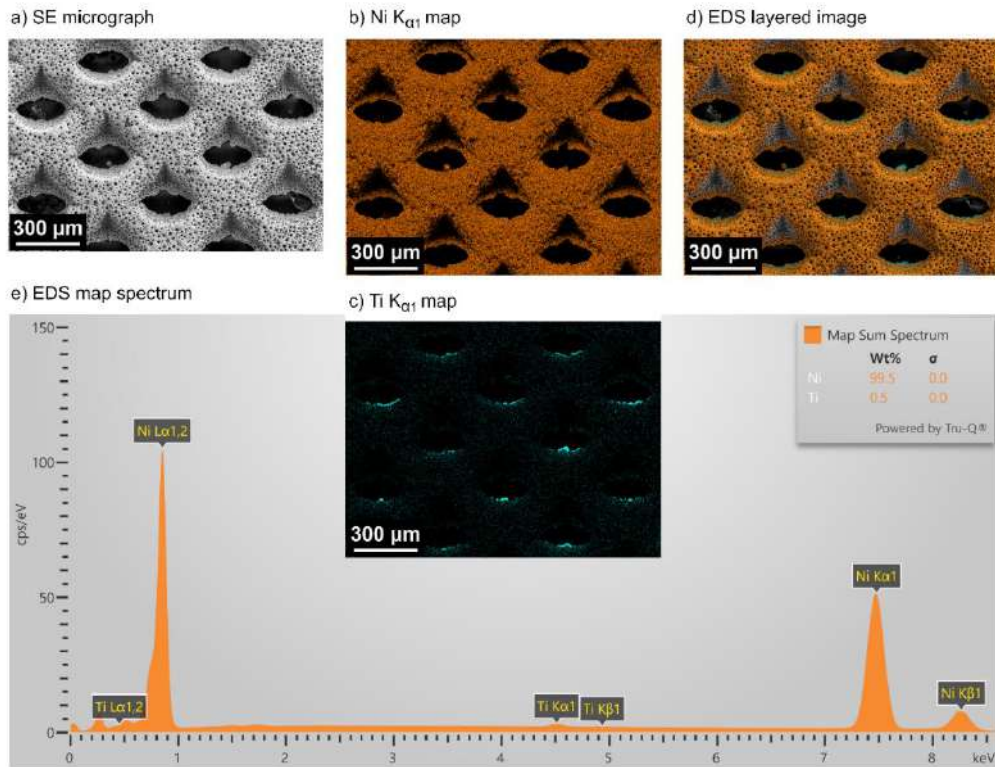
Figure S3. SEM-EDS analysis of a 45 s Ni foam. The purity of the Ni was verified over the entire substrate surface. The spectrum shown in (e) reveals characteristics similar to those reported in Figure S5 for carbon (0.28 keV), oxygen (0.53 keV), and aluminum (1.49 keV) peaks. The low, 0.5 wt.%, fraction of Ti is mostly originated by edge effects, where the shielding Kapton tape at the backside of the substrate hindered Ni deposition.

X-ray diffraction
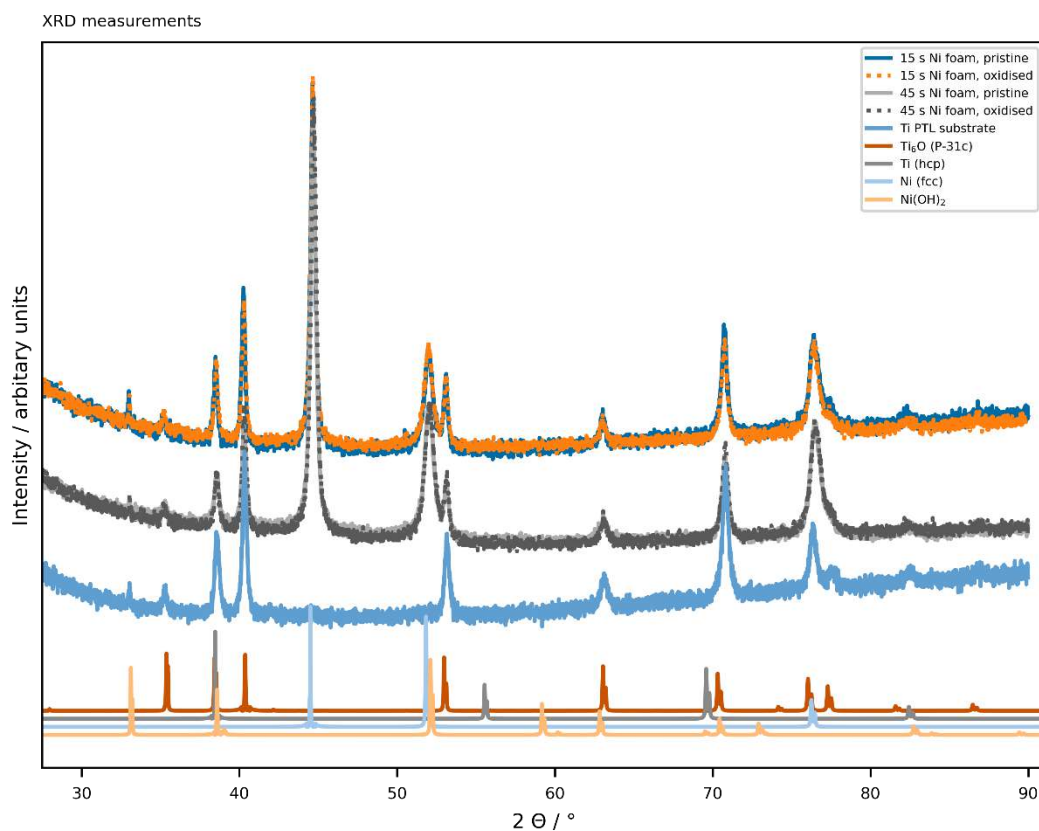
Figure S4. XRD measurements reveal no difference between the pristine and oxidized Ni foams. However, a longer deposition time leads to a smaller substrate signature, as expected. The Ni (fcc) signal at 44.4° was more pronounced for the thicker Ni foam, similar to the signal at 51.7°, whereas these peaks were absent on the PTL substrate. Interestingly regarding the substrate is, the Ti (hcp) signature is less pronounced than the Ti_6O signature. This is in agreement with the small fraction of oxygen detected by SEM-EDS and confirms the presence of a slightly oxidized Ti substrate. References for material-specific spectra are listed at the end of this document.

Capacity measurements

Cyclic Voltammograms
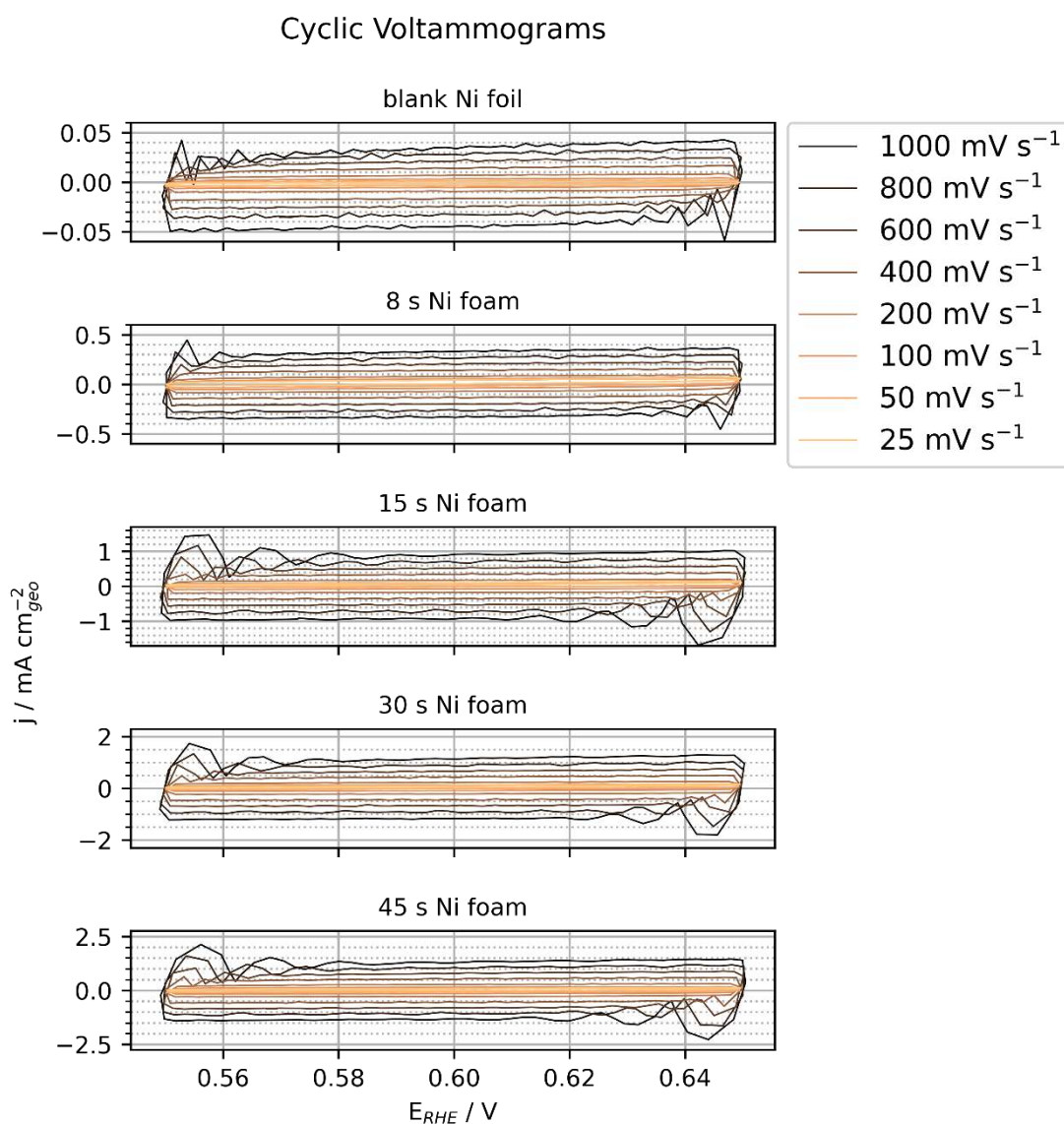
Figure S5. Raw data normalized to geometric area for the capacity measurements in the potential window from 0.55 - 0.65 V_{RHE} for the four deposition durations and a polished Ni foil in 4M KOH electrolyte. To determine the capacitive current j_C, the geometrical current densities were averaged between 0.595 and 0.605 V_{RHE} for each scan rate. The sum of the values of the positive and negative scan currents was divided by two to obtain j_C for the linear regression depicted in the inset of Figure 3.

ECSA normalized current density
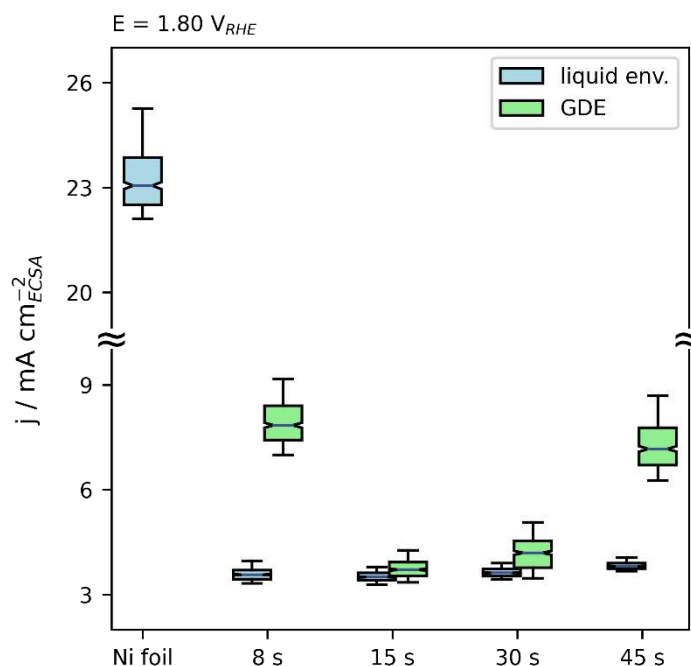
Figure S6. The ECSA normalized quasi-steady-state current density at 1.80 V_{RHE} presented in box plots reveals that the polished Ni foil is the most active "intrinsic" catalyst. In the liquid environment (4M KOH), the "intrinsic" currents are almost constant for all Ni deposition durations ($j_{ECSA} \approx 3.5$ mA cm$^{-2}_{ECSA}$). As the surface determination was performed in a 4M KOH electrolyte and the geometric areas within the liquid electrolyte were relatively large (~ 25 mm^2), this result indicates an appropriate approach for determining the ECSAs via capacitive currents in the non-Faradaic region for activities in a liquid environment. Because the ECSA current density is inversely proportional to the absolute values of the ECSA, higher j_{ECSA} current densities within the GDE could refer to smaller real ECSAs during the measurement, as assumed for the calculation. In the GDE setup, smaller geometric areas (7 mm^2) were experimentally exposed, resulting in higher error margins. The exact alignment of disks within the GDE setup is challenging, meaning that the disks are not perfectly centered. Therefore, less catalytic coating could have been exposed and the effective geometric area of the catalytic coating was lower. This explains the higher "intrinsic" activity of the films in the GDE compared to that in the liquid environment. Furthermore, the plotted iR-free potentials are not always exactly at 1.80 V_{RHE}, that is in particular for the liquid measurements 1.785 V < V_{RHE} < 1.808 V and for the GDE setup 1.794 V < V_{RHE} < 1.799 V.

Determining the iR correction for electrochemical potentials

In general, the goal is to obtain the potential of the electrochemical interface. However, due to the physical separation of the reference electrode and the working electrode, whenever there is a current, a potential offset of the size of i*R$_{Sol.}$ is also measured. To mitigate this offset, an iR free potential ($E_{iR-free}$) can be obtained by applying the following equation:

$$E_{iR-free} = E_{measured} - i * R_{Sol.}$$

In some cases, this calculation can be done by the electronic hardware of the potentiostat during the measurement, i.e. iR-compensation, or after the measurement, using a software in a computer, i.e. iR-correction.

In this study, we employ post measurement correction of the data. The electronic compensation can only work properly, if the solution resistance stays constant during the entirety of the experiment. During our experiments, the R$_{Sol.}$ was continuously measured, and we could observe that the resistance varied significantly. Therefore, the hardware correction could not be employed, thus we could only do post measurement correction.

Here follows how the $E_{iR-free}$ was calculated. At each time instant (t_i), the potentiostat measure E(t_i), i(t_i) and R$_{Sol.}$(t_i). Thus at each instant we can calculate $E_{iR-free}(t_i)$. More explicitly, we used the following equation:

$$E_{iR-free}(t_i) = E_{measured}(t_i) - i(t_i) * R_{Sol.}(t_i)$$

Stability measurements
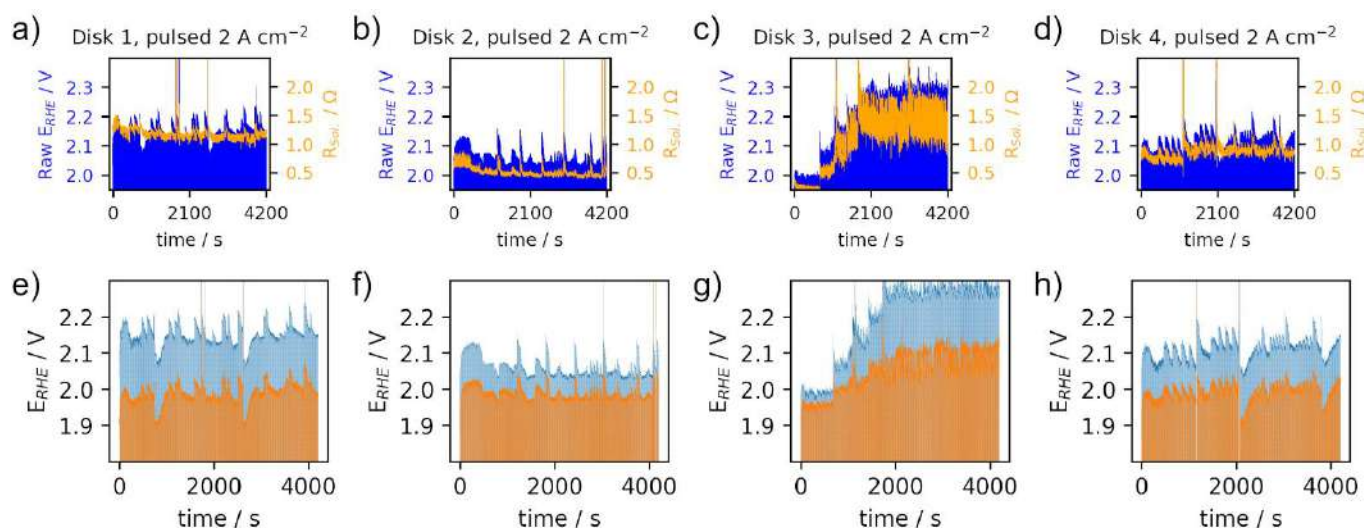
Figure S7. Stability measurements of four disks (45 s Ni deposition, fabricated in one synthesis) subjected to 600 pulses (each pulse was 6 s at 2 A cm$^{-2}_{geo}$, followed by 1 s of zero current). Upper line, (a) to (d): The non-corrected potential curves in blue and the measured solution resistances in orange are shown. The solution resistance was measured by a superposed, single-frequency EIS (AC signal of 5 kHz with an amplitude of 5 mV) throughout the entire experiment. The potential responses to $R_{Sol.}$ are apparently visible. Bubble formation can cause a dramatic and rapid increase in the solution resistance. For effective bubble removal, a horn sonicator under software control was selectively applied to the liquid electrolyte compartment above the GDE, if $R_{Sol.}$ exceeded 2 Ω. After the ultrasonic pulse, the resistance could recover to initial values. Lower line, (e) to (h): The blue potential curve is the corresponding raw data of the upper line. The orange potential curve represents the respective iR-free potentials calculated at instant of recorded data (see prev. section). For example, the applied current density was 2 A cm^{-2}, given the geometric surface area of 7.07 mm^2, the applied current was 141 mA. The potential drop for $R_{Sol.}$ at 1 Ω is then 141 mV. In (f), the potential drop is below 100 mV, as $R_{Sol.}$ is ~ 0.5 Ω. In (g), the potential drop was approximately 150 mV, given $R_{Sol.}$ was slightly higher than 1 Ω.

Electrodeposited catalytic Ni circles and geometrical characteristics of catalytic disks
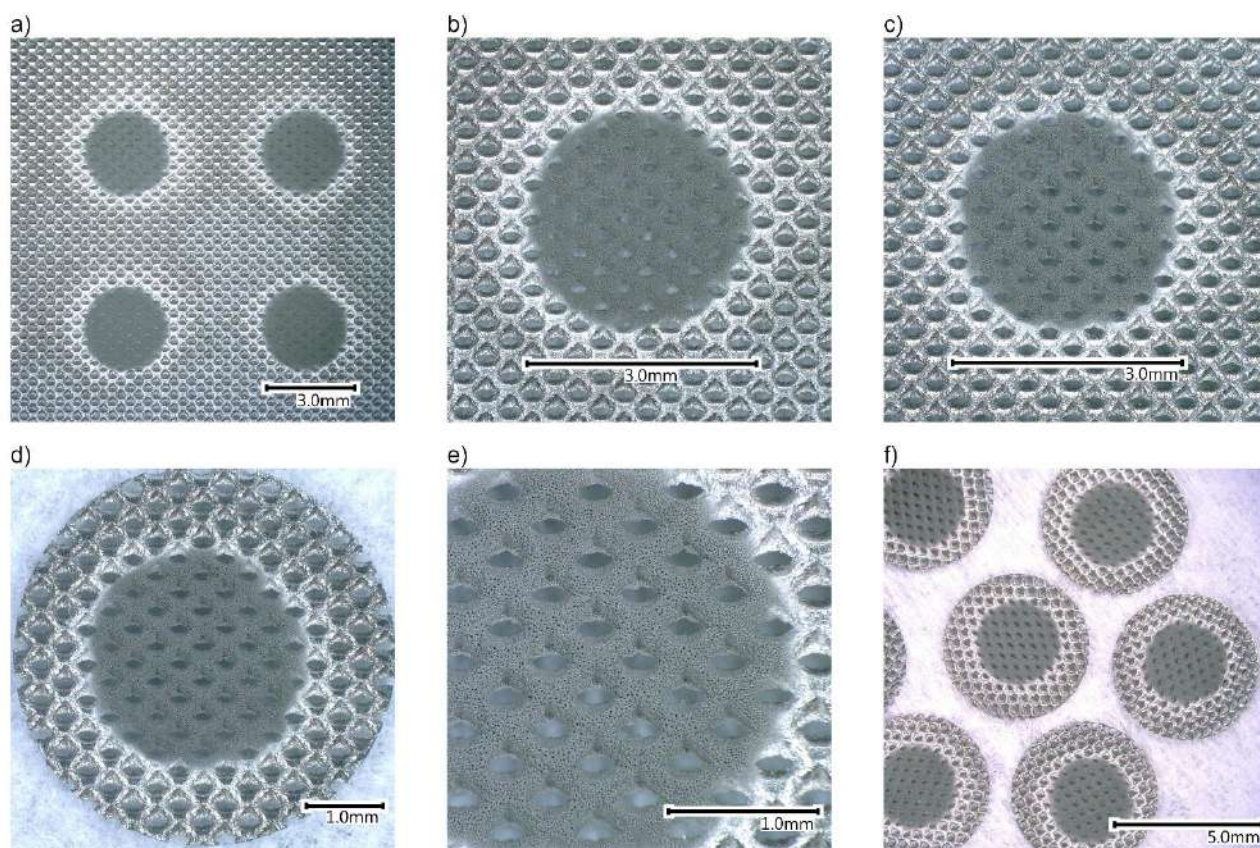
Figure S8. Optical micrographs of a 45 s Ni foam deposition with circular masks (Ø = 3 mm); (a) four neighboring Ni catalytic depositions; (b) and (c) exemplarily samples on the substrate to illustrate homogeneity and differences between two disks; (d) catalytic disk of the sample shown in c) to be inserted into the GDE setup; (e) enlarged magnification to show exemplarily film homogeneity over the disk and edge behavior; (f) several disks of the same deposition to illustrate typical center alignment.

Embedding the Ni coated catalytic disk into the gas diffusion electrode setup
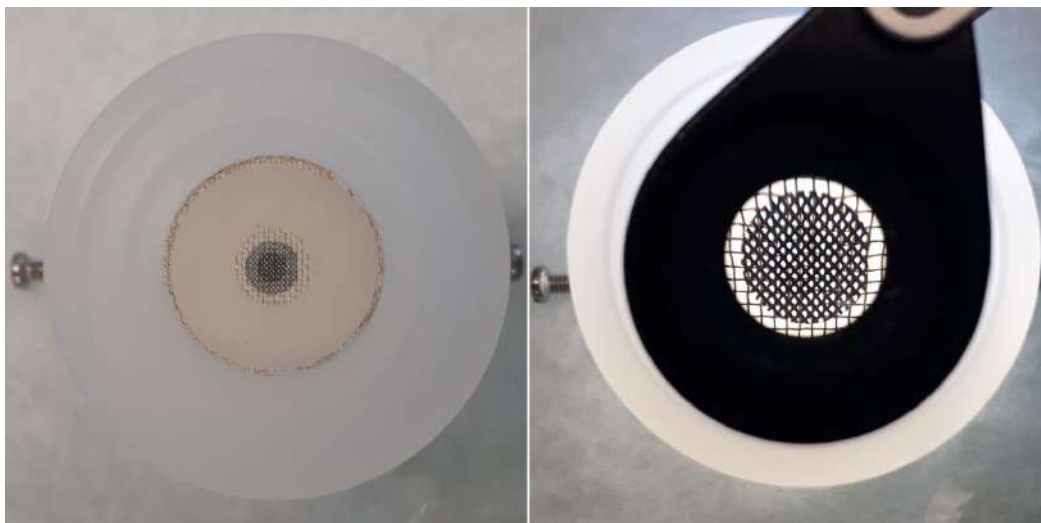
Figure S9. PTL disk positioned on top of the gas flow field covered by the Au contact mesh (Ø = 20 mm) before the final assembly. Left: Assembly including the Au mesh, PTFE mask (outer Ø = 18 mm, inner Ø = 7 mm), and Ti PTL disk (Ø = 5 mm, catalytic coating Ø = 3 mm). Right: The same assembly under a 20x magnifying glass (Eschenbach, Germany).

GDE assembly
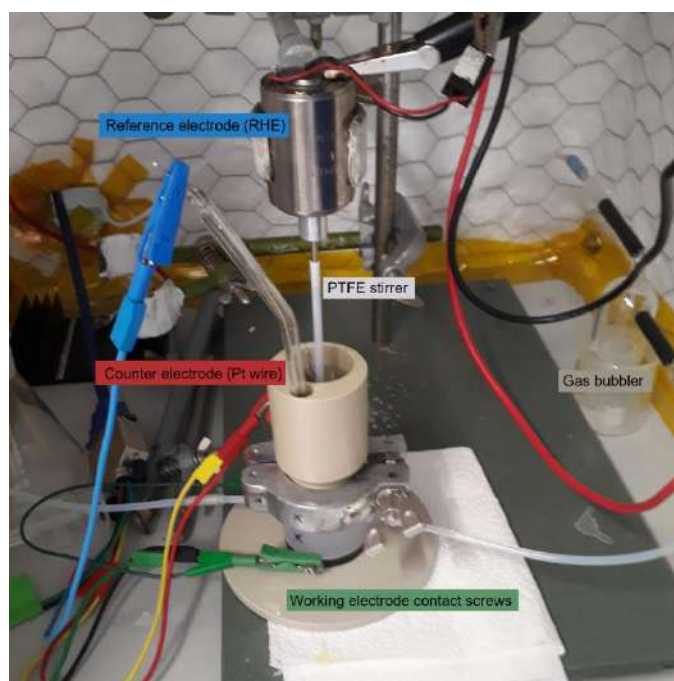
Figure S10. Illustrated GDE setup. The working electrode (i.e., the Ni foam catalytic disk) was embedded between the gas flow field at the bottom and the liquid electrolyte compartment using a membrane on top of the catalytic disk to ensure that the electrolyte (4M KOH) remained in the upper compartment. The electrolyte was agitated with a stirrer. The reference electrode was placed in a Lugging capillary that was in direct contact with the membrane to lower the solution resistivity.

References

The XRD reference data were obtained from the "Crystallography Open Database" (www.crystallography.net).

Ti_6O: COD entry # 1529015
Yamaguchi, S.; Koiwa, M.; Hirabayashi, M., Interstitial Superlattice of Ti_6O and its Transformation, *Journal of the Physical Society of Japan*, 1966, *21*, 2096-2096

Ti (hcp): COD entry # 9008554
Wyckoff, R. W. G., Second edition. Interscience Publishers, New York, *Crystal Structures*, 1963, *1*, 7-83

Ni (fcc): COD entry # 2102272
Angel, R. J.; Bismayer, U.; Marshall, W. G., Local and long-range order in ferroelastic lead phosphate at high pressure, *Acta Crystallographica Section B*, 2004, *60*, 1-9

$Ni(OH)_2$: COD entry # 9011314
Ramesh, T. N.; Kamath, P. V.; Shivakumara, C., Classification of stacking faults and their stepwise elemination during the disorder -> order transformation of nickel hydroxide, *Acta Crystallographica, Section B*, 2006, *62*, 530-536

6. Manuscript II

This work was published in ChemRxiv and is available as a preprint. It includes the development and application of more active FeNi foam catalysts employed in the dry anode configuration. The most competitive FeNi alloy required an averaged potential of 1.82 V_{RHE} at a pulsed current density of 3 A cm^{-2}.

Etienne Berner, Gustav K. H. Wiberg, Matthias Arenz

Investigation of FeNi alloy foams at high oxygen evolution reaction rates using a dry anode setup in alkaline environment

Investigation of FeNi alloy foams at high oxygen evolution reaction rates using a dry anode setup in alkaline environment

Etienne Berner [1], Gustav K. H. Wiberg [1], Matthias Arenz [1*]

1: Department of Chemistry, Biochemistry and Pharmaceutical Sciences, University of Bern, Bern, Switzerland

* Corresponding Author: Prof. Dr. M. Arenz (matthias.arenz@unibe.ch)

Abstract

We investigated the composition-activity relationship of porous FeNi alloy foams for the alkaline oxygen evolution reaction (OER). We compared conventional transient behavior using cyclic voltammetry with the performance at high geometric current densities up to 3.0 A cm^{-2} achieved at quasi steady-state conditions employing pulsed electrolysis. The experiments were performed under setup parameters, we introduce as dry anode conditions for anion exchange membrane (AEM) water electrolyzers. In this context, a dry anode refers to an electrode setup in which the catalyst is not directly submerged in a liquid medium, unlike conventional electrodes fed with an alkaline electrolyte. Instead, the anode is purged with humidified gas. Eleven different compositions in the FeNi alloy space (93 – 2 at. % Fe) were synthesized using the hydrogen bubble template method, resulting in porous foams with similar structures. A rigorous statistical analysis of all measured data was conducted to ensure reproducibility. The influence of bubble formation on the solution resistance is elucidated and, consequently, the apparent performance is assessed. The most efficient alloy composition required an averaged mean potential of 1.82 V$_{RHE}$ for 3 A cm^{-2} under quasi steady-state conditions.

1. Introduction

The growing imperative to transition from a fossil-fuel-based economy to a society powered by renewable energy has stimulated interest in alternative strategies to overcome the dependency on fossil-based resources.[1] Hydrogen plays a crucial role in this process, as it holds significant importance, particularly in the refining of fuels and in the production of fertilizers.[2] Today, approximately 95 % of hydrogen is produced from fossil sources due to economic reasons.[3] A potentially economically viable alternative for hydrogen production has recently garnered significant attention, namely anion exchange membrane (AEM) electrolysis.[4–6] This technology is of significant interest as it has the potential to combine the advantages of proton exchange membrane (PEM) electrolysis, such as efficiency, high current density, and rapid ramping, with the potential benefits

1

of alkaline electrolysis, including the utilization of non-precious metals as catalysts, stable operation, scalability and robustness. Its advancement is therefore of considerable importance.[7]

A limitation of current pressurized alkaline electrolyzers is their mass, and consequently, their relatively slow ramping time. Operational systems optimally function continuously without interruption. Therefore, a reduction in mass and, preferably, more compact systems are desirable to facilitate rapid ramping, considering the intermittent nature of renewable energy supply. Recently, the concept of a dry cathode was introduced to address the lower material consumption of AEM electrolyzers.[8–11] Using this configuration, current densities above 1 A cm^{-2}, requiring less than 2 V in MEA devices, were achieved. A potential advantage of this configuration is that the produced H_2 is water-free and requires less subsequent treatment than the conventionally produced H_2 in alkali vapor. Recent demonstrations of high current densities in AEM devices exceeding 5 A cm^{-2} have illustrated the capabilities of AEM technology in terms of enhanced stability and elevated production rates.[12,13]

This study introduces the dry anode concept for AEMs, wherein oxygen evolves at high rates at the gas diffusion electrode (GDE).[14–16] A conceivable advantage over dry cathodes is the electronic driving force for hydroxide transport through the AEM towards the positively charged anode. Furthermore, elevated reaction rates in water-splitting devices inherently result in gas bubble formation within liquid electrolytes, which induces undesirable internal resistance and consequently reduces device efficiency. Several bubble removal strategies have been proposed to address this challenge.[17,18] In addition to geometric configurations, ultrasonic pulses can facilitate bubble detachment from the catalytic surface. Moreover, electrochemical pulsing and electrolyte flow rate specifically applied to defined pore-size geometries within electrodes have demonstrated performance effects.[19,20]

In the presented work, we investigate a series of porous FeNi alloy foams for the alkaline OER. FeNi alloys are crucial for a diverse range of applications, including electrocatalysis and magnetic implementations.[21] The choice between FeNi or NiFe alloy abbreviations depends on the specific alloy composition, with common compositions including invar alloy[22] (65% Fe) and permalloy[23] (20% Fe). In general, FeNi alloys are considered among the most promising candidates for alkaline OER catalysis.[24–26] In this context, stainless steel has also been subjected to investigation.[27,28] As a consequence, the number of published studies on FeNi as an OER catalyst is substantial.[29] However, research encompassing the entire FeNi alloy space is more scarce,[30] as numerous studies focus on specific alloy compositions or slight deviations with functionalized components or specific crystal structures.[31] We employed a hydrogen bubble template method for the synthesis of FeNi alloys with varying composition. A comparable method has been demonstrated before.[32] Electroplating of FeNi alloys represents a common synthesis approach,[33] although the co-

electrodeposition of Fe and Ni is considered anomalous.[34] Reproducible electroplated FeNi films are widely applied in research and industrial applications.

2. Experimental

2.1. Chemicals, materials and gases

Ultrapure water from a Milli-Q system (Merck, IQ 7000) with a resistivity of 18.2 MΩ·cm and total organic carbon (TOC) not exceeding 5 ppb was used for the electrolyte solution, plating bath, gas bubbler, and equipment rinse. The electrolyte for the upper GDE compartment was prepared using potassium hydroxide pellets (KOH, Ph. Eur. grade; Hänseler, Switzerland) containing a maximum of 15 wt.% H_2O and less than 3 ppm Fe content, without additional purification. Sulfuric acid (H_2SO_4, 96 % pure, Grogg Chemie, Switzerland), iron sulfate heptahydrate ($FeSO_4 \cdot 7\ H_2O$, ACS reagent, ≥ 99 %, Merck), nickel sulfate hexahydrate ($NiSO_4 \cdot 6\ H_2O$, ACS reagent, ≥ 98 %, Sigma-Aldrich), and ammonium sulfate (($NH_4)_2SO_4$, ACS reagent, ≥ 99.5 %, Sigma-Aldrich) were used as received. Organic solvents for cleaning were employed without further processing, including acetone (pure, Grogg Chemie, Switzerland), isopropanol (pure, Grogg Chemie, Switzerland), and ethanol (94 %, Grogg Chemie, Switzerland). Argon (Ar 5.0, Carbagas, Switzerland) and oxygen gas (O_2 4.5, Carbagas, Switzerland) were used for all the experiments.

2.2. Electrochemical synthesis of porous FeNi foam and experimental setup

2.2.1. Electroplating for catalyst synthesis

FeNi catalyst samples were fabricated by electrodeposition onto a titanium PTL substrate (MeliDiff TL 05/04-008 from MeliCon, Germany, 0.1 mm thick expanded metal). The process used a computer-controlled power supply (Voltcraft, model CPPS-160-42). The PTLs were thoroughly cleaned before immersion into the plating bath. This involved two 5-minute ultrasonic bath cycles (US cleaner from VWR, model USC1200THD) in soap water, acetone, isopropanol, and ethanol, followed by three 5-minute ultrasonic rinses in ultrapure water. The plating baths comprised 0.2 M metal salt in relative ratios of Fe:Ni = 10:1, 5:1, 2:1, 1.5:1, 1:1, 1:1.5, 1:2, 1:5, 1:10, 1:20 and 1:100. All plating baths comprised 0.45 M ammonium sulfate as the electrolyte and were buffered in 0.1 M sulfuric acid. For each bath, 100 ml of 0.1 M H_2SO_4 was prepared and the pH was controlled to be close to 1 using a pH-meter (Mettler-Toledo, model FEP20). The solutions were then saturated with Ar and degassed in an ultrasonic bath to prevent the presence of oxygen. Then, iron sulfate was added and the bath was agitated until a clear solution was obtained (max. 10 minutes). Similarly, nickel sulfate was added. In the final step, ammonium sulfate was added, and the solution was agitated again until all salts were dissolved. The resulting pH of approximately 1.5, and conductivity of approximately 85 mS cm^{-1} (measured with a Greisinger conductivity meter, model GMH 3431)

were similar for all different Fe:Ni ratios (Table S1). A pure Pt foil (0.1 mm thick, 99.9 %, Goodfellow) served as the dimensionally stable anode. To ensure consistent coating conditions, the PTL and Pt foil were positioned 30 mm apart in a custom-made cage, using specific sample holders. Galvano-controlled deposition was performed at a normalized geometrical current density of 3.5 A cm^{-2} for 45 s for all the samples. This current density resulted in an applied potential exceeding 10 V between the electrodes, causing most of the charges to be allocated to hydrogen formation and only a fraction to FeNi co-deposition. The deliberate formation of hydrogen bubbles creates a porous, foam-like structure in the resulting catalytic coating. During the deposition, a magnetic stirrer at 500 rpm was used to agitate the plating bath, and argon gas was bubbled into the solution to reduce the amount of dissolved oxygen.

For samples intended for physical characterization and electrochemically active surface area (ECSA) measurements, the deposition was performed on a 1x1 cm^2 square mask facing the Pt foil anode, with the Ti substrate's backside secured using polyimide film tape ("Kapton", 3M 5413, USA) to prevent coating. For the OER activity measurements, FeNi coatings were applied to Ti substrates with circular masks measuring 3 mm in diameter, with nine samples per run on the same PTL substrate. The backsides of the substrate were protected with polyimide film tape (3M 5413, USA) to ensure coating only on the forefront. To guarantee electrical contact in the dry anode setup, 3 mm catalytic disks were die-cut using a 5 mm diameter circular blanking sleeve (Bohrbuechsen Heimberg AG, Switzerland) inserted into a custom-made precision tool.

2.2.2. "Dry anode" assembly

The electrochemical activities under alkaline conditions were measured using a previously described GDE setup,[16] which was initially developed to study the oxygen reduction reaction [35–37] and OER in acidic environment.[38] The FeNi-coated PTL substrates served as the working electrode (WE) and were positioned between an AEM (Sustainion X37-50 RT, Dioxide Materials, USA) and an Au mesh (woven from 0.102 mm $\varnothing$ wires, 99.99 %, Thermo Scientific), which served as a current collector. Two Au-plated pogo pins (Conrad Electronic, 1025-M-1.5N-AU-1.5) were inserted into the hole channels through the polymer lower cell body, made of polychlorotrifluoroethylene (PCTFE), which provided electrical contact between the Au mesh and stainless-steel screws to link the potentiostat. A polytetrafluoroethylene (PTFE) mask (inner $\varnothing$ = 7 mm, outer $\varnothing$ = 18 mm, 250 µm thickness) was placed around the coated PTL disk to ensure proper sealing of the gas flow field and uniform pressure distribution when the upper cell body, fabricated from polyetheretherketone (PEEK), was mounted and clamped to the lower cell compartment. The counter electrode (CE) consisted of a pure Pt wire immersed in 20 ml of 4 M KOH electrolyte in the upper section of the cell. A reversible hydrogen electrode (RHE) with a trapped hydrogen configuration in direct contact with the membrane via a Luggin capillary served as the reference electrode (RE). During the

measurements, humidified oxygen gas was passed through the anode (WE) at 50 mL min^{-1}. Humidification was achieved by using a bubbler containing ultrapure water. Optimal assembly conditions allowed the solution resistivity to be less than 1 Ω. An ultrasonic horn homogenizer (Shanghai Ultrasonic Instrument Co., Model SC-150, 30 kHz, horn Ø = 3 mm) was used to degas excessive bubbles during measurements at the RHE interface and in the liquid electrolyte.

2.2.3. ECSA measurement in liquid electrolyte

Experiments were performed using a conventional beaker cell containing approximately 100 ml of 4 M KOH solution. The uncoated backsides of the PTLs were covered with Kapton tape to measure the active surface area of the FeNi catalyst. The measurements were conducted on rectangular specimens with geometric areas ranging from 28 to 36 mm^2. A digital microscope (Keyence VHX-6000) was used to precisely determine the area of each sample for accurate area normalization. The specimens were firmly attached to a PTFE sample holder and sealed using PTFE tape to ensure that only the intended catalytic surface came into contact with the electrolyte. A platinum wire served as the counter electrode (CE). The solution resistivity between the reference electrode (RE) and working electrode (WE) was approximately 2 Ω.

2.3. Characterization methods

2.3.1. Physical characterizations

A Zeiss GeminiSEM 450 operated with SmartSEM 6.05 software was used to obtain SE micrographs. Images were recorded using a secondary electron (SE) Everhart-Thornley detector. For SEM-EDS analysis, an Oxford Instruments Ultim max 150 photodetector was employed, controlled by AZTec software (6.0), with parameters set of a working distance (WD) of 8.3 to 8.7 mm, 15 kV acceleration voltage, and 200 pA probe current. A Keyence VHX-6000 digital microscope was used to obtain optical micrographs. X-ray diffraction (XRD) patterns were recorded using a STOE StadiP device in reflection mode, utilizing Bragg-Brentano geometry. The instrument featured a Cu Kα radiation source (40 keV, 40 mA, λ = 0.1540 nm) and was operated via WinXPow software. Diffractograms were collected in 0.1° increments, measured for 30 s, spanning 2θ values from 10° to 90°, using a zero-matrix quartz sample holder.

2.3.2. Electrochemical characterization

An ECi 210 potentiostat from Nordic Electrochemistry ApS, controlled by the EC4 DAQ 4.2.142 software, was used to conduct the measurements. Initially, for each disk, cyclic voltammograms (CVs) were recorded at various scan rates and in different potential windows: 200 mV s^{-1} (two cycles) from -0.3 to 1.65 V$_{RHE}$, then 100 mV s^{-1} (four cycles), 75 mV s^{-1} (three cycles), 50 mV s^{-1} (two cycles), and 25 mV s^{-1} (one cycle), spanning the range between 1.0 to 1.9 V$_{RHE}$. Then followed one slow CV from 1.2 to 1.6 V$_{RHE}$ at 5 mV s^{-1} for the Tafel analysis and low current regime evaluation. Two potential scans spanning from -0.3 to 1.65 V$_{RHE}$ recorded with 200 mV s^{-1} completed the CV

measurements. Subsequently, a dynamic galvanostatic protocol was implemented to investigate the performance under quasi steady-state conditions. This protocol involved measuring geometrical current densities starting at 0.5 A cm^{-2}, with subsequent intervals of 0.5 A cm^{-2} step size up to 3 A cm^{-2}. In the applied protocol, the galvanostatic current density was hold for 6 seconds, followed by one second of zero current. This procedure was repeated 50 times per geometrical current density, resulting in a measurement time of 5 min of active OER per investigated current density and a total duration of 350 s (86 % active OER time) per current density step. The 3500 measured currents (at a measurement frequency of 10 Hz) were normalized to the geometric area, indexed, and sorted in ascending order. The measured potentials were indexed and iR-corrected before geometrical normalization and arranged according to the sorted current density. Therefore, we refer to the potential values presented as quasi steady-state.

To determine the ECSA, cyclic voltammetry (CV) was performed in 4 M KOH. Initially, the films were oxidized at 1.65 V$_{RHE}$ for 60 seconds. Cyclic voltammograms were recorded in the non-faradaic region between 0.55 - 0.65 V$_{RHE}$ at scan rates of 25, 50, 100, 200, 400, 600, 800, and 1000 mV s^{-1}. The measured currents were normalized to the geometric area and averaged between 0.595 and 0.605 V$_{RHE}$. Positive scan currents were added to the absolute value of the negative scan currents and then divided by two. These current densities in the double-layer region, J$_{dl}$, were used for a linear regression for each FeNi composition to obtain their specific surface capacities in mF cm^{-2}.

The galvanostatic stability test at 3 A cm^{-2} included similar pulse durations to those of the OER activity measurements. Each pulse consisted of 6 s at 3 A cm^{-2}, followed by 1 s with no current.

A high-frequency AC signal of 5 kHz and an amplitude of 10 mV was superimposed on all previously described electrochemical measurement protocols to measure the system resistances, as they enable tracking bubble formation and posterior iR-correction of the measured potentials to maintain comparable measurement conditions. The solution resistance is defined as the measured high-frequency resistance (HFR) between the WE and the end of the Luggin capillary (HFR$_{Sol.}$), sometimes referred to the uncompensated resistance, which primarily represents the membrane resistance in this setup. Cell resistance is defined similarly, but refers to the HFR between the WE and CE (HFR$_{Cell}$). As the solution and cell resistance was tracked in situ during the experiments, an ultrasonic horn could selectively be applied via software control when the resistance exceeded 2 Ω (HFR$_{Sol.}$) or 16 Ω (HFR$_{Cell}$), respectively, during electrochemical measurements to remove bubbles.

2.3.3 Additionally employed software

The potentiostat datasets were evaluated using Jupyter notebook (V. 6.3.0), installed under Anaconda Navigator (V. 2.0.3), and plotted with Matplotlib (V. 3.7.4). During the preparation of this manuscript, the authors engaged with large language models (LLMs), specifically Paperpal (V. 2.14.2) and ChatGPT (V. 3.5), to improve readability and grammatical quality. Subsequently, a

comprehensive review and editing process were undertaken, assuming full responsibility for content accuracy. No references were derived from LLMs. ImageJ (V. 1.53e) software facilitated pore size analysis of the SE micrographs.

3. Results and discussion

3.1. Catalyst and plating bath characterization

With the developed bath composition using sulfuric acid as the buffer and ammonium sulfate as the base electrolyte, we were able to synthesize and investigate a wide range of different FeNi alloy foam ratios by varying the initial ratio of iron to nickel sulfate in the plating bath (Figure S1). The composition of the FeNi alloy ranged from 93 atomic percent (at. %) to 2 at. % Fe content according to our SEM-EDS analysis (Table S2, Figure S2). We deposited each composition a minimum of two times on a 1x1 cm^2 area on a PTL substrate similar to that used for the OER measurements. Each sample was analyzed using three elemental maps at different locations: two at 75 x magnification and one at 250 x magnification. The signal intensity was above 20 cps eV^{-1} for the Kα peaks, which ensured reliable conclusions. Within each series of three maps, the variations within the individually synthesized Fe:Ni contents were below 2 at. %. The second electrodeposited sample series was synthesized a minimum of two months after the first application using the same plating baths and varied to some extent in composition, but not more than 4 at. % for the individual metal content. The plating baths appeared to be stable upon inspection, only minor precipitates in the form of transparent crystals were observed for higher amounts of Ni (> 90 at. %) in the plating baths after few days of storage. These were easily re-dissolved by heating the baths to approximately 50° C. Therefore, we conclude that the plating baths are stable and can be stored over an extended period; however, small deviations in the obtained Fe:Ni composition can occur over months. The search for impurities via SEM-EDS revealed no sulfur or other metal impurities in the coated catalytic foams.

The XRD analysis confirmed crystallinity of the alloy foams, although a certain amorphous structure can be assumed due to the fast synthesis via high overpotentials in the electrodeposition (Figure S3). For samples with a higher Fe content, the diffractograms aligned with pure Fe body-centered cubic (bcc) XRD signatures. The characteristic double peak of the "invar alloy" is visible for Fe:Ni ratios between 87:13 and 65:35 at. % at 2 θ ≈ 45°, where the transition from Fe bcc to Ni face-centered cubic (fcc) occurs. The most pronounced double peak was identified for samples containing approximately 70 at. % Fe, which also represents the most amorphous sample with lowest crystal sizes. This iron content represents a slightly larger fraction than that of the standard invar alloy, typically 65 at. %.[39] However, it is in good agreement with other reported data [40] and in the range of invar related properties.[22] Samples with increased Ni content diverge to the pure Ni

XRD signature, confirming the transition from Fe bcc crystal structure to Ni fcc structure depending on the alloying ratio contents. The reported FeNi alloy foams exhibited an fcc structure for Fe contents lower than 60 at. %.

Visual analysis of the SE micrographs revealed no significant differences between the foam compositions, as shown in Figure 1. This can be expected, as the synthesis parameters were kept constant, and only the initial Fe:Ni sulfate concentration varied. The pore size distribution spread
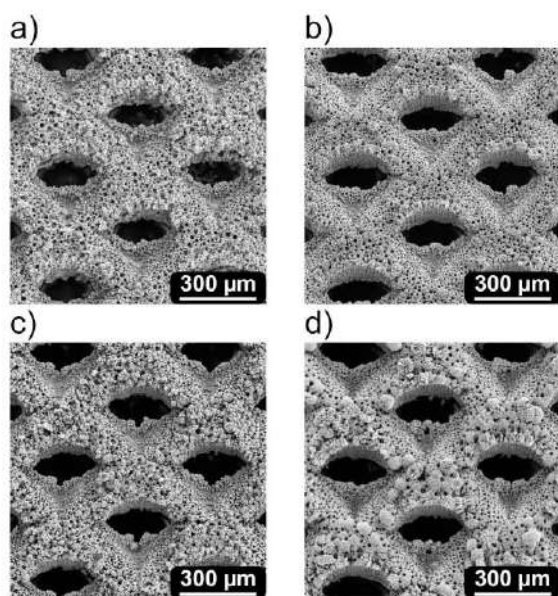
Figure 1. SE micrographs of different FeNi alloy foam compositions on Ti-PTL expanded metal substrates. The apertures of the substrates are indicated in black. Typical morphologies of hydrogen bubble templated materials can be observed. a) 93 at. % Fe, b) 65 at. % Fe, c) 40 at. % Fe, d) 2 at. % Fe

from small pores with a diameter below one micrometer to pores with diameters up to 20 µm. In general, full coverage of the extended Ti PTL substrate is achieved. However, owing to the 3D structure of the substrate, the film quality is not entirely homogeneous. We observed geometrical patterns related to the PTL structure, specifically for compositions with a high Ni content of more than 90 at. %, which resembled pellet-like shapes at the edges of the most elevated parts of the substrate towards the counter anode during electrodeposition. Nevertheless, the basic building blocks were similar and cauliflower-like. Furthermore, in the narrow corners of the 3D structure, the PTL coverage may be lower, as a slightly more pronounced Ti SEM-EDS signal was observed (Figure S2). This is either related to a thinner deposit or could be influenced by the shadowing effects of the EDS signal during the measurement.

Determining the number of active OER sites of FeNi oxyhydroxides in the Faradaic OER region is highly challenging, but of interest to understand the elemental reaction steps.[41] However, the exact OER mechanisms in alkaline media for FeNi electrocatalysts are widely debated and not fully uncovered.[42] As our research approach is based on geometrical current densities, we decided to

8

use a straightforward ECSA determination mainly for comparison purposes.[43,44] Hence, the surface roughness was determined via measuring the double-layer capacitance in a non-Faradaic potential window (Figures S4, S5, and S6).[45] Our roughness analysis revealed comparable surface morphologies for Fe:Ni ratios ranging from 93:7 to 19:81 at. %, which is consistent with our visual SEM analysis. A typical surface roughness factor of 40 was determined and can be considered relatively high when compared to literature data.[46,47] For Ni-rich samples, the roughness increased, which can be attributed to the formation of pellet-like surface structures.

The current density was normalized to the geometric area. We thoroughly investigated the area of each disk employed in the OER measurements using an optical microscope as a quality check of the deposition (Figure S7 and S8). In our GDE setup, the active electrode area is 7.1 mm^2, i.e. a 3 mm Ø disk is exposed to the electrolyte. Therefore, we aligned the catalyst synthesis accordingly and used masks with a round 3 mm opening exposed for deposition. This resulted in slightly smaller film geometries, on average of 5.6 mm^2. This discrepancy of about 20% can be explained by the edge effects of masking during the electrodeposition. Nevertheless, the reported geometrical current densities were normalized to the assumed active area of 7.07 mm^2, as due to the geometries of the electrochemical setup. Therefore, the reported current density-values are likely underestimated and can be understood as a lower limit.

3.2. Electrochemical OER performance at low current density

As discussed in the Introduction, achieving high current densities is one of the primary challenges in alkaline electrolysis. To identify valuable catalyst candidates, current research focuses on the synthesis of novel materials that are often tested and characterized in rotating disk electrode (RDE) configurations. This method has several advantages, such as low material consumption, simple experimental setup, and fast electrochemical characterization. This allows for good comparability between the novel materials and the intrinsic activity data. Often, a benchmark activity of 10 mA cm^{-2} is chosen to compare the so-called onset potential.[45] Despite film homogeneity, substrate coverage, and catalyst morphology, the geometric current density is a widely applied measurement normalization method. We investigated the "onset potentials" of our FeNi foams via slow CV scans using a dry anode configuration. These scans allowed the determination of the corresponding Tafel slopes, which is another commonly used benchmark for comparison (Figure 2).
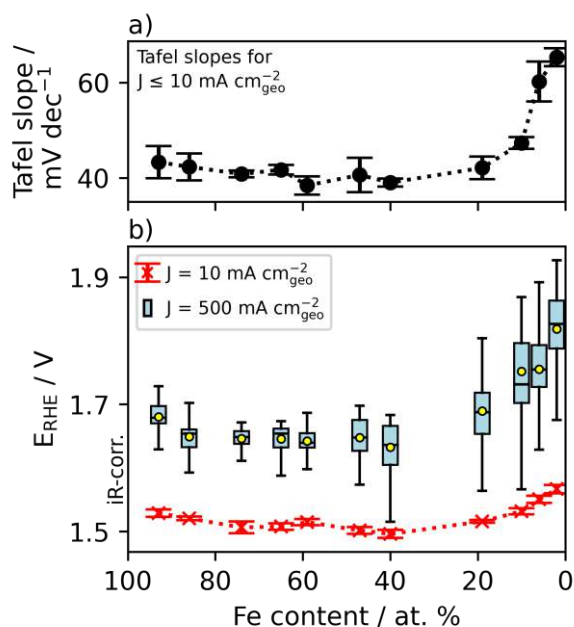
Figure 2. Low current density evaluation. (a) Tafel slope analysis derived from CVs recorded at a scan rate of 5 mV s^{-1}. Four samples were measured and averaged, and the error bars represent the standard deviation. Between 60 and 40 at. % Fe, Tafel slopes below 40 mV dec^{-1} are noted. (b) The "onset potentials" for 10 mA cm^{-2} were derived from CV measurements. They follow the same trend as the quasi steady-state measurements with an enhanced current density of 500 mA cm^{-2}, as depicted using box plots. The mean values are represented by yellow circles and the median values are horizontally black marked within the box.

Tafel analyses have been presented in many publications and can serve to examine the reaction mechanism and rate-determining step of the overall OER.[48] A Tafel analysis using potentiodynamic polarization curves is discussed controversial[49] but commonly used in RDE measurements. However, it has been observed that the electrolyte concentration, scan rate, and rotation speed lead to different Tafel slopes for FeNi electrocatalysts in alkaline OER, making the interpretation of absolute values challenging.[50] Moreover, a wider range of current densities or statistical data are rarely shown, which is unfortunate given that the unit is mV dec^{-1}. Our Tafel analysis involved 30 data points for each sample, with an upper threshold current density of 10 mA cm^{-2}. In this low current density region, we observed linear potential vs. log(J) plots. At slightly higher current densities, linearity was lost (Figure S9), which we attribute to other processes, such as gas bubble formation, rather than a change in the reaction mechanism. The lowest Tafel slopes were measured for FeNi ratios between 60 and 40 at. % Fe, with values below 40 mV dec^{-1}. Other composition ratios were quantified below 50 mV dec^{-1}. For the two Ni-rich samples, we determined 60 mV dec^{-1} or more. Given the comparable values in the literature, we conclude that our synthesized FeNi foams are effective OER catalysts. However, the values are not interpreted further and serve mainly for comparison purposes.

The "onset potentials" were determined between the overpotentials of 260 and 300 mV, with the exception of the two Ni-rich samples, which exceeded 300 mV (Figure S10). This represents for this particular benchmark not "best in class" of FeNi electrodeposited catalysts[51] but is comparable to literature and within the expected range.[29] Nevertheless, the primary objective was to investigate the FeNi alloy compositions under high current densities, which represents a distinct research focus of our group and is discussed in the following.

3.3. Electrochemical OER performance at high current density

In our previous work [16] we faced some challenges to reproduce constant results, as we developed the dry anode setup for alkaline OER. With an advanced setup optimization, we increased the success rate of our experiments to more than 93 %. This study involved 88 sample disk measurements, and only 6 failed our criteria to be accepted and were repeated. Samples were excluded based on three criteria: excessive solution resistance of more than 2 Ω (three cases), lack of ultrasonic pulse interaction (two cases), and one isolated case of inexplicable measurement results. We emphasize that our analysis includes all other obtained measurements without selectively choosing datasets. This approach ensures a comprehensive and unbiased evaluation of the data. A relatively large number of samples was chosen to derive statistical significance and minimize outliers affecting the results. In this context, notable variations were observed between individual samples from the same synthesis by comparing the mean and median potentials required to achieve the respective current densities. Consequently, a replicate synthesis utilizing identical experimental parameters was conducted to assess the reproducibility and dataset progression. Furthermore, the measurement protocol involved the application of galvanostatic pulses, leading to highly transient voltage responses. In this regard, statistical tools, such as box plots and histograms, are preferable to the mean values and standard deviations of small datasets to offer a more detailed understanding. In Figure 3, we provide a comprehensive view of the dataset measured for the 59 at. % Fe alloy composition.
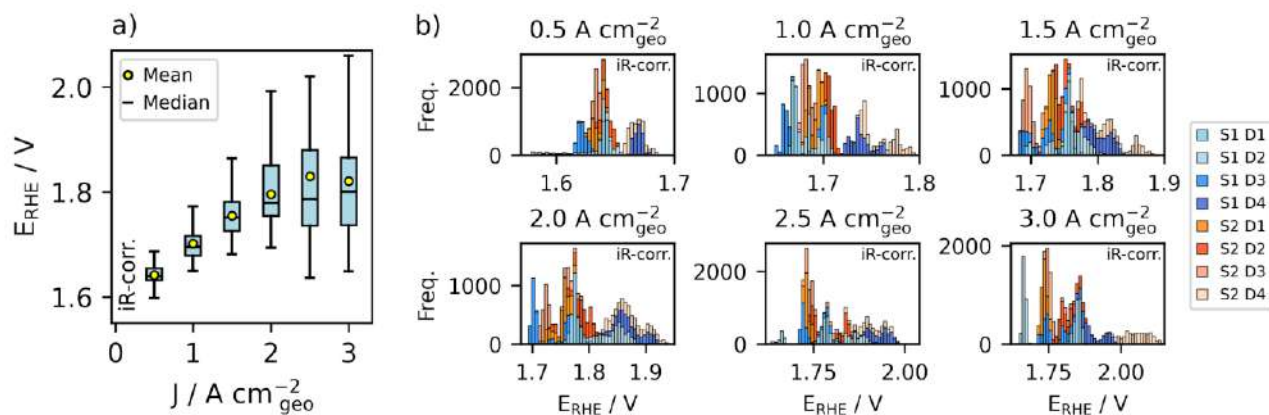
Figure 3. Summary of the 59 at. % Fe alloy foam, including eight individual disk measurements derived from two syntheses (S1 and S2). Given the five-minute OER per

disk and galvanostatic pulsed current density, measured at a frequency of 10 Hz, 144k data points were considered. (a) Box plot of the potential required at the applied current density. In general, the mean and median values are aligned. However, for this particular alloy, the mean deviated to slightly higher potentials than the median at current densities above 2 A cm^{-2}. For the pulsed current density of 3 A cm^{-2}, the deviation between mean and median is 20 mV. By consulting the respective histograms shown in (b), the data structure is clarified, and the contribution of each sample can be identified. The blue scheme depicts the four disks (D1-D4) of the initial synthesis, whereas the red scheme illustrates the disks from the repeated synthesis. Outliers are not shown, and bin size is not specifically normalized.

We present the classical I-V polarization curve using a box plot. In electrochemistry publications, polarization curves frequently represent a single sample, which is designated as representative. This approach is justifiable, given that cleanliness and defined characteristics are desirable. However, we observed variations in the applied potential exceeding 100 mV at similar current densities after iR-correction for samples originating from the same synthesis, rendering the selection of a representative sample difficult. To address this selection process, we implemented a more statistically appropriate reporting method that has been adopted by other electrochemists facing similar challenges.[52,53] The interquartile range (IQR) in a box plot represents 50 % of the measured values (highlighted in blue), encompassing the upper and lower quartiles, with the median positioned between them. The mean value of the dataset is indicated by a round (yellow) marker. The error bars, also referred to as whiskers in a box plot, represent the range of the data outside the IQR, extending to the minimum and maximum values within 1.5 times the IQR from the lower and upper quartiles, respectively. Data points beyond the whiskers are considered outliers, which were not plotted in this instance.

To elucidate the contributions of individual samples in the box plot, we visualized them using separate histograms with a dedicated color code for each disk and synthesis. This approach facilitates a comprehensive understanding of the dataset structure and data symmetry. A normal distribution is characterized by symmetry, wherein the mean is equal to the median and the upper quartile is equal to the lower quartile. Upon evaluation of the initial synthesis, the distributions were determined to be asymmetric. By including a second synthesis, we aimed to enhance the symmetry of the data. This evolution is shown in Figure 3 (b). The first synthesis, represented by bluish colors, was dispersed with several distinct maxima. The mean potential for 3 A cm^{-2} is lower than the median for the first four samples. Conversely, for the second measurement series with the repeated synthesis, the mean potential for 3 A cm^{-2} exceeds the median. Combining the two syntheses mitigates this effect to some extent and the mean approximates the median in the combined dataset. For full transparency, we provide the polarization curves visualized in box plots and their respective histograms for all measured FeNi alloy compositions in a similar manner in the SI (Figure S11). For most of the alloy compositions, we identified a good alignment of the mean and median in the

combined datasets considering the two syntheses. This observation holds true for current densities not exceeding 2 A cm^{-2}, where discrepancies between mean and median values can be more pronounced. At a current density of 3 A cm^{-2}, the deviation between mean and median exceeds 25 mV for two FeNi compositions (47 and 19 at. % Fe). However, a normal distribution with similar upper and lower quartiles is not consistently observed. In cases where the median separates the quartiles into unequal parts, the mean value provides a balanced representation. For medians with smaller lower quartiles, the mean value is consistently larger than the median. Conversely, when the median divides into a larger lower quartile, the mean is lower than the median.

The representation utilizing histograms facilitated the comparison between the initial and repeated syntheses. In general, the second measurement series corroborated the range of the measured values, with the two datasets exhibiting substantial overlap. The best-performing disks for each composition were equally distributed between the two syntheses. Five disks from the first synthesis (93, 74, 59, 10, and 2 at. % Fe) and six disks from the second synthesis demonstrated the best performance for a given FeNi composition, requiring the lowest potential for the applied current density. Notably, for the 40 at. % Fe alloy, the second synthesis surpassed the first, with minimal overlap between the two datasets observed at 2.5 and 3 A cm^{-2}. In conclusion, the second synthesis significantly enhanced the statistical validity of a relatively wide range of measured potentials.

However, this analysis does not fully elucidate the wide range of the measured potentials. The discrepancy between disks from the same synthesis can be attributed to various factors. There is the geometrical aspect, which was previously discussed. Not every disk possesses identical geometries, as illustrated in Figure S8. This had a significant impact, as all disks were normalized using an assumed geometrical area of 7.07 mm^{-2}, which exceeded the exact real area. Considering the normalization to one square centimeter, this represents a relatively small area and is therefore susceptible to normalization error. Additionally, the disks are manually inserted into the dry anode setup through visual centering, which can lead to inaccuracy. During the mounting of the upper cell body, a slight shift may occur, potentially displacing the sample. Furthermore, the contact via the Au mesh used as the current collector varied for each disk. The relative mesh structures of both apertures, the PTL and Au mesh, were slightly different for each measurement. This can result in different gas flow behaviors on a microscopic scale and influence the mass transport. In general, the setup assembly can lead to different individual initial solution resistances, which were measured by a high-frequency AC signal and varied between 200 mΩ and 1.5 Ω. The combination of these effects leads to a spread variation in the potential distribution. Nevertheless, considering the substantial sample size and rigorous statistical methodology employed, it can be concluded that individual discrepancies are counterbalanced, yielding representative results.

Figure 4 presents the electrode potential distributions required to achieve current densities of 1, 2, and 3 A cm^{-2} for the different FeNi alloy compositions comprising the complete datasets using box plots. Compared to the trends observed in the low current density region, the data demonstrate coherence, however, also notable discrepancies. For 1 A cm^{-2}, the data exhibit a clear trend, that is, Fe-rich and Ni-rich alloys require higher electrode potentials than the more equally alloyed samples. Similarly, as observed in the activity data derived from the potential scan. However, discrepancies were observed at an increased current density of 3 A cm^{-2}. For example, in the case of the 59 at. % Fe alloy, where the "onset potential" showed a higher value than its neighboring alloy compositions, i.e. 65 and 47 at. % Fe (Figure 2). At increased current densities, however, this alloy requires lower overpotentials than its neighboring compositions, even representing the most competitive alloy regarding the observed potential to reach 3 A cm^{-2}, i.e., 1.80 V$_{RHE}$ (median), or 1.82 V$_{RHE}$ (mean).
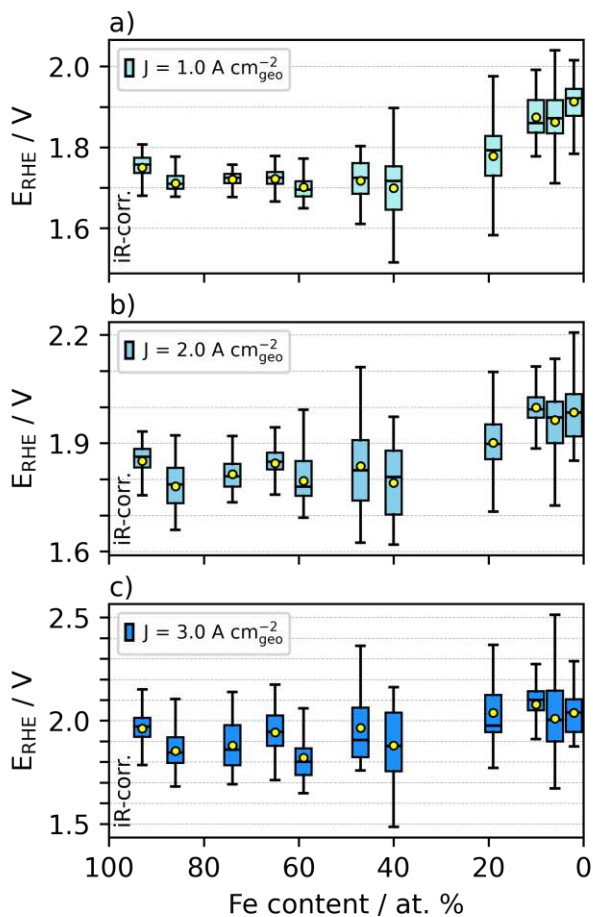
Figure 4. Galvanostatic pulsed current densities were evaluated using box plots. The potentials required to drive a pulsed current density of 1 (a), 2 (b), and 3 (c) A cm^{-2} are shown. At a moderate current density (a), alloy compositions ranging from 86 to 40 at. % Fe require a comparable potential of approximately 1.7 V$_{RHE}$. With increased current density, the potential distribution is increased due to bubble formation, and three local minima occurred at 86, 59, and 40 at. % Fe alloyed foams.

The invar alloy (65 at. % Fe) exhibits a tendency to require larger overpotentials at current densities exceeding 2 A cm^{-2} relative to its neighboring alloy compositions. Given that the alloy exists in a

transitional form between bcc and fcc crystal structures and revealed one of the smallest crystallite size in our XRD measurement, a more amorphous surface and consequently more FeNi oxyhydroxide could have been anticipated at its surface to facilitate the OER. However, this hypothesis could not be supported; instead, a higher potential of approximately 150 mV is necessary to generate an equivalent current density (i.e., 1.95 V_{RHE} (median), 1.94 V_{RHE} (mean)). Notably, the alloy containing 86 at. % Fe achieves a current density of 3 A cm^{-2} at 1.85 V_{RHE} (median and mean). Although its stability requires verification, this alloy composition could be of interest for industrial applications due to the high availability and relatively low cost of iron. Another composition that warrants attention is the 40 at. % Fe alloy. When considering only the second synthesis, the necessary potential to apply the current density of 3 A cm^{-2} was 1.76 V_{RHE} (mean and median). However, considering both syntheses, a required potential of 1.88 V_{RHE} (mean and median) was determined. This represents the largest deviation between the two syntheses of similar alloy compositions and can be attributed to the geometrical disk areas measured using an optical microscope. The first synthesis yielded an average catalytic disk size of 5.3 mm^2, whereas for the second synthesis, an average geometrical area of 6.0 mm^2 was measured. The alloy requiring the highest potential to promote 3 A cm^{-2} contained 10 at. % Fe and necessitated 2.10 V_{RHE} (median) and 2.08 V_{RHE} (mean), respectively. In conclusion, the potential for applying a high current density did not exhibit significant variation over a wide range of FeNi alloy compositions. However, a potential difference of 300 mV was observed between the lowest and highest potentials required to apply a pulsed current density of 3 A cm^{-2}. Three alloy compositions ranging from 83 to 40 at. % Fe are considered promising candidates for further investigation.

3.4. Stability measurement

To investigate the catalytic stability, a similar pulsed galvanostatic protocol was employed to examine the time-dependent behavior at high current densities. Specifically, instead of measuring the potential during 3 A cm^{-2} pulses for five minutes, the measurement duration was substantially extended. Figure 5 presents a 10 h stability measurement, wherein the potential response of an FeNi alloy containing 59 at. % Fe was analyzed. Throughout the measurement, a high-frequency AC signal was superimposed to measure the solution and cell resistances (HFR$_{Sol.}$ and HFR$_{Cell}$) in situ. This was necessary to maintain stable setup conditions. Figure 5 (c) and (g) depict the HFR$_{Sol.}$ oscillations and spikes, respectively. Whereas the oscillations around 0.5 to 1 Ω are tolerated and performance-related, exceeding HFR$_{Sol.}$ above 2 Ω had to be reduced immediately. An exceeding HFR$_{Sol.}$ is related to gas bubble formation between the Luggin capillary and the membrane. Without intervention, HFR$_{Sol.}$ would further increase and the measurement would collapse because of the application of high potentials exceeding 10 V (compliance voltage). The result could be interpreted as an apparent instability of the catalyst film. By applying ultrasonic (US) pulses to the upper cell

compartment filled with 4M KOH, however, gas bubbles could be effectively removed. Therefore, we set the threshold for US pulsing for $HFR_{Sol.}$ to 2 Ω to maintain low solution resistance throughout the experiment. In Figure 5 (c), $HFR_{Sol.}$ exceeded the threshold seven times, and the US pulses successfully re-established stable conditions. Correlation between $HFR_{Sol.}$ and the potentials are shown in Figures 5 (f) and (g). Although the potential was iR-corrected, the potential response was directly coupled to the solution resistance. Interestingly, $HFR_{Sol.}$ increases stepwise, whereas recovery and bubble release progress continuously. This recovery can be attributed to the electrochemical pulsing, which allows resting time between active and inactive OER phases. Figures 5 (d) and (h) show the HFR_{Cell} evolution, which oscillated between 10 and 16 Ω. This is related to the set threshold for US pulsing, which was 16 Ω for HFR_{Cell}. The 10 Ω value corresponds to bubble-free conditions after US pulsing. HFR_{Cell} steadily increased thereafter at typical intervals of 15 min to reach the threshold value again. We attribute this to bubble formation on top of the membrane, which could be correlated to cross-over bubbles.[54]

After 1 h, no sample degradation was observed. The mean potential required to apply the desired current density was 1.80 V_{RHE}, which is in good agreement with previously discussed results. However, with an extended duration, some performance degradation became evident. During the 10th hour, the necessary potential to deliver the desired current increased for active OER averaged to 2.13 V_{RHE} (Figure 6). By applying a linear regression through the mean potentials required for the average current density per hour, we obtained a degradation of 35 mV h^{-1} ($R^2 = 0.991$). This value indicates that the synthesized catalysts are not stable during extended high current density operation.
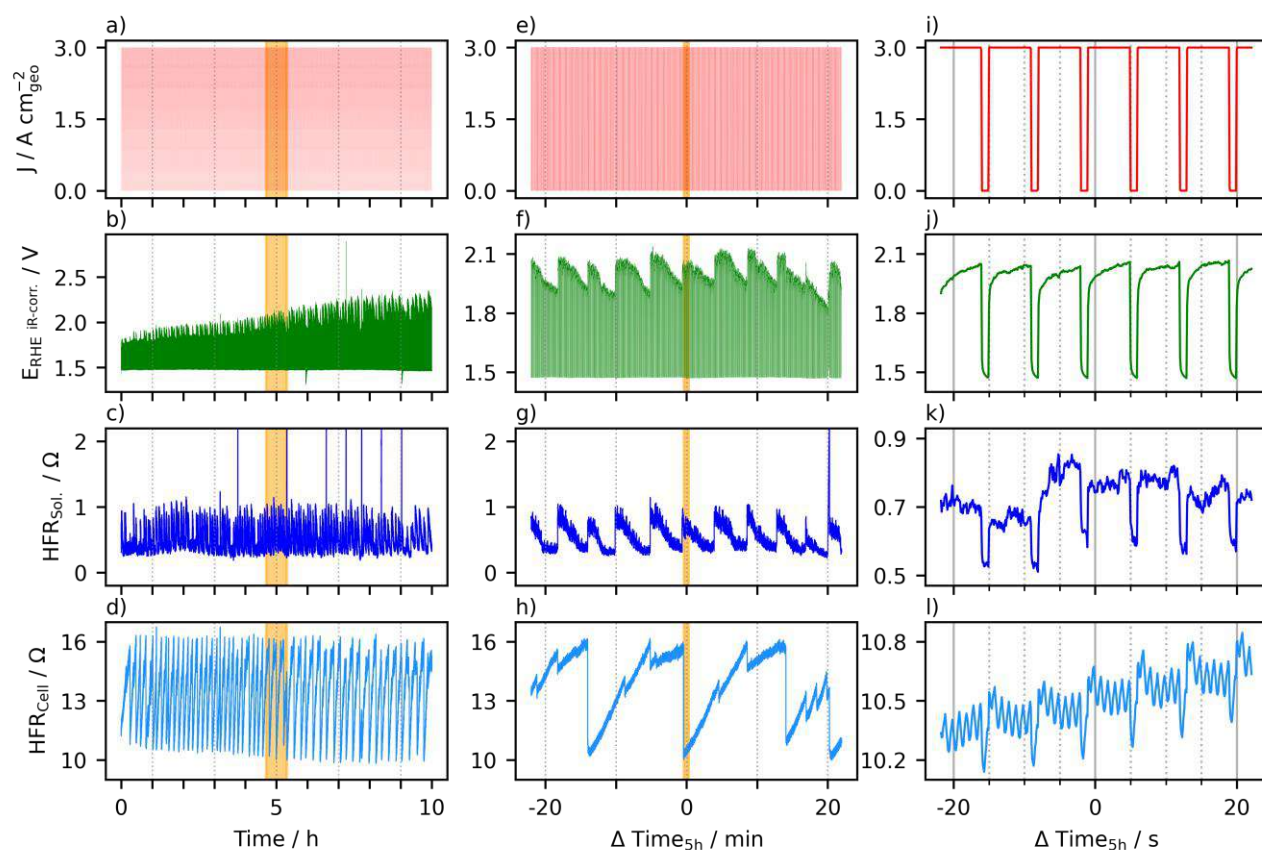
Figure 5. Stability test of a 59 at. % Fe alloy disk with a pulsed galvanostatic current density of 3 A cm^{-2} for 10 h. Pulse duration was 6 s, followed by 1 s with no current. (a) to (d) The representation of the entire dataset reveals a certain degradation (b), the potential at zero current is constant. HFR$_{Sol.}$ and HFR$_{Cell}$ remained within specific ranges, several spikes were observed. Highlighted in orange is the 40 min timeframe around 5 h, as shown in (e) to (h). Two different oscillation patterns were observed. The potential oscillations (iR-corrected) were directly coupled to the HFR$_{Sol.}$ evolution. HFR$_{Cell}$ increased from approximately 10 Ω to 16 Ω within 15 min, HFR$_{Sol.}$ oscillates at a frequency of approximately 5 min. Highlighted in orange is the 40 s timeframe around 5 h, as shown in (i) to (l). Individual pulses are presented. HFR$_{Sol.}$ changed during the OER active and inactive phases by approximately 80 mΩ.

The observed degradation can be attributed to several factors. The FeNi alloy was electroplated onto a Ti-PTL. This PTL corrodes under alkaline OER conditions and is completely inactive for the OER.[16] A potential corrosion process, initiating from the edges of the disks, may gradually progress towards the center of the catalytic disk, resulting in a reduction in the number of active sites. The sample was thermally heated for an extended duration. This could lead to gradual dehydration of the anode, a phenomenon observed in dry cathode applications.[11] A drier surface inhibits hydroxide conductivity within the hydrated layer on the catalytic surface and increases internal resistivity. Furthermore, upon a detailed analysis of the pulse characteristics, we observed an increasing capacitive contribution over time (Figure S13). This can be attributed to repeated cycling, potentially leading to mechanical stress and catalyst degradation. Membrane degradation could be another contributing factor;[55] however, as HFR$_{Sol.}$ remained constant, we do not consider this to be a

significant issue. Our in situ $HFR_{Sol.}$ measurement allowed us to compare the effect of the active OER solution resistance increase against inactive phases. On average, for the 10 h test, we measured $HFR_{Sol.}$ in the active OER phase to be 534 mΩ, in the inactive phase it was 451 mΩ. This represented a relative increase of 18 % for the active OER phases. This result is likely relative and setup-dependent. However, other studies reveal a similar trend and emphasize the importance of accurate solution resistance determination for subsequent iR-correction.[56]
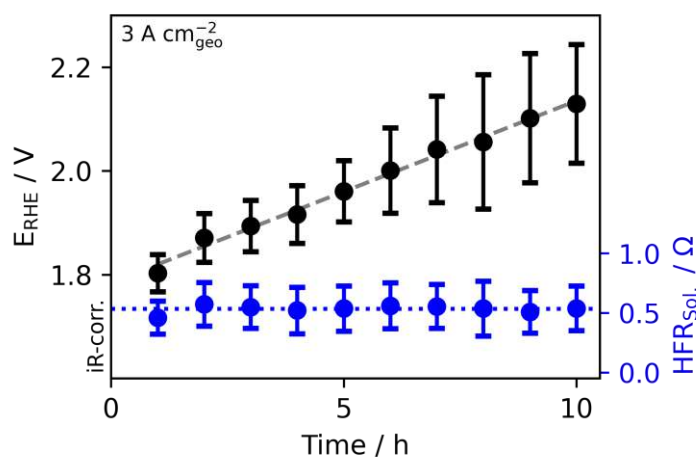
Figure 6. Evaluation of the applied potentials during the stability test. After one hour of operation, no degradation was remarked. With continuous duration, the linear sample degradation was 35 mV h^{-1}. Maintaining a low solution resistance over the entire duration revealed no membrane degradation and stable cell conditions, which translates to effective sample performance loss.

4. Conclusions

This study investigated the performance of porous FeNi alloy foams as OER catalysts in a dry anode setup for alkaline water electrolysis. The setup was capable of testing promising catalyst candidates at high geometrical currents of up to 3 A cm^{-2} under experimental settings that can mimic large-scale application conditions. The catalysts were evaluated using pulsed electrolysis to address the intermittent current supply associated with renewable energy and to facilitate bubble release. An advantage of this configuration compared to a dry cathode is its polarity. The anode attracts hydroxides through the membrane, where they can react into oxygen and water. Thereby the humidification of the anode is essential to maintain the membrane interface moisture and hydroxide conductivity on the catalytic coating. Therefore, water vapor is supplied and "dry" refers to the fact, that the electrode is not directly immersed in a liquid alkaline electrolyte. This is beneficial for the enhanced mass transport of the gaseous oxygen product, which is effectively released at the anode and allows for relatively low overpotential. Furthermore, a low internal resistance allows for an efficient process. However, bubble related issues must be addressed in the cathode compartment. In principle, the setup could also be implemented in a pressurized system and evaluated at higher temperatures to enhance catalytic activity. In the low current density range, the setup is capable of

characterizing the FeNi catalysts accordingly. Alloys with 60 to 40 at. % Fe exhibited Tafel slopes below 40 mV dec^{-1} and "onset potentials" between 260 and 290 mV to reach 10 mA cm^{-2}. Higher current densities up to 3 A cm^{-2} were evaluated using box plots. This approach ensured the unbiased and statistical presentation of all measurements, which comprised 88 sample disks. A wide range of FeNi alloy compositions, ranging from 93 to 2 at. % Fe, was synthesized, and every alloy composition was resynthesized to address reproducibility. At high current densities, the three composition ranges showed promising performance, that is, 86, 59, and 40 at. % Fe. The alloy with 59 at. % Fe reached 3 A cm^{-2} at an averaged potential of 1.82 V$_{RHE}$, while the other two promising compositions requested a 30, resp. 60 mV higher potential to reach the similar current density on average. A 10 h stability test of the 59 at. % Fe alloy at pulsed galvanostatic current density of 3 A cm^{-2} showed an initial stable performance for 1 hour, followed by degradation at a rate of 35 mV h^{-1}. Further work is required to optimize the catalyst composition and structure for enhanced long-term stability at high current densities. In particular, replacing the Ti-PTL substrate with stainless steel or Ni-based material would be beneficial for preventing corrosion.

Author Contributions

Etienne Berner: Sample synthesis and preparation, electrochemical measurements, data curation, GDE setup optimization, SEM-EDS and XRD measurements, conceptualization, paper writing.
Gustav K. H. Wiberg: GDE setup optimization, reviewing, editing.
Matthias Arenz: Supervision, conceptualization, reviewing, editing.

Conflicts of Interest

The authors declare no conflicts.

Acknowledgements

References

1   M. van der Spek, C. Banet, C. Bauer, P. Gabrielli, W. Goldthorpe, M. Mazzotti, S. T. Munkejord, N. A. Røkke, N. Shah, N. Sunny, D. Sutter, J. M. Trusler and M. Gazzani, *Energy Environ. Sci.*, 2022, **15**, 1034–1077.
2   P. Nikolaidis and A. Poullikkas, *Renew. Sustain. Energy Rev.*, 2017, **67**, 597–611.
3   A. Boretti and B. K. Banik, *Adv. Energy Sustain. Res.*, 2021, **2**, 1–10.
4   H. A. Miller, K. Bouzek, J. Hnat, S. Loos, C. I. Bernäcker, T. Weißgärber, L. Röntzsch and J.

Meier-Haack, *Sustain. Energy Fuels*, 2020, **4**, 2114–2133.

5   N. Du, C. Roy, R. Peach, M. Turnbull, S. Thiele and C. Bock, *Chem. Rev.*, 2022, **122**, 11830–11895.
6   Y. Sugawara, S. Sankar, S. Miyanishi, R. Illathvalappil, P. K. Gangadharan, H. Kuroki, G. M. Anilkumar and T. Yamaguchi, *J. Chem. Eng. Japan*, 2023, **56**.
7   M. Chatenet, B. G. Pollet, D. R. Dekel, F. Dionigi, J. Deseure, P. Millet, R. D. Braatz, M. Z. Bazant, M. Eikerling, I. Staffell, P. Balcombe, Y. Shao-Horn and H. Schäfer, *Chem. Soc. Rev.*, 2022, **51**, 4583–4762.
8   A. Lim, H. Kim, D. Henkensmeier, S. Jong Yoo, J. Young Kim, S. Young Lee, Y.-E. Sung, J. H. Jang and H. S. Park, *J. Ind. Eng. Chem.*, 2019, **76**, 410–418.
9   D. Xu, M. B. Stevens, M. R. Cosby, S. Z. Oener, A. M. Smith, L. J. Enman, K. E. Ayers, C. B. Capuano, J. N. Renner, N. Danilovic, Y. Li, H. Wang, Q. Zhang and S. W. Boettcher, *ACS Catal.*, 2019, **9**, 7–15.
10 R. Wang, M. Ohashi, M. Ishida and H. Ito, *Int. J. Hydrogen Energy*, 2022, **47**, 40835–40848.
11 S. Koch, J. Disch, S. K. Kilian, Y. Han, L. Metzler, A. Tengattini, L. Helfen, M. Schulz, M. Breitwieser and S. Vierrath, *RSC Adv.*, 2022, **12**, 20778–20784.
12 N. Chen, S. Y. Paek, J. Y. Lee, J. H. Park, S. Y. Lee and Y. M. Lee, *Energy Environ. Sci.*, 2021, **14**, 6338–6348.
13 Y. Zheng, W. Ma, A. Serban, A. Allushi and X. Hu, *Angew. Chemie Int. Ed.*, 2024, e202413698.
14 S. Marini, P. Salvi, P. Nelli, R. Pesenti, M. Villa and Y. Kiros, *Int. J. Hydrogen Energy*, 2013, **38**, 11496–11506.
15 M. Koj, J. Qian and T. Turek, *Int. J. Hydrogen Energy*, 2019, **44**, 29862–29875.
16 E. Berner, G. K. H. Wiberg and M. Arenz, *Adv. Energy Sustain. Res.*, 2024, **5**, 2400050.
17 J. Bleeker, C. van Kasteren, J. R. van Ommen and D. A. Vermaas, *Int. J. Hydrogen Energy*, 2024, **57**, 1398–1407.
18 V. Karimi, R. Sharma, P. Morgen and S. M. Andersen, *ACS Appl. Mater. Interfaces*, 2023, **15**, 49233–49245.
19 F. Rocha, R. Delmelle, C. Georgiadis and J. Proost, *J. Environ. Chem. Eng.*, 2022, **10**, 107648.
20 F. Yang, M. J. Kim, M. Brown and B. J. Wiley, *Adv. Energy Mater.*, 2020, **10**, 2001174.
21 M. Ali and F. Ahmad, *Mater. Manuf. Process.*, 2019, **34**, 1580–1604.
22 A. Sahoo and V. R. R. Medicherla, *Mater. Today Proc.*, 2020, **43**, 2242–2244.
23 T. Waeckerlé, A. Demier, F. Godard and H. Fraisse, *J. Magn. Magn. Mater.*, 2020, **505**, 166635.
24 F. Song, L. Bai, A. Moysiadou, S. Lee, C. Hu, L. Liardet and X. Hu, *J. Am. Chem. Soc.*, 2018, **140**, 7748–7759.
25 M. Gong and H. Dai, *Nano Res.*, 2015, **8**, 23–39.
26 Y. Zhou, Z. Wang, M. Cui, H. Wu, Y. Liu, Q. Ou, X. Tian and S. Zhang, *Adv. Funct. Mater.*, 2024, **2410618**, 1–26.
27 L. Magnier, G. Cossard, V. Martin, C. Pascal, V. Roche, E. Sibert, I. Shchedrina, R. Bousquet, V. Parry and M. Chatenet, *Nat. Mater.*, 2024, **23**, 252–261.
28 H. R. Zamanizadeh, S. Sunde, B. G. Pollet and F. Seland, *Electrochim. Acta*, 2022, **424**, 140561.
29 J. Zhao, J. Zhang, Z. Li and X. Bu, *Small*, 2020, **16**, 1–23.
30 M. W. Louie and A. T. Bell, *J. Am. Chem. Soc.*, 2013, **135**, 12329–12337.
31 P. M. Bodhankar, P. B. Sarawade, G. Singh, A. Vinu and D. S. Dhawale, *J. Mater. Chem. A*, 2021, **9**, 3180–3208.
32 P. Arévalo-Cid, M. F. Vaz and M. F. Montemor, *Mater. Charact.*, 2022, **193**, 112311.
33 V. Torabinejad, M. Aliofkhazraei, S. Assareh, M. H. Allahyarzadeh and A. S. Rouhaghdam, *J. Alloys Compd.*, 2017, **691**, 841–859.
34 H. Dahms and I. M. Croll, *J. Electrochem. Soc.*, 1965, **112**, 771.
35 G. K. H. Wiberg, M. Fleige and M. Arenz, *Rev. Sci. Instrum.*, 2015, **86**, 024102.
36 M. Inaba, A. W. Jensen, G. W. Sievers, M. Escudero-Escribano, A. Zana and M. Arenz, *Energy Environ. Sci.*, 2018, **11**, 988–994.
37 G. K. H. Wiberg, S. Nösberger and M. Arenz, *Curr. Opin. Electrochem.*, 2022, **36**, 101129.
38 J. Schröder, V. A. Mints, A. Bornet, E. Berner, M. Fathi Tovini, J. Quinson, G. K. H. Wiberg, F. Bizzotto, H. A. El-Sayed and M. Arenz, *JACS Au*, 2021, jacsau.1c00015.
39 S. Zhang and S. Kobayashi, *J. Mater. Sci.*, 2021, **56**, 9484–9498.
40 J. F. Valderruten, G. A. Pérez Alcázar and J. M. Grenèche, *J. Phys. Condens. Matter*, 2008,

20, 485204.

41   S. S. Jeon, P. W. Kang, M. Klingenhof, H. Lee, F. Dionigi and P. Strasser, *ACS Catal.*, 2023, **13**, 1186–1196.

42   J. Mohammed-Ibrahim, *J. Power Sources*, 2020, **448**, 227375.

43   D. Voiry, M. Chhowalla, Y. Gogotsi, N. A. Kotov, Y. Li, R. M. Penner, R. E. Schaak and P. S. Weiss, *ACS Nano*, 2018, **12**, 9635–9638.

44   D. Li, C. Batchelor-McAuley and R. G. Compton, *Appl. Mater. Today*, 2020, **18**, 100404.

45   C. C. L. McCrory, S. Jung, J. C. Peters and T. F. Jaramillo, *J. Am. Chem. Soc.*, 2013, **135**, 16977–16987.

46   A. Hodges, A. L. Hoang, G. Tsekouras, K. Wagner, C. Y. Lee, G. F. Swiegers and G. G. Wallace, *Nat. Commun.*, 2022, **13**, 1–11.

47   A. Iarchuk, A. Dutta and P. Broekmann, *J. Hazard. Mater.*, 2022, **439**, 129504.

48   T. Shinagawa, A. T. Garcia-Esparza and K. Takanabe, *Sci. Rep.*, 2015, **5**, 13801.

49   S. Anantharaj, S. Noda, M. Driess and P. W. Menezes, *ACS Energy Lett.*, 2021, **6**, 1607–1611.

50   O. van der Heijden, S. Park, J. J. J. Eggebeen and M. T. M. Koper, *Angew. Chemie Int. Ed.*, 2023, **62**, 1–9.

51   J. Jin, J. Xia, X. Qian, T. Wu, H. Ling, A. Hu, M. Li and T. Hang, *Electrochim. Acta*, 2019, **299**, 567–574.

52   H. Giess, *J. Power Sources*, 1995, **53**, 31–43.

53   M. Kasper, A. Leike, J. Thielmann, C. Winkler, N. Al-Zubaidi R-Smith and F. Kienberger, *J. Power Sources*, 2022, **536**, 231407.

54   J. W. Haverkort and H. Rajaei, *J. Power Sources*, 2021, **497**, 229864.

55   D. Li, A. R. Motz, C. Bae, C. Fujimoto, G. Yang, F.-Y. Zhang, K. E. Ayers and Y. S. Kim, *Energy Environ. Sci.*, 2021, **14**, 3393–3419.

56   R. Lira Garcia Barros, M. H. G. Kelleners, L. van Bemmel, T. V. N. van der Leegte, J. van der Schaaf and M. T. de Groot, *Electrochim. Acta*, 2024, **507**, 145161.

Investigation of FeNi alloy foams at high oxygen evolution reaction rates using a dry anode setup in alkaline environment

Etienne Berner,[1] Gustav K. H. Wiberg,[1] Matthias Arenz[1*]

1: Department of Chemistry, Biochemistry and Pharmaceutical Sciences, University of Bern, Bern, Switzerland

* Corresponding Author: Prof. Dr. M. Arenz (matthias.arenz@unibe.ch)

Selected plating bath pH- and electronic conductivity values

Fe:Ni ratio in solution:	10:1	5:1	2:1	1:20	1:100
Initial pH	1.5	1.5	1.6	1.6	1.6
Post deposition pH	1.5	1.5	1.5	1.5	1.5
Initial conductivity [mS/cm]	84	84	84	85	85
Post depo. conductivity [mS/cm]	85	85	85	84	83

Table S1. The initial values of pH and electronic conductivity of selected plating bath compositions and the same measurements after three foam electrodepositions revealed a comparable solution quality. No significant differences were observed among the compositions.

Photograph of the plating baths
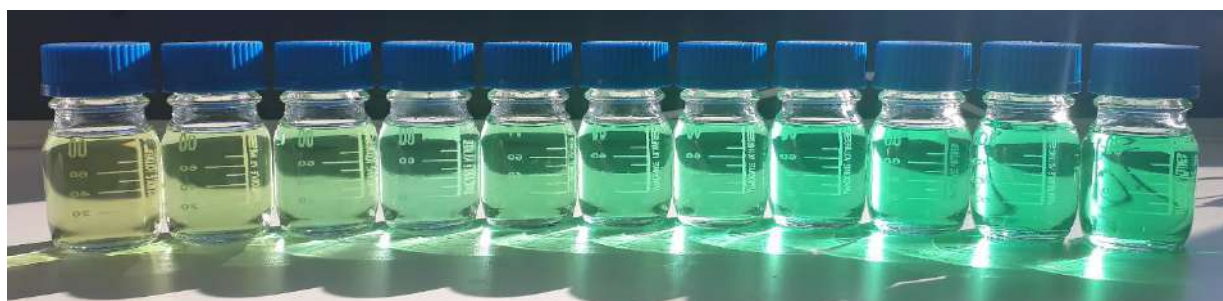
Figure S1. The eleven plating solutions with different Fe:Ni ratios are shown after several months of storage. Various electrodepositions (in a minimum of five) were performed with each of these baths. No precipitations are visible, all solutions are clear. The left panel represents the highest Fe content and the right represents the highest Ni content. Metal salt concentration is 0.2 M with Fe:Ni ratios (from left to right): 10:1, 5:1, 2:1, 1.5:1, 1:1, 1:1.5, 1:2, 1:5, 1:10, 1:20 and 1:100.

SEM-EDS composition analysis

	Fe [at. %]	Ni [at. %]	Ti [at. %]	Ø of 2 samples
synthesis i)	93 / 93 / 93	6 / 6 / 6	1 / 1 / 1	
Ø of 3 EDS maps	**93**	**6**	**1**	
synthesis ii)	92 / 93 / 93	7 / 7 / 7	1 / 1 / 1	**93 at. % Fe**
Ø of 3 EDS maps	**93**	**7**	**1**	
synthesis i)	87 / 87 / 87	12 / 12 / 12	1 / 1 / 1	
Ø of 3 EDS maps	**87**	**12**	**1**	
synthesis ii)	85 / 84 / 85	14 / 14 / 13	2 / 2 / 2	**86 at. % Fe**
Ø of 3 EDS maps	**85**	**14**	**2**	
synthesis i)	72 / 72 / 72	27 / 27 / 27	1 / 1 / 1	
Ø of 3 EDS maps	**72**	**27**	**1**	
synthesis ii)	75 / 76 / 76	23 / 23 / 23	2 / 1 / 1	**74 at. % Fe**
Ø of 3 EDS maps	**76**	**23**	**1**	
synthesis i)	65 / 64 / 65	35 / 35 / 35	1 / 0 / 0	
Ø of 3 EDS maps	**65**	**35**	**0**	
synthesis ii)	65 / 65 / 65	35 / 35 / 35	0 / 0 / 0	**65 at. % Fe**
Ø of 3 EDS maps	**65**	**35**	**0**	
synthesis i)	57 /57 / 57	43 / 43 / 43	0 / 0 / 0	
Ø of 3 EDS maps	**57**	**43**	**0**	
synthesis ii)	60 / 60 / 61	39 / 39 / 38	1 / 1 / 1	**59 at. % Fe**
Ø of 3 EDS maps	**60**	**39**	**1**	
synthesis i)	48 / 48 / 48	51 / 50 / 51	1 / 2 / 1	
Ø of 3 EDS maps	**48**	**51**	**1**	
synthesis ii)	46 / 46 / 46	53 / 53 / 53	1 / 1 / 1	**47 at. % Fe**
Ø of 3 EDS maps	**46**	**53**	**1**	
synthesis i)	41 / 40 / 40	59 / 60 / 60	0 / 0 / 0	
Ø of 3 EDS maps	**40**	**60**	**0**	
synthesis ii)	40 / 40 / 40	60 /60 / 60	1 / 1 / 1	**40 at. % Fe**
Ø of 3 EDS maps	**40**	**60**	**1**	
synthesis i)	20 / 20 / 20	80 / 80 / 80	0 / 0 / 0	
Ø of 3 EDS maps	**20**	**80**	**0**	
synthesis ii)	18 / 18 / 18	82 / 82 / 82	0 / 0 / 0	**19 at. % Fe**
Ø of 3 EDS maps	**18**	**82**	**0**	
synthesis i)	10 / 10 / 10	90 / 89 / 89	0 / 0 / 0	
Ø of 3 EDS maps	**10**	**89**	**0**	
synthesis ii)	10 / 10 / 10	90 / 90 / 90	0 / 0 / 0	**10 at. % Fe**
Ø of 3 EDS maps	**10**	**90**	**0**	
synthesis i)	6 / 6 / 6	93 / 93 / 93	1 / 1 / 1	
Ø of 3 EDS maps	**6**	**93**	**1**	
synthesis ii)	6 / 6 / 6	94 / 94 / 94	0 / 0 / 0	**6 at. % Fe**
Ø of 3 EDS maps	**6**	**94**	**0**	
synthesis i)	2 / 2 / 2	98 / 98 / 98	0 / 1 / 1	
Ø of 3 EDS maps	**2**	**98**	**1**	
synthesis ii)	2 / 2 / 2	98 / 98 / 98	0 / 0 / 0	**2 at. % Fe**
Ø of 3 EDS maps	**2**	**98**	**0**	

Table S2. FeNi alloy composition analysis of the atomic percentages of each catalyst synthesis derived by SEM-EDS. The contents were normalized to Fe, Ni, and Ti. Each sample was measured at three individual spots using map spectra. The three measured atomic weights were averaged for each metal. Synthesis i) and ii) refer to individual samples with similar compositions, which were combined using the average iron content.

Exemplarily selected SEM-EDS maps
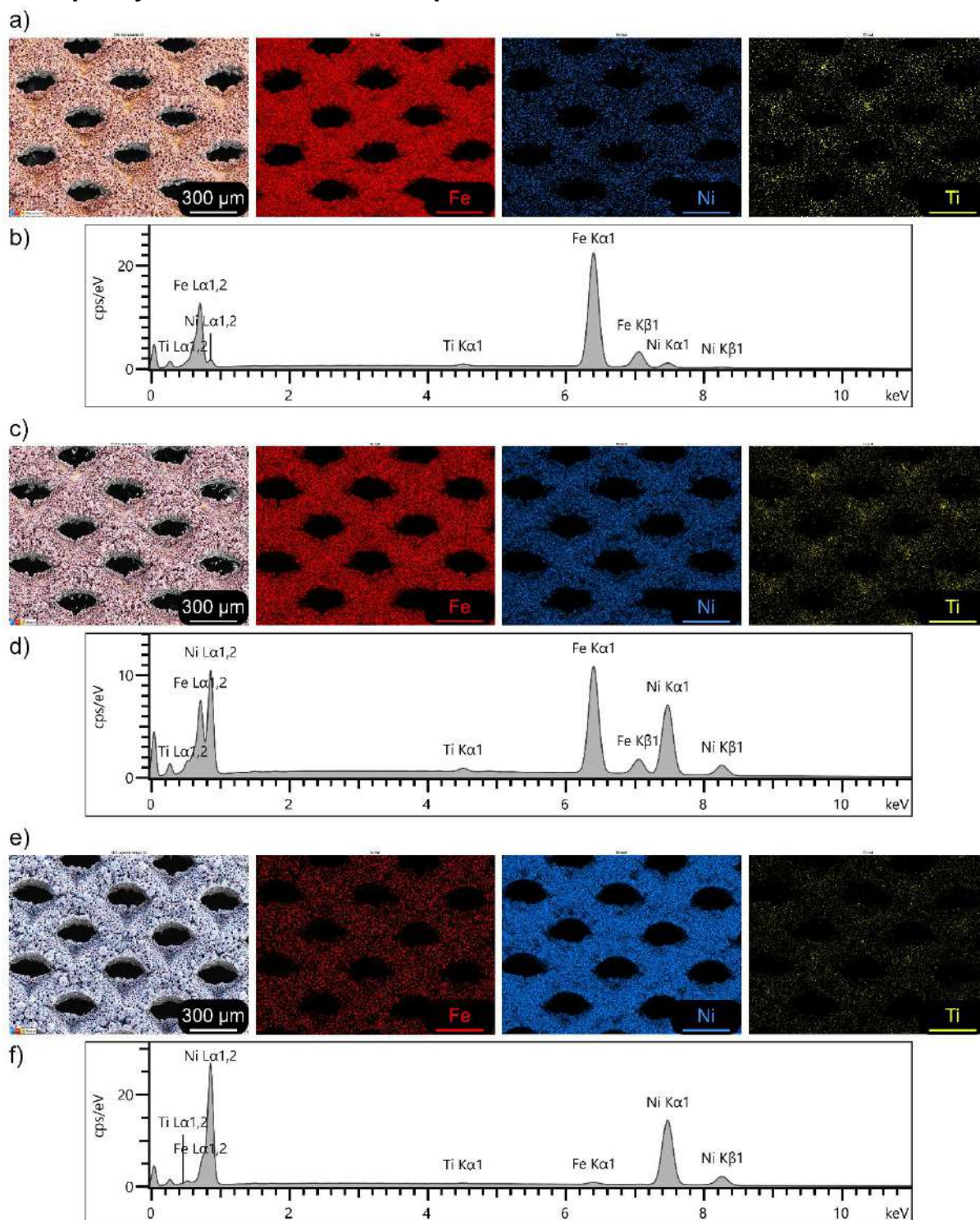
Figure S2. EDS color maps and map sum spectra of three selected electrodeposited samples.
a) and b): Fe (92.5 at. %), Ni (6.8 at. %) and Ti (0.7 at. %)
c) and d): Fe (46.1 at. %), Ni (53.1 at. %) and Ti (0.8 at. %)
e) and f): Fe (1.6 at. %), Ni (98.1 at. %) and Ti (0.3 at. %)
Map dimensions are 1.52 x 1.14 mm^2 with 2048 x 1536 pixel resolution. The dwell time was 30 μs (94.3 s measurement time), and the total counts per map exceeded 10^6. To export the color maps, a binning factor of four was applied.

X-ray diffraction
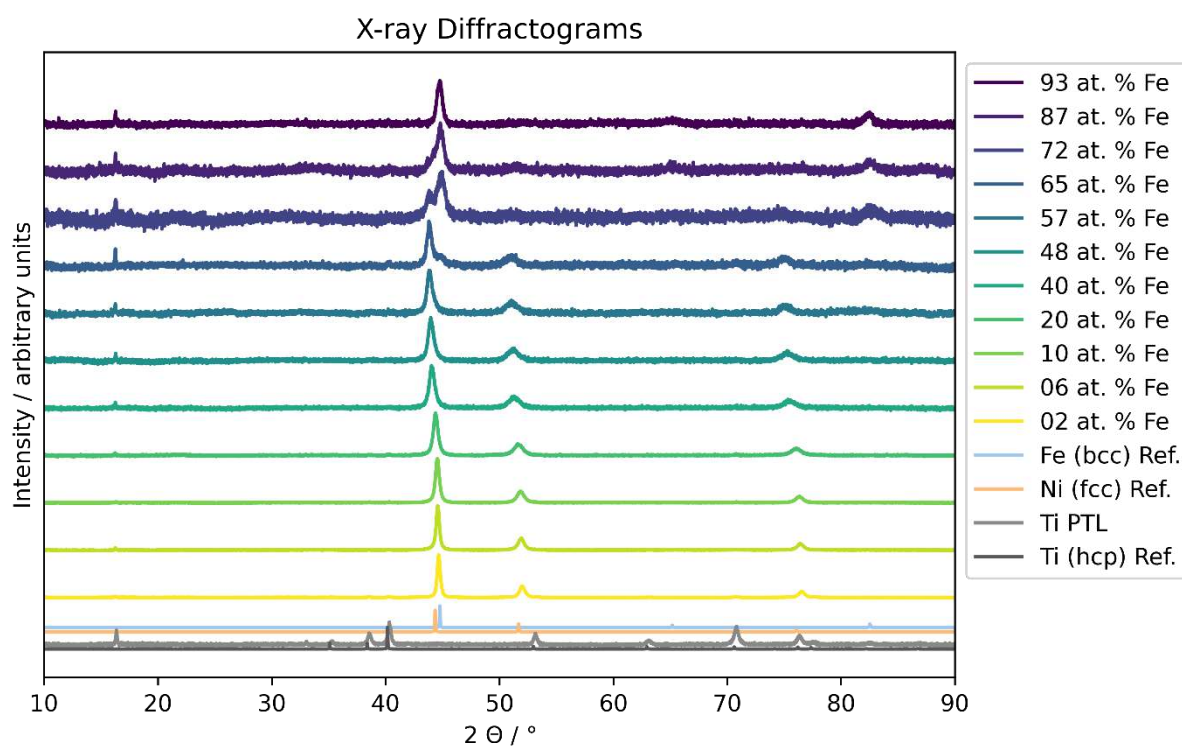
Figure S3. Peak-height normalized and background-corrected X-ray diffractograms of electrodeposited FeNi alloy foams. The iron-rich sample aligns with the Fe body-centered cubic (bcc) structure and transforms into a Ni face-centered cubic (fcc) structure with enhanced Ni content. The most pronounced double peak, at 72 at. % Fe, is characteristic for "invar alloy", interestingly its also the most amorphous sample given the lowest absolute peak height. The fcc crystal size of Fe:Ni samples with min. 60 at. % Fe increased with larger Ni content, given the absolute peak height increased.

CVs to visualize the non-Faradaic potential window
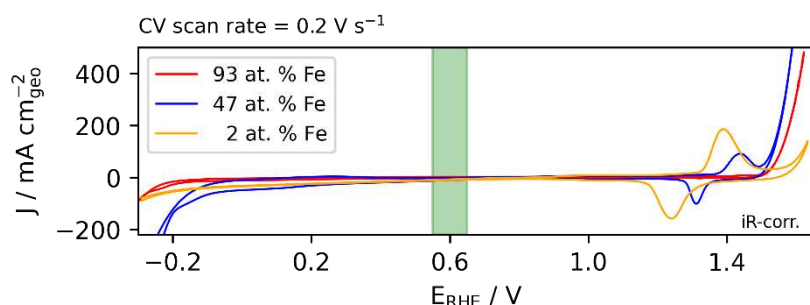
Figure S4. The selected CVs were measured using the dry anode setup. Depicted are the final CVs of the respective samples spanning the potential window from the hydrogen evolution reaction to the oxygen evolution reaction (HER to OER). The green shaded potential window from 0.55 to 0.65 V_{RHE} was chosen to determine the double-layer capacitance of each composition (Figure S5).
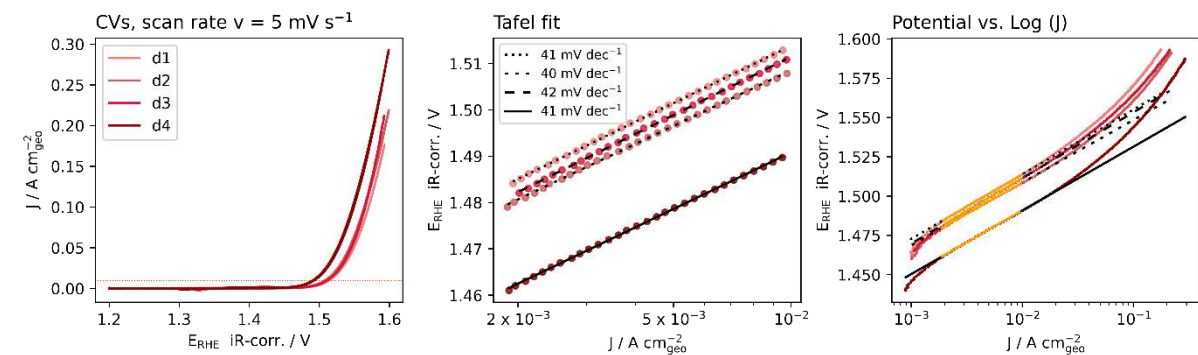
CVs to determine the double-layer capacity
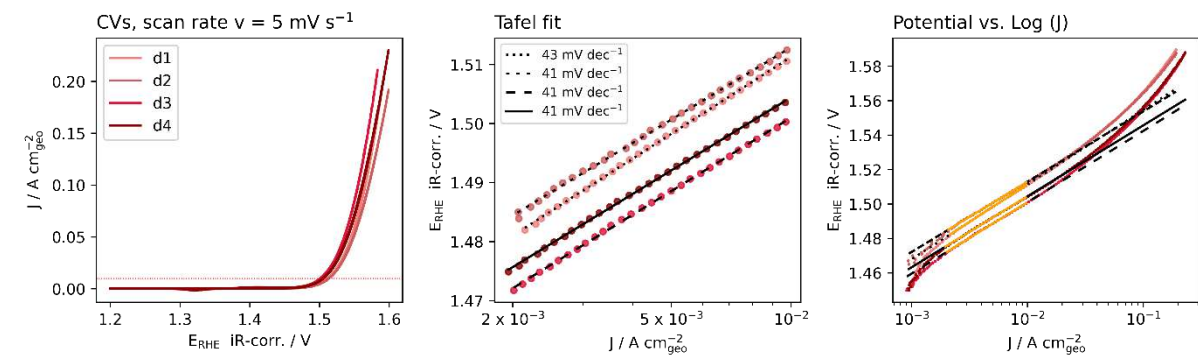
a) 93 at. % Fe
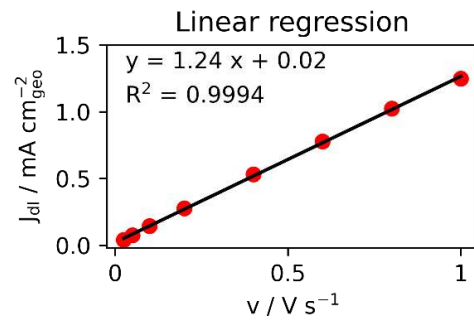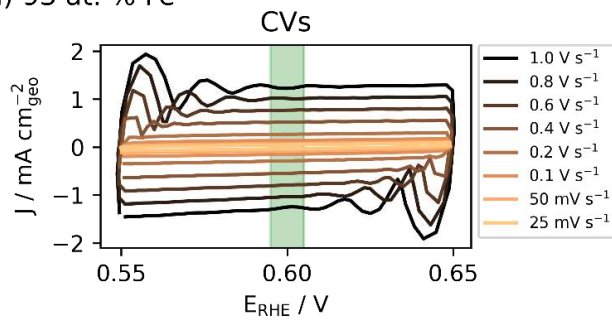
b) 86 at. % Fe
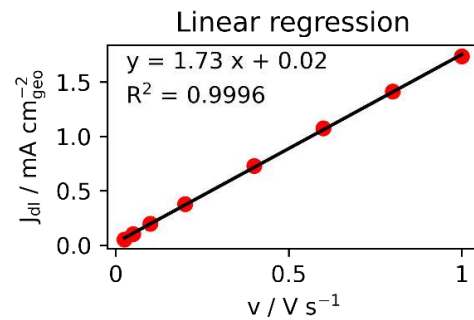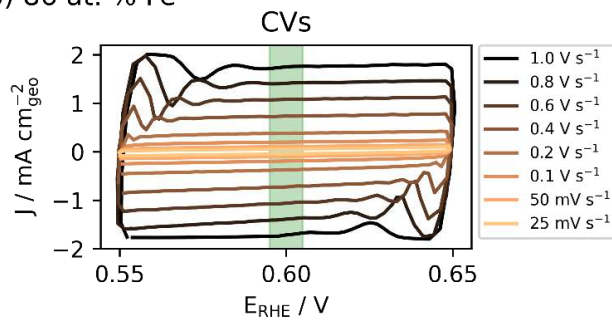
c) 74 at. % Fe

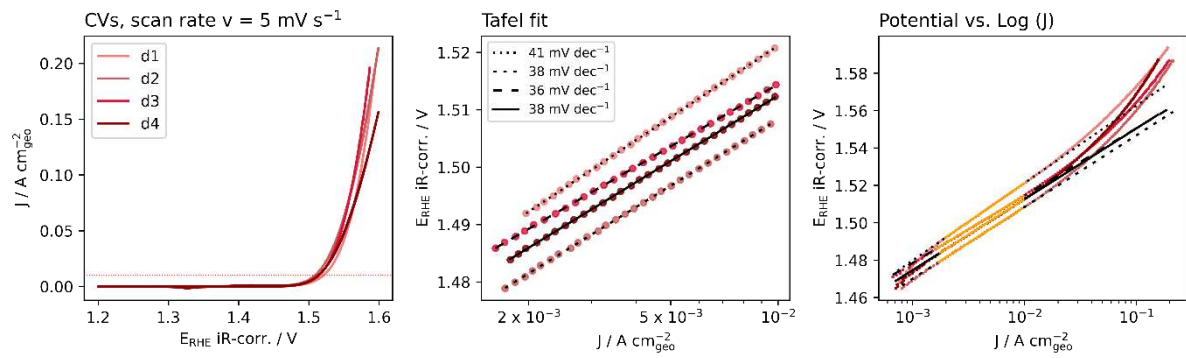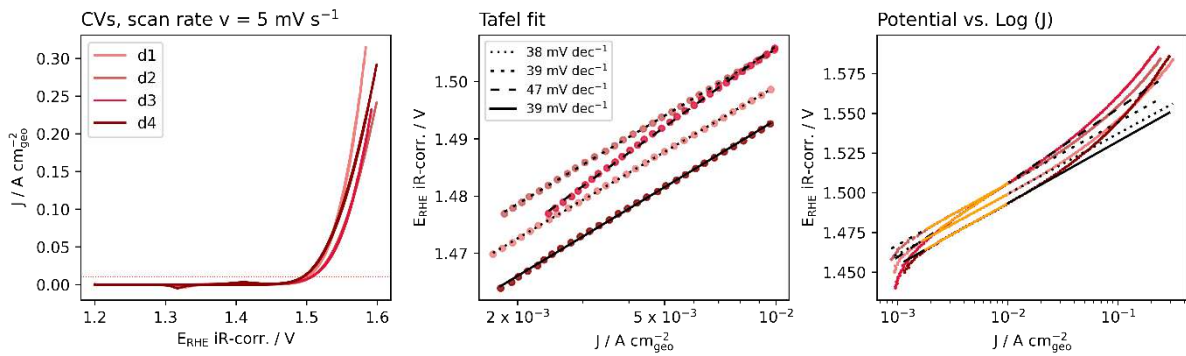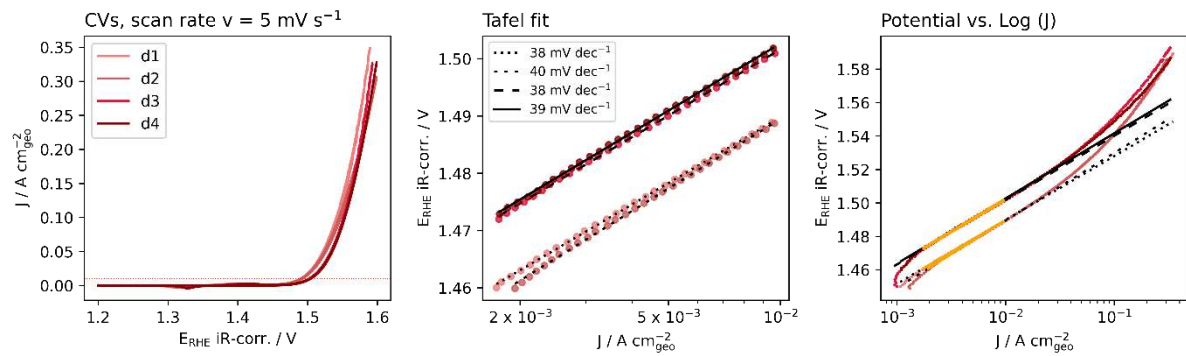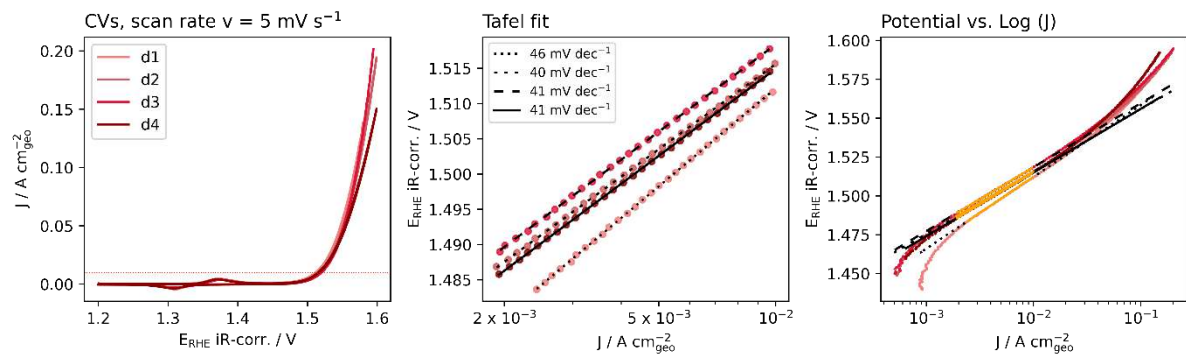### d) 65 at. % Fe

e) 59 at. % Fe

f) 47 at. % Fe

g) 40 at. % Fe

h) 19 at. % Fe

i) 10 at. % Fe

j) 6 at. % Fe

CVs

Linear regression

$y = 2.67\ x + 0.03$
$R^2 = 0.9996$

k) 2 at. % Fe

CVs

Linear regression

$y = 3.00\ x + 0.04$
$R^2 = 0.9983$
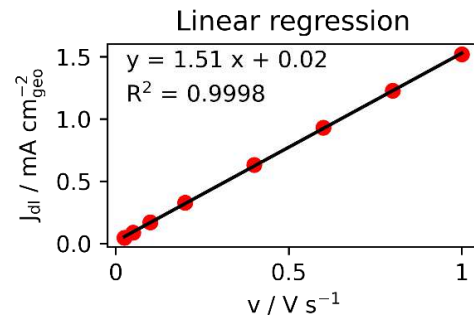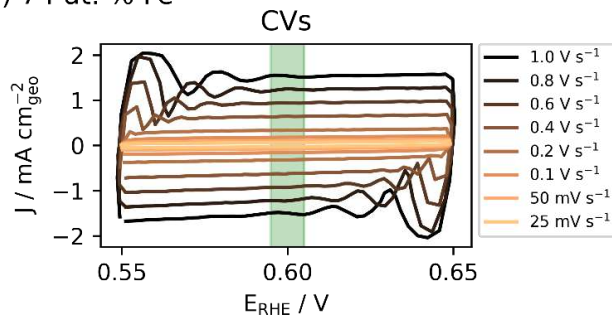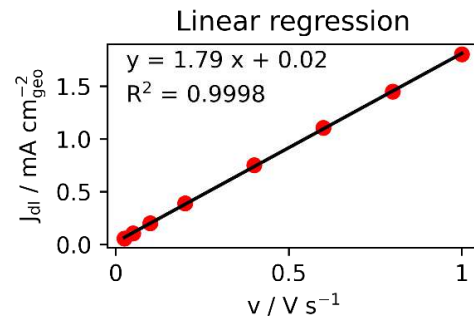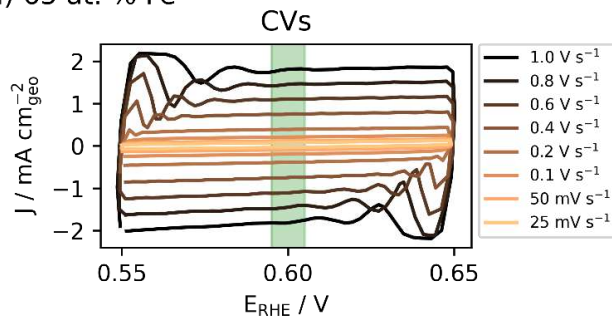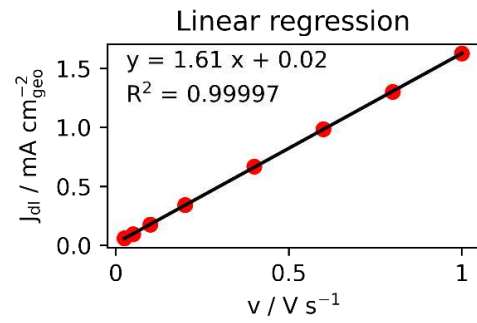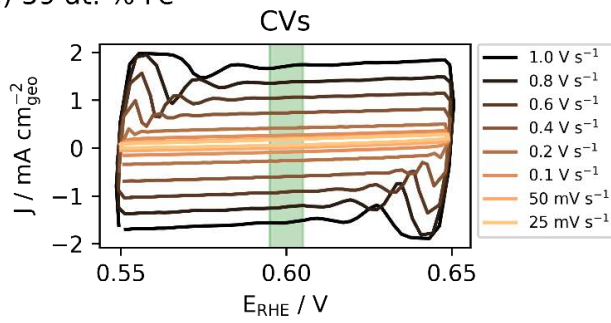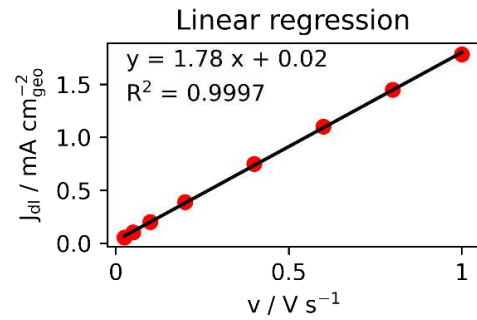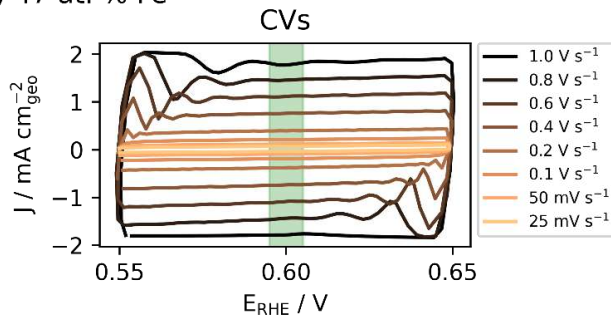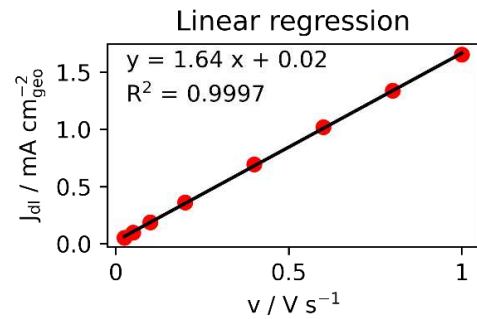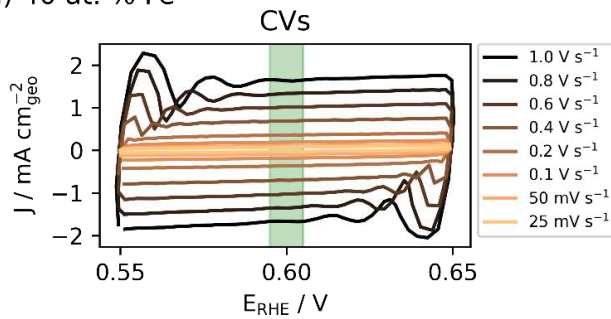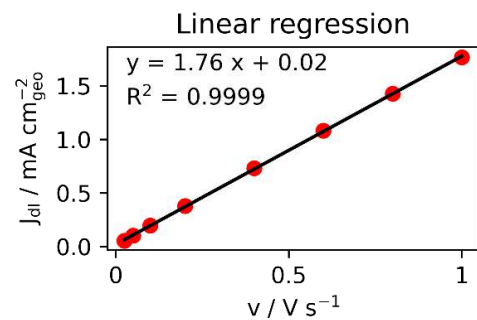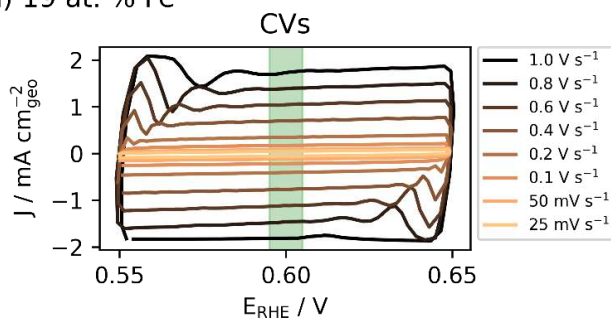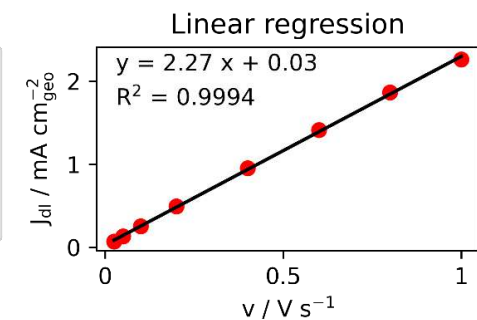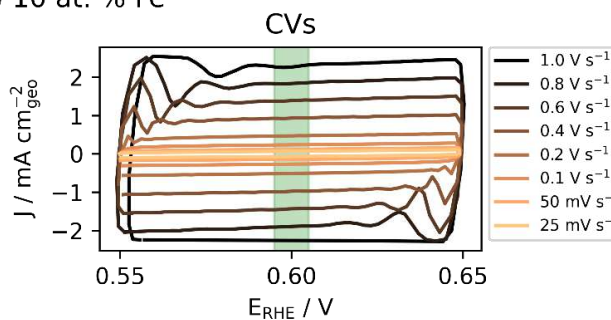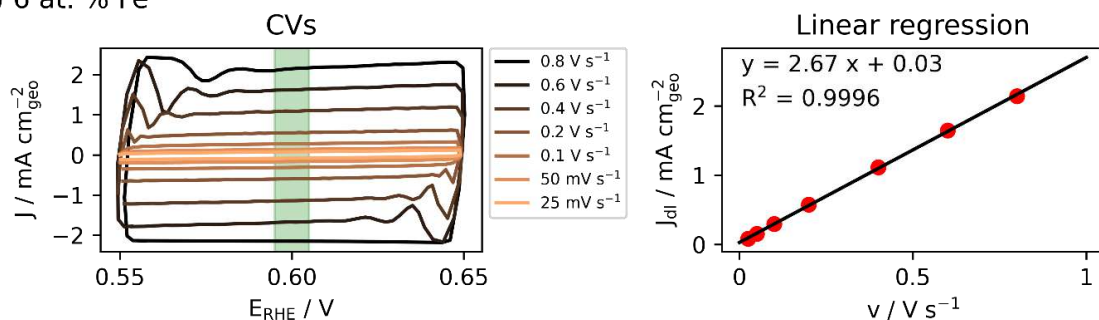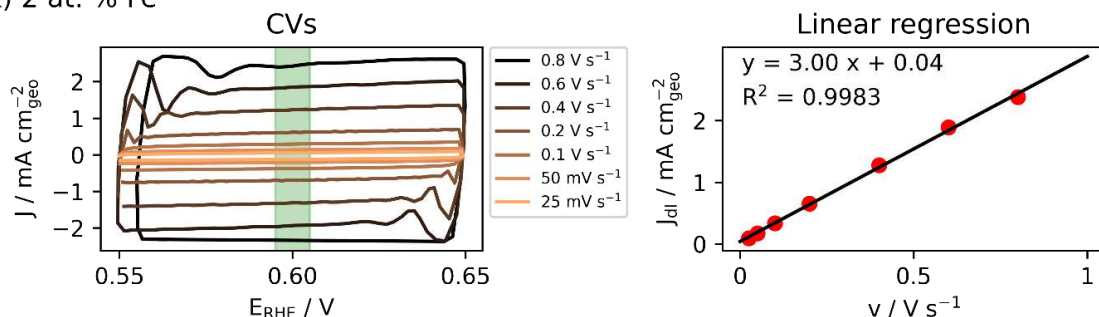
Figure S5. CVs for the double-layer capacity determination in the non-Faradaic region between 0.55 and 0.65 V_{RHE} for all investigated FeNi alloy compositions. To calculate J_{dl}, the current responses between 0.595 and 0.605 V_{RHE} (highlighted in green) were averaged for positive and negative scans. In general, a double-layer capacitance of more than 1 mF cm^{-2} is measured for all foam compositions, with a maximum value of 3.0 mF cm^{-2} for the Ni richest sample.

Roughness factor to express the ECSA

Normalization factor = 39 μF cm^{-2}
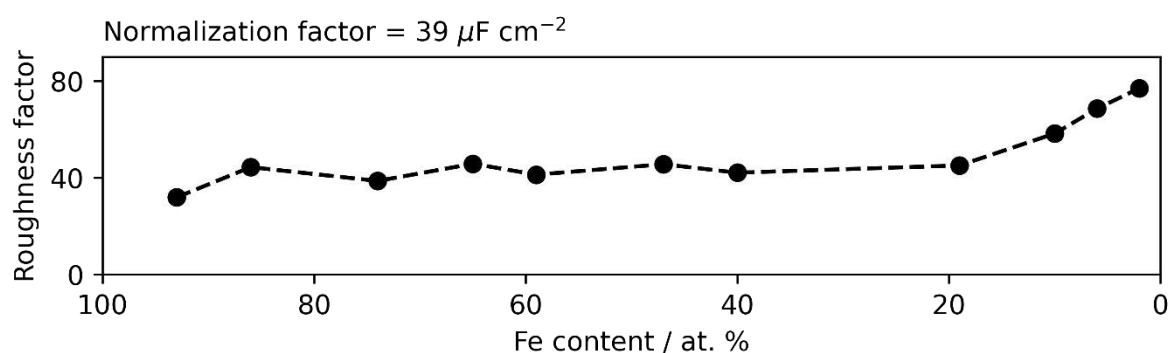
Figure S6. The roughness factor represents the surface morphology relative to a planar surface. It was derived from the ratio of the measured geometrical double-layer capacitance of each foam composition, normalized by the specific Ni metal double-layer capacitance. We determined 39 μF cm^{-2} on pure polished Ni foil in a previous study under similar experimental conditions (4 M KOH electrolyte, equivalent potential window); therefore, we applied this factor for normalization.

Optical geometric area investigation of catalytic disks
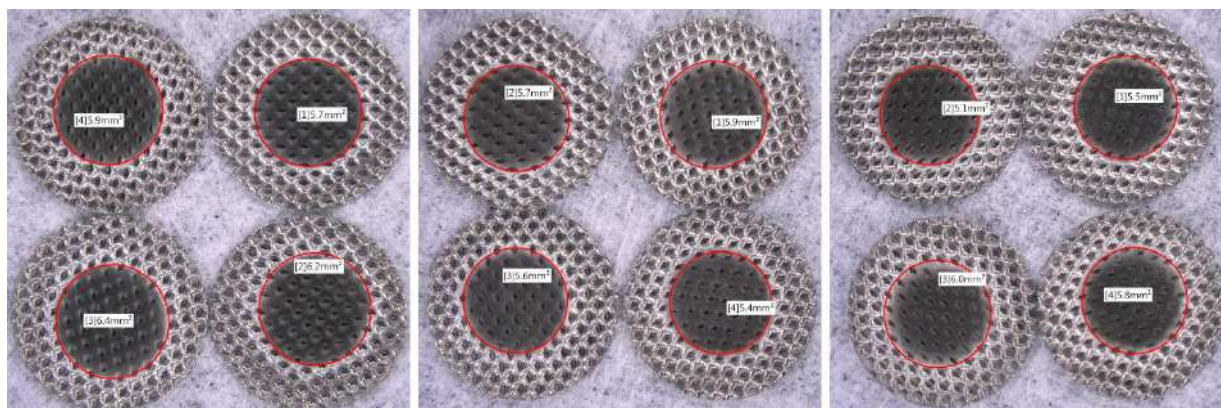
Figure S7. Selected optical micrographs representing the effective geometric areas of the catalytic FeNi foam disks for OER measurements in the dry anode setup. The average geometrical area of the representative 12 samples was 5.8 mm^2, corresponding to 82 % of the assumed geometrical area of 7.1 mm^2. The calibration of the microscope was verified by using a dedicated calibration reference plate.

Effective geometric area evaluation of all disks
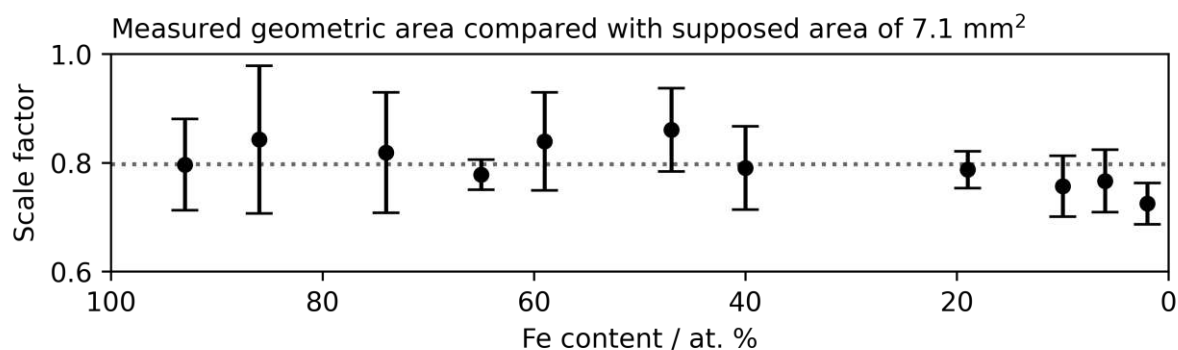
Figure S8. Geometric scale factors for each FeNi composition. The eight disks per FeNi composition were measured twice, each at two magnifications. The error bars show the standard deviations of the 16 measured areas. The dashed line shows the average of all 176 measured areas, corresponded to 5.64 mm^2.

Low geometric current density evaluation

a) 93 at. % Fe

b) 86 at. % Fe

c) 74 at. % Fe

d) 65 at. % Fe

e) 59 at. % Fe

CVs, scan rate v = 5 mV s⁻¹ — legend: d1, d2, d3, d4

Tafel fit — legend: 41 mV dec⁻¹, 38 mV dec⁻¹, 36 mV dec⁻¹, 38 mV dec⁻¹

Potential vs. Log (J)

f) 47 at. % Fe

CVs, scan rate v = 5 mV s⁻¹ — legend: d1, d2, d3, d4

Tafel fit — legend: 38 mV dec⁻¹, 39 mV dec⁻¹, 47 mV dec⁻¹, 39 mV dec⁻¹

Potential vs. Log (J)

g) 40 at. % Fe

CVs, scan rate v = 5 mV s⁻¹ — legend: d1, d2, d3, d4

Tafel fit — legend: 38 mV dec⁻¹, 40 mV dec⁻¹, 38 mV dec⁻¹, 39 mV dec⁻¹

Potential vs. Log (J)

h) 19 at. % Fe

CVs, scan rate v = 5 mV s⁻¹ — legend: d1, d2, d3, d4

Tafel fit — legend: 46 mV dec⁻¹, 40 mV dec⁻¹, 41 mV dec⁻¹, 41 mV dec⁻¹

Potential vs. Log (J)

i) 10 at. % Fe

j) 6 at. % Fe

k) 2 at. % Fe

Figure S9. CV analysis of each composition with four disks. CVs, Tafel fit, and potential vs. log (J) visualizations are shown. Using the CV data, we identified the potentials at which a current density of 10 mA cm^{-2} was reached. The Tafel slope was fitted for each sample using 30 data points below the onset potential of 10 mA cm^{-2}. From the potential vs. log (J) plots, it can be seen that the Tafel fit was not maintained for current densities above 30 mA cm^{-2}.

Overpotential required to reach the onset potential
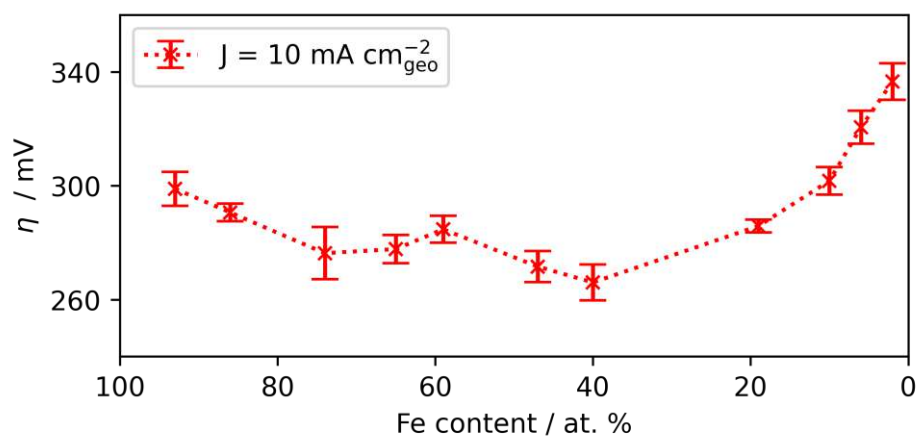
Figure S10. The potential at which 10 mA cm^{-2} is reached, expressed by the overpotential (i.e., the potential beyond the thermodynamic standard potential $E^0 = 1.23$ V). This was derived by evaluating the CV scans (Figure S9).
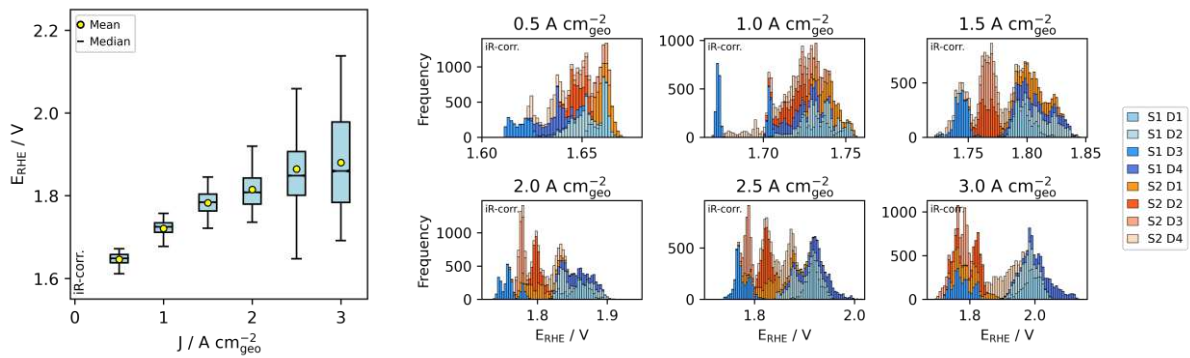
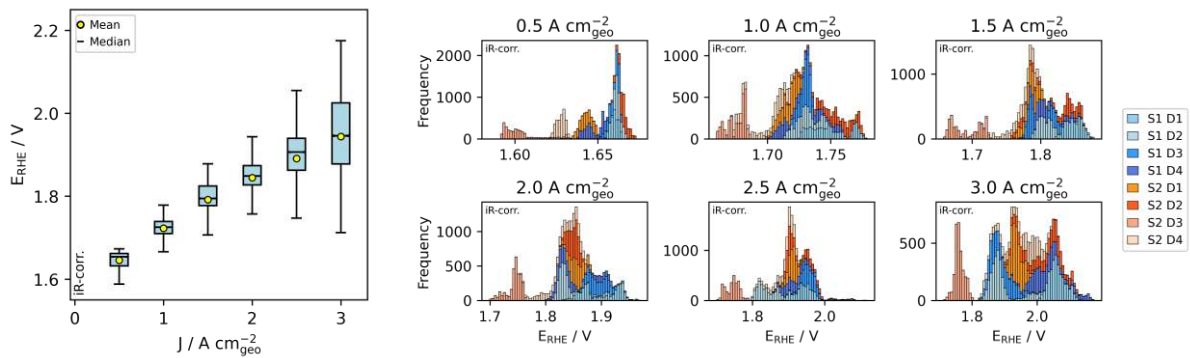# High current density dataset evaluations
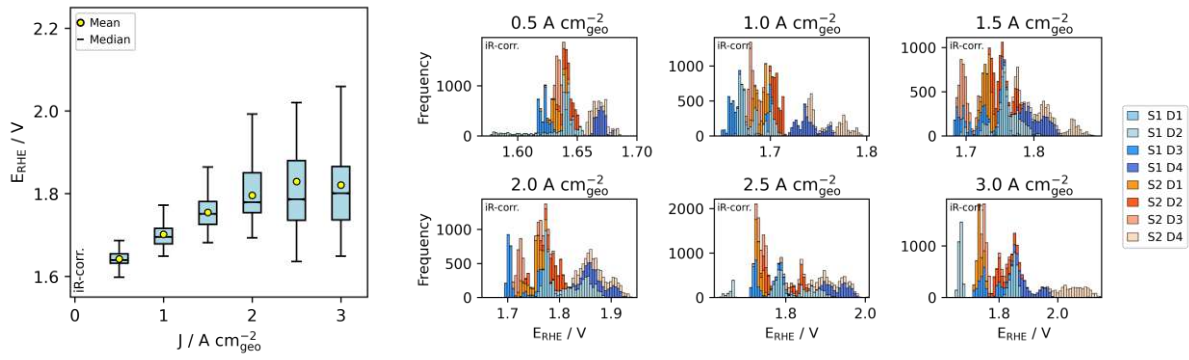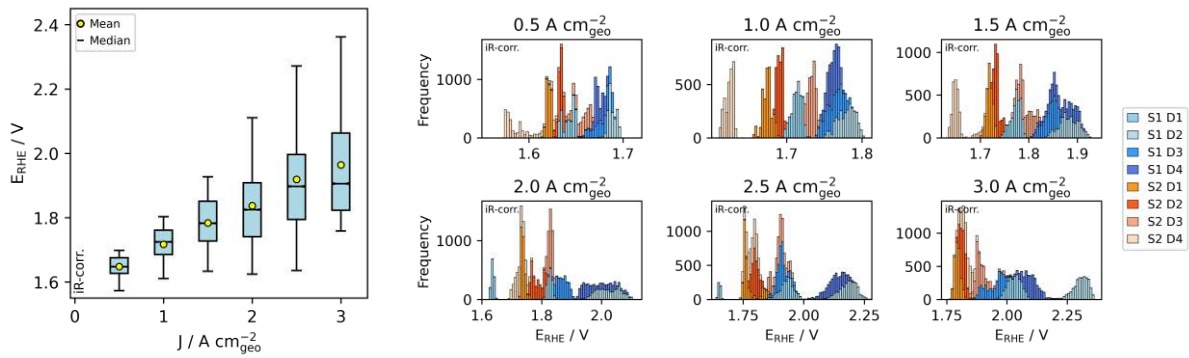
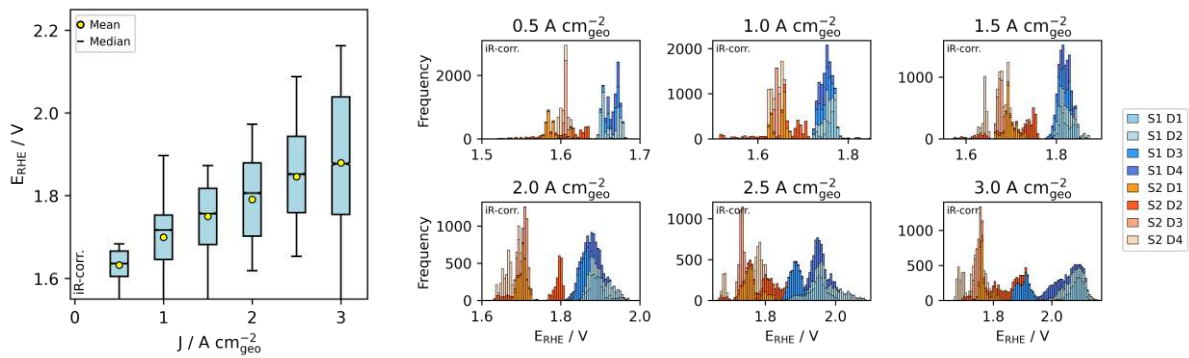## a) 93 at. % Fe
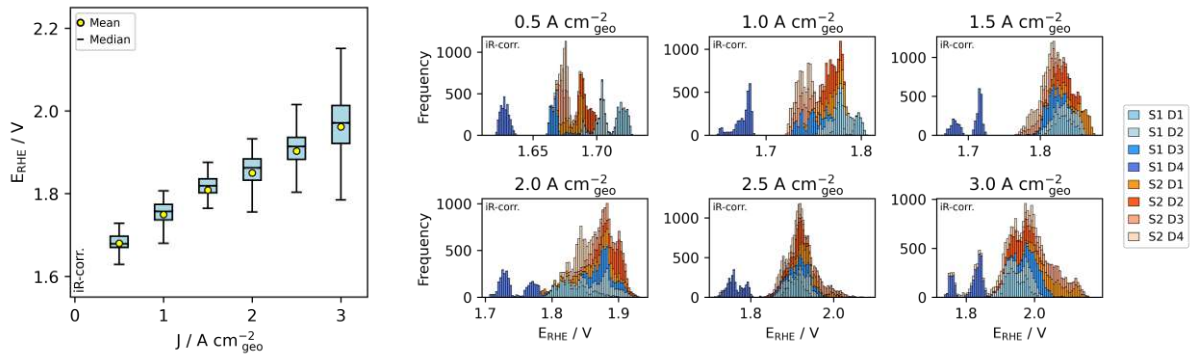
b) 86 at. % Fe
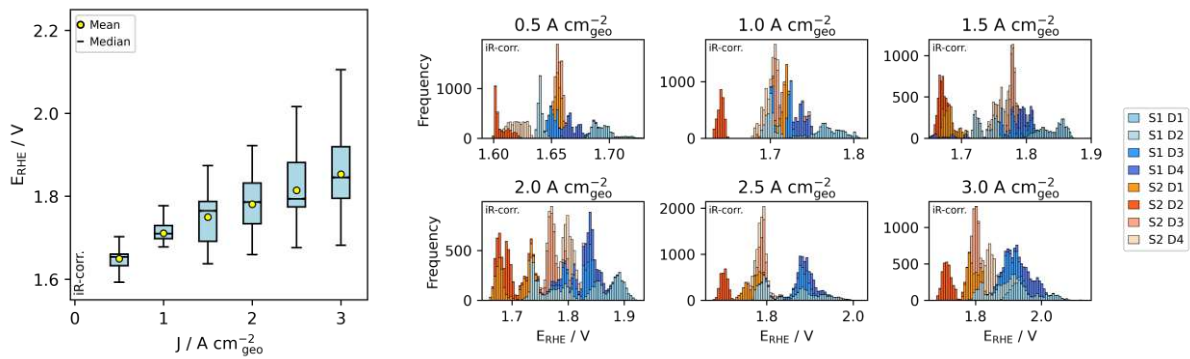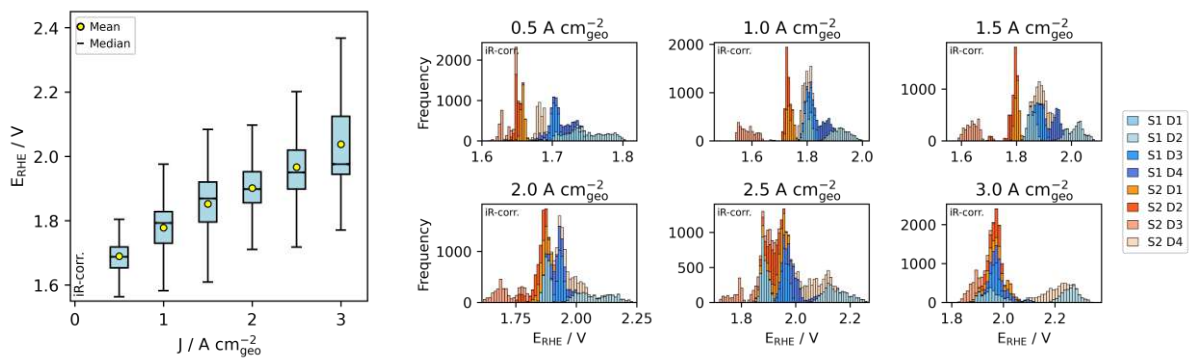

c) 74 at. % Fe

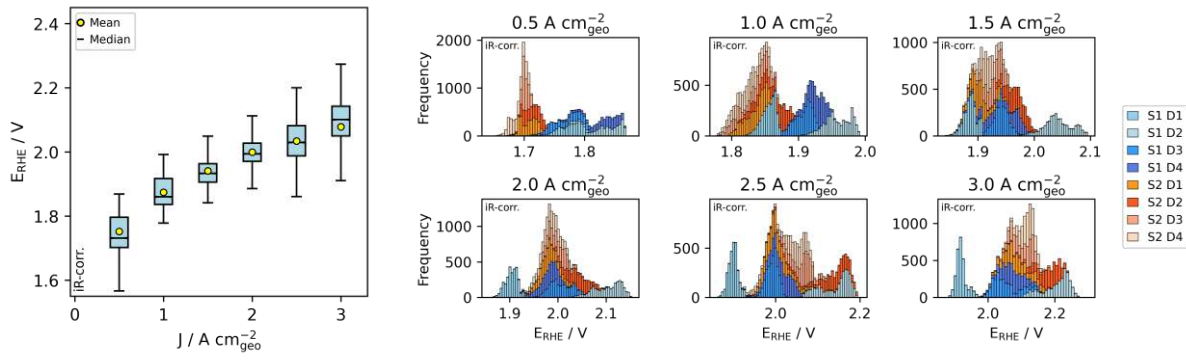## d) 65 at. % Fe

e) 59 at. % Fe

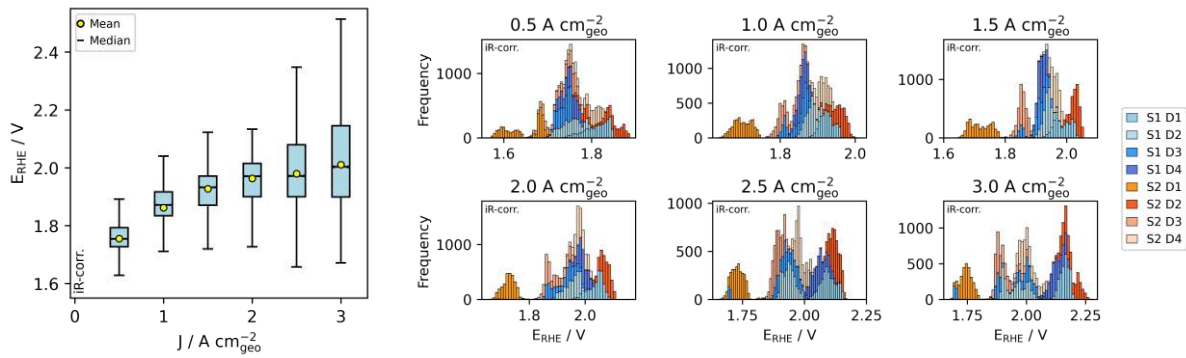## f) 47 at. % Fe

g) 40 at. % Fe

h) 19 at. % Fe

i) 10 at. % Fe

j) 6 at. % Fe

k) 2 at. % Fe
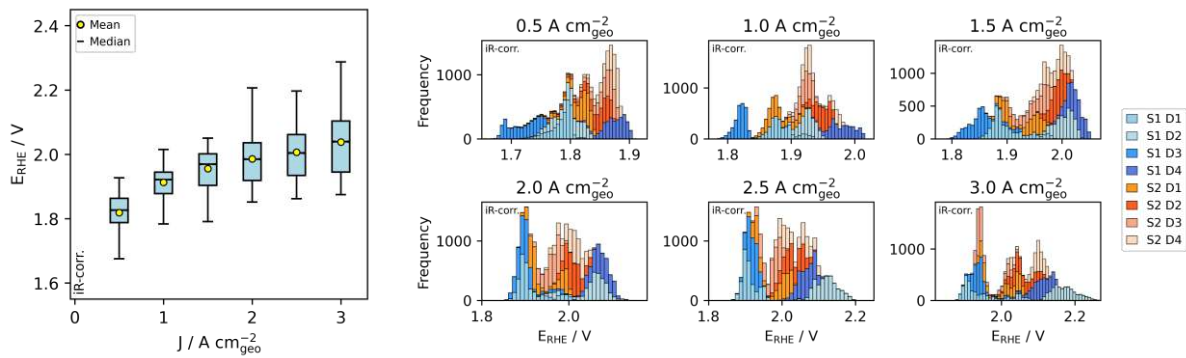
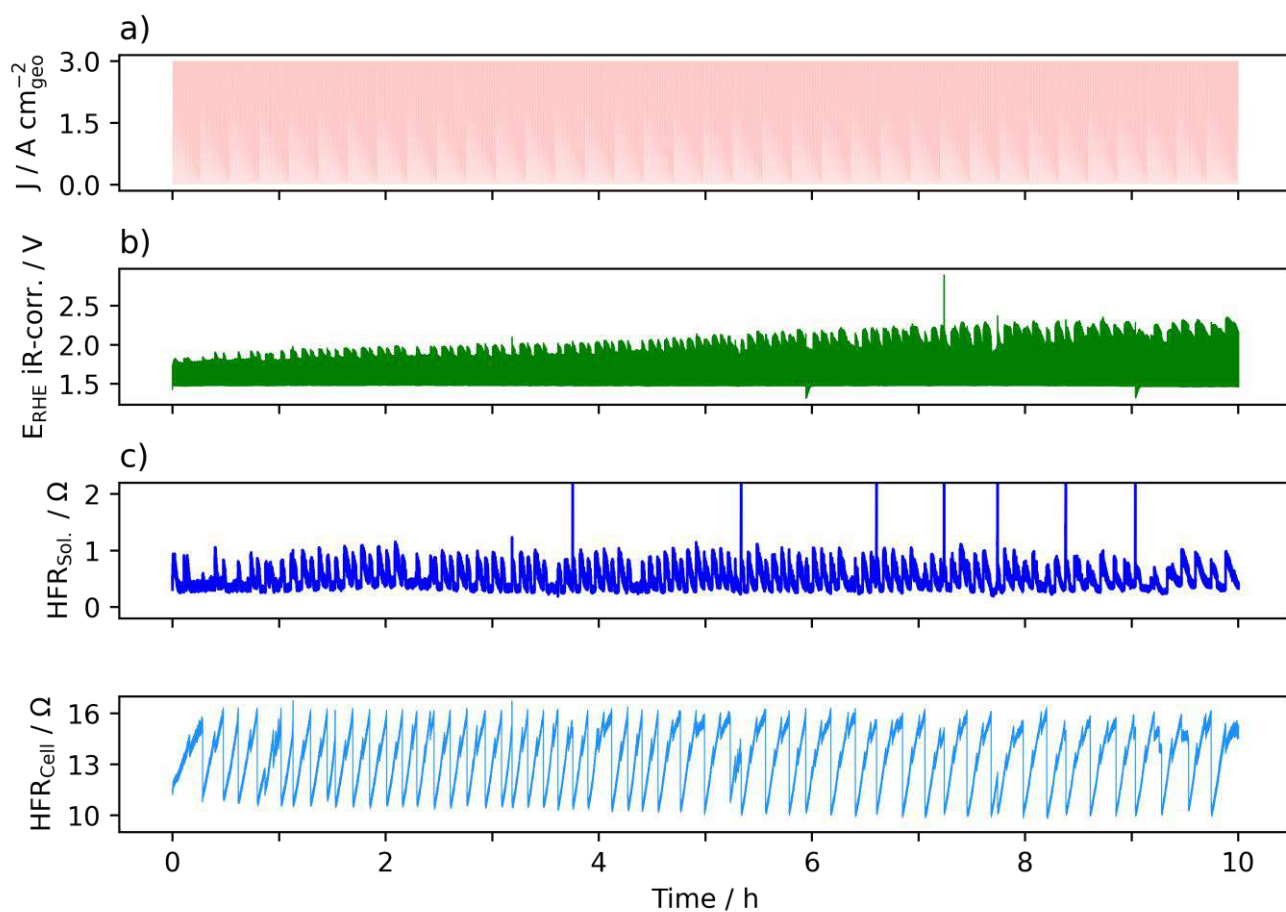**Figure S11.** Boxplots of applied iR-corrected potentials to reach the specific current densities. The corresponding histograms help to understand the potential distribution. Each disk has an own color, with the first synthesis in a blue and the second synthesis in a red color theme.

Stability measurement

Figure S12. The entire dataset of the stability measurement with a higher resolution.
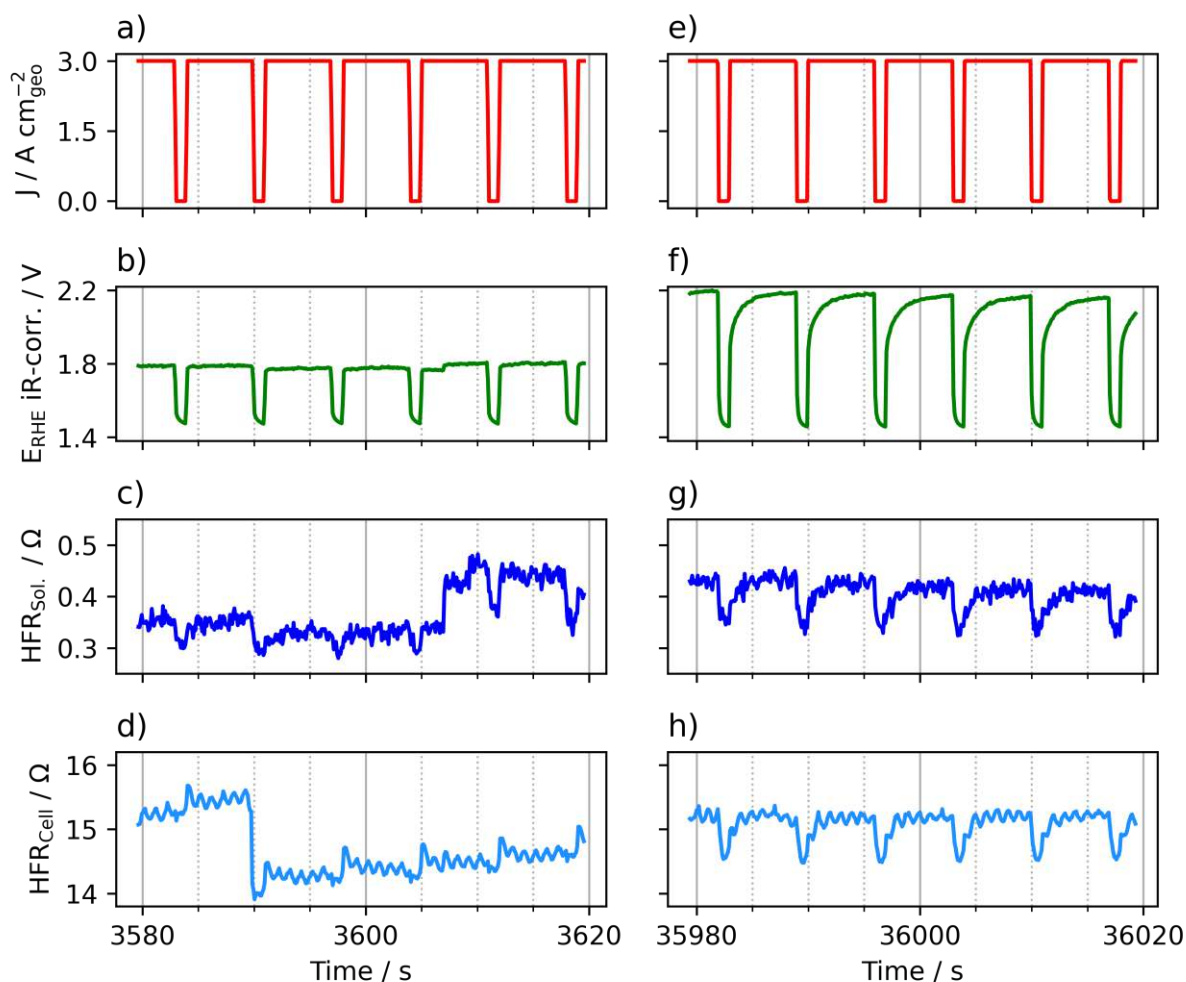
Figure S13. Timeframes of 40 s after 1 h and 10 h are presented to illustrate the pulse characteristics evolution during the stability test.

References:

The XRD reference data were obtained from the "Crystallography Open Database" (www.crystallography.net).

Fe (bcc): COD entry # 4113928
Woodward, P. M.; Suard, E.; Karen, P., *Journal of the American Chemical Society*, 3, *125*, 8889-8899

Ni (fcc): COD entry # 2102272
Angel, R. J.; Bismayer, U.; Marshall, W. G., *Acta Crystallographica Section B*, 2004, *60*, 1-9

Ti (hcp): COD entry # 9008517
Wyckoff, R. W. G., Interscience Publishers, New York, *Crystal Structures*, 1963, *1*, 7-83

Declaration of consent

On the basis of Article 18 of the PromR Phil.-nat. 19

Name/First Name:	Berner, Etienne
Registration Number:	06-907-299
Study program:	PhD in Chemistry and Molecular Sciences
Document:	Dissertation
Title of the thesis:	Investigation of Dry Anodes Utilizing Electroplated Nickel and Nickel-Alloy Foam Catalysts for the Alkaline Oxygen Evolution in Anion Exchange Membrane Electrolyzers
Supervisor:	Prof. Dr. Matthias Arenz

I declare herewith that this thesis is my own work and that I have not used any sources other than those stated. I have indicated the adoption of quotations as well as thoughts taken from other authors as such in the thesis. I am aware that the Senate pursuant to Article 36 paragraph 1 litera r of the University Act of September 5th, 1996 and Article 69 of the University Statute of June 7th, 2011 is authorized to revoke the doctoral degree awarded on the basis of this thesis. For the purposes of evaluation and verification of compliance with the declaration of originality and the regulations governing plagiarism, I hereby grant the University of Bern the right to process my personal data and to perform the acts of use this requires, in particular, to reproduce the written thesis and to store it permanently in a database, and to use said database, or to make said database available, to enable comparison with theses submitted by others.

Bern, Sept. 25, 2024   Etienne Berner

Etienne Berner

Curriculum Vitae

Matriculation ID: 06-907-299
ORCID iD: *0000-0002-4902-2687*
Researcher ID: *AAV-6558-2021*
✉ *etienne.berner@unibe.ch*
Nationality: Swiss

Driven by a passion for research, I find fulfillment in discoveries and optimizations that contribute to a more sustainable energy landscape.

Education

Sept. 2020 - Dec. 2024	**PhD candidate of science in chemistry and molecular sciences**, *University of Bern*.
	Doctoral studies in the field of sustainable transformation of energy sources, with a focus on water electrolysis. Experimental laboratory activities include:

- Development and application of electroplated coatings
- Experimental setup initialization and continuous improvement
- Electrochemical measurements, e.g. pulsed potentio- & galvanostatic assets, ECSA, Tafel analyses [1, 2, 3]
- Scanning Electron Microscopy (SEM) and optical microscopy [4, 5, 6]
- Energy-dispersive X-ray spectroscopy (EDS) and X-ray diffraction (XRD) [9, 10, 11, 12, 13]

Sept. 2007 - Sept. 2012	**Master of science in nanosciences**, *University of Basel*.
	Natural scientific, interdisciplinary degree course (chosen core area physics) with insights to the physics of elementary particles, surface interactions, thin films, inorganic & organic chemistry and cell biology The academic studies allowed sound standing laboratory activities in:

- Nano-fabrications (electron- and UV-lithography), a. o. PVD, CVD [8] and spin-coating of thin films
- Electron microscopy (SEM, TEM) of thin films like graphene, TiO_x layers or cryo-SEM of biological probes
- Atomic force microscopy (AFM) of thin films and biological samples
- X-ray diffractometry with grazing incidence (GI-XRD)
- Raman spectroscopy of graphene
- Neutron spectroscopy (at Paul Scherrer Institute)
- Setup of an optical trap (Laser-trap), combined with fluorescence microscopy

Sept. 2006 - Sept. 2007	**Basic study mechanical engineering**, *ETH Zürich*.
	Basic study of mechanical engineering includes mathematics, material sciences and innovation processes
Aug. 2002 - Dec. 2005	**Matura**, *Gymnasium Münchenstein*.
	Type W (economy and law); Project work: Into the future with renewable energies; Elective course: Robotics

Master thesis

Title	*Towards the inverted cyanine-dye solar cell*
Supervisors	Prof. Dr. Ernst Meyer, Department of Physics, University of Basel Dr. Roland Hany, Laboratory for Functional Polymers, EMPA Dübendorf
Description	Organic solar cells offer a possible alternative to the silicon technology. During the thesis I implemented an organic dye into a stack of inorganic thin films, which converted light into electricity. [7, 8] [14, 15]
Download	Available online: *https://nanoscience.ch/de/studium/masterstudium/masterarbeiten-archiv/*

Professional experience

	University of Bern, Bern.
2020 - 2024	Research Associate & Teaching Assistant.
	Essilor Technology & Service Center Switzerland AG, Trimbach.
2018 - 2020	Manager Final Control & Surfacing.
2017 - 2018	Head Hard Coating.
	Freelance mandates, Olten.
2016 - 2017	Consultant for optical technology and a photovoltaic project.
	Blösch AG, Grenchen.
2016	Production Manager.

Rolic Technologies Ltd., Allschwil.

2015 Research Associate, Patent applications: [16, 17].
2013 - 2014 Application Engineer.

Internships

2010 **EBM Ecotec AG**, Münchenstein.
2006 **Stöcklin AG**, Dornach.

Languages

German Mother tongue
English Business fluent, written and spoken (CEFR: C1)
French Fluent, written and spoken (CEFR: B2)

Computer skills

MS Office	Advanced user knowledge	MATLAB, Origin	Good user knowledge
Python, Jupyter	Advanced user knowledge	LabView, WP Ⓦ	User knowledge
LaTeX	Advanced user knowledge	GIMP, Photoshop	Advanced user knowledge
OS	Windows, Linux, MAC	SQL, C+, Fortran	Basic knowledge

Scientific contributions

Publications

[1] Etienne Berner, Gustav K.H. Wiberg, and Matthias Arenz. Investigation of FeNi alloy foams at high oxygen evolution reaction rates using a dry anode setup in alkaline environment. *ChemRxiv*, 2024.

[2] Baiyu Wang, Nicolas Schlegel, Olivia Aalling-Frederiksen, Etienne Berner, Damin Zhang, Rebecca K. Pittkowski, Kirsten M. Ø. Jensen, and Matthias Arenz. $(Ni_{1-x}Fe_x)OOH$ binary nanoparticles in as-prepared and purified KOH electrolyte solutions for water splitting. *ACS Applied Nano Materials*, 7(11):12345–12355, 2024.

[3] Etienne Berner, Gustav K.H. Wiberg, and Matthias Arenz. Attaining substantially enhanced oxygen evolution reaction rates on Ni foam catalysts in a gas diffusion electrode setup. *Advanced Energy and Sustainability Research*, 5(9):2400050, 2024.

[4] Aline Bornet, Rebecca Pittkowski, Tobias M. Nielsen, Etienne Berner, Annabelle Maletzko, Johanna Schröder, Jonathan Quinson, Julia Melke, Kirsten M. Ø. Jensen, and Matthias Arenz. Influence of temperature on the performance of carbon- and ATO-supported oxygen evolution reaction catalysts in a gas diffusion electrode setup. *ACS Catalysis*, 13(11):7568–7577, 2023.

[5] Sven Nösberger, Jia Du, Jonathan Quinson, Etienne Berner, Alessandro Zana, Gustav K.H. Wiberg, and Matthias Arenz. The gas diffusion electrode setup as a testing platform for evaluating fuel cell catalysts: A comparative RDE-GDE study. *Electrochemical Science Advances*, 3(1):e2100190, 2023.

[6] Johanna Schröder, Vladislav A. Mints, Aline Bornet, Etienne Berner, Mohammad Fathi Tovini, Jonathan Quinson, Gustav K. H. Wiberg, Francesco Bizzotto, Hany A. El-Sayed, and Matthias Arenz. The gas diffusion electrode setup as straightforward testing device for proton exchange membrane water electrolyzer catalysts. *JACS Au*, 1(3):247–251, 2021.

[7] Gaëtan Wicht, Etienne Berner, Timo Jäger, Hui Zhang, Roland Hany, and Frank Nüesch. *Performance and Stability of Organic Trimethine Cyanine Dye - C_{60} Heterojunction Solar Cells*, pages 221–229. Springer International Publishing. Materials Challenges and Testing for Manufacturing, Mobility, Biomedical Applications and Climate; ISBN: 978-3-319-11339-5, 2014.

[8] Etienne Berner, Timo Jäger, Thomas Lanz, Frank Nüesch, Jean-Nicolas Tisserant, Gaëtan Wicht, Hui Zhang, and Roland Hany. Influence of crystalline titanium oxide layer smoothness on the performance of inverted organic bilayer solar cells. *Applied Physics Letters*, 102(18):183903, 2013.

Oral & poster presentations

[9] Etienne Berner, Gustav K.H. Wiberg, and Matthias Arenz. Achieving enhanced oxygen evolution reaction rates on Ni-based foam catalysts in a gas diffusion electrode setup. Oral presentation at 37th Topical Meeting of the International Society of Electrochemistry, June 2024. Convention Centre, Stresa, Italy.

[10] Etienne Berner, Gustav K.H. Wiberg, and Matthias Arenz. Attaining substantially enhanced oxygen evolution reaction rates on Ni foam catalysts in a gas diffusion electrode setup. Poster presentation

at Electrocatalysis Symposium 2024 (International Symposia Series on Electrocatalysis), Mai 2024. Campus of Friedrich-Alexander-Universität, Nürnberg, Germany.

[11] Etienne Berner, Gustav K.H. Wiberg, and Matthias Arenz. Attaining substantially enhanced oxygen evolution reaction rates on Ni foam catalysts in a gas diffusion electrode setup. <u>Poster</u> presentation at 40th Swiss Electrochemistry Symposium by PSI 2024, April 2024. Kultur- & Kongresshaus, Aarau, Switzerland.

[12] Etienne Berner, Gustav K.H. Wiberg, and Matthias Arenz. Measuring high oxygen evolution reaction current densities in alkaline environment: The gas diffusion electrode setup. <u>Poster</u> presentation at International Summer School on Electrocatalysis and Organic Electrosynthesis 2023, Aug. 2023. Hotel Metropole, Interlaken, Switzerland.

[13] Etienne Berner, Gustav K.H. Wiberg, and Matthias Arenz. Measuring high oxygen evolution reaction current densities in alkaline environment: The gas diffusion electrode setup. <u>Poster</u> presentation at Swiss NanoConvention 2023, June 2023. Patinoires du Littoral, Neuchâtel, Switzerland.

[14] Etienne Berner, Gaëtan Wicht, and Roland Hany. Towards the inverted cyanine-dye solar cell. <u>Oral</u> presentation at INASCON (International Nanoscience Student Conference), Aug. 2013. London Centre for Nanotechnology, London, England.

[15] Etienne Berner, Gaëtan Wicht, and Roland Hany. Towards the inverted cyanine-dye solar cell. <u>Oral</u> presentation at "Next Nano Stars" convention by the Swiss Nanoscience Institute, March 2013. Messe Congress Center, Basel, Switzerland.

Patents

[16] Rolic AG. Multiple hidden image security device. *WO2016188936A1*, 2016.

[17] Rolic AG. Multiple image scattering device. *WO2016166044A1*, 2016.

Bern, Oct. 18th, 2024